Spin Polarization Produced in Projectile Fragmentation Reactions

By

Daniel E. Groh

A DISSERTATION

Submitted to
Michigan State University
in partial fulfillment of the requirements
for the degree of

DOCTOR OF PHILOSOPHY

Department of Chemistry

2002

ABSTRACT

Spin Polarization Produced in Projectile Fragmentation Reactions

By

Daniel E. Groh

Projectile fragmentation is a demonstrated technique for producing fast beams of rare isotopes independent of chemical properties. With selection of appropriate reaction parameters, projectile fragmentation can produce isotopes with some degree of spin polarization. A kinematical model based on the conservation of linear and angular momentum qualitatively describes the polarization data.

A Monte Carlo code has been developed, based on this kinematical model, to calculate the induced fragment spin polarization produced in projectile fragmentation reactions. Quantitative predictions were realized by including the process of nucleon evaporation, realistic angular distributions, de-orientation caused by γ-ray emission and by correcting for the out of plane acceptance. Polarization calculated with this code quantitatively reproduces known polarization data.

The polarization of ^{37}K produced from 150 MeV/A ^{36}Ar on a ^{9}Be target at a beam angle of $+2^{\circ}$ was measured. This was the first observation of polarization produced in a nucleon pickup reaction at fragmentation energies. The presence of polarization can be understood by extending the kinematical model used to understand polarization produced in fragmentation reactions. The qualitative agreement between the predicted and the experimental polarization validates the use of the kinematical conservation model to understand both polarization phenomena.

for Michelle

ACKNOWLEDGMENTS

I would like to thank my advisor, Paul Mantica, for giving me the opportunity to study at the NSCL, for providing endless encouragement and assistance, for answering all my questions (especially the second or third times I asked them), and for putting up with my attitude (specifically in years Two and Three). I didn't always like graduate school, but Paul did his job and kept me here long enough to graduate!

I would like to specifically thank Andreas Stolz and Andrew Stuchbery. Andreas was always open and willing to help me in whatever capacity he could. He was always enthusiastic and he seemed to know the answer to just about every question. Andrew served almost as a surrogate advisor near the end with heavy involvement in my experiment and with the polarization calculations. Andrew seemed to be able to calculate anything! Andreas' knowledge and Andrew's computational ability really saved me - I could not have done it without their invaluable help.

I thank my advisorial committee including Dave Morrissey, the second reader, Thomas Glasmacher and Gregors Hansen for their thoughts and ideas on various issues.

Furthermore, I extend my thanks to the entire cyclotron laboratory. Everyone's hard work and dedication influenced my time here. I would particularly like to mention my fellow group members Andrew, Brian, Sean, Theo and Colin for their willingness to help, answer questions and listen to countless practice seminars! Thanks, guys.

I also want to thank my student colleagues. The shared lunches, laughter and complaining will be missed. I especially want to thank Joann Prisciandaro, my academic big sister. She was the first in our group and she paved the way for me, making things immensely easier. I owe you one, Joann!

And finally I want to thank my wife Michelle. She encourages, supports and loves me through everything. She is the light of my life.

Contents

List of Figures

List of Tables

Chapter 1

Introduction

Many nuclei contain an intrinsic angular momentum in their ground state which is colloquially called spin. This nuclear spin is the result of coupling the intrinsic spin of the nucleons to the orbital angular momentum of the nucleons in the nucleus. Under ordinary circumstances, nuclear spins are randomly distributed with respect to any external reference; thus, a sample of nuclei as a whole has zero net spin orientation. However, if the nuclear spins in a sample are preferentially oriented relative to some external reference, these nuclei are said to be spin polarized.

Nuclei with spin polarization can be utilized in the study of nuclear structure, nuclear reactions, fundamental interactions, and materials science. For all of these applications, a reliable and effective method to produce spin polarization is required. Techniques to produce spin polarization exist depending on the details of the particular experiment or application for spin polarization. In nuclear physics, the production of spin polarized rare isotopes involves not only producing sizeable spin polarization, but also producing a sufficient quantity of nuclei. This work addresses the effort to maximize both spin polarization and yield for the specific case of fragmentation reactions. The following sections provide more formal definitions for spin polarization and fragmentation reactions, an overview of polarization in nuclear physics, as well

as the motivation for this work.

1.1 Spin Polarization

Spin polarization is the result of unequal magnetic substate populations. Specifically, spin polarization occurs when the population for a given substate, m, is not equal to the population for the substate $-m$. Spin alignment is the result of unequal, but symmetric, substate populations; i.e. for spin alignment, the population for substate m equals the population for substate $-m$. Spin polarization and spin alignment are generally discussed in terms of the statistical tensor, ρ, which characterizes the orientation of a particular state [1]. The spin polarization for a given spin value I is defined as the ratio of the statistical tensor to its value for maximum spin polarization. Specifically,

$$\rho_1(\mathrm{I}) = -\sum_{\mathrm{m}} \frac{\mathrm{mP(m)}}{\sqrt{\mathrm{I(I+1)}}} \tag{1.1}$$

and

$$\rho_1^{\max}(I) = \frac{-I}{\sqrt{I(I+1)}} \tag{1.2}$$

so the spin polarization is

$$\rho_1(I)/\rho_1^{\max}(I) = \sum_m mP(m)/I = \langle I_z/I \rangle \tag{1.3}$$

where m is the magnetic substate quantum number, I is the spin and P(m) is the normalized population for substate m. Thus, spin polarization is a measure of the orientation of the total angular momentum relative to a fixed axis. It is generally quantized by the z-component of the nuclear spin divided by the total spin for the system where the beam axis is the y-axis. The terms spin polarization and polarization will be used interchangeably in this text. Spin alignment will be discussed briefly in Chapter 5.

Polarization phenomena were first used as a tool to understand reaction mechanisms because the production of spin polarization is intimately linked to the details of the reaction process. The variation of the polarization with reaction Q-value, product mass, product emission angle, incident energy etc. all give insight into the details of the reaction mechanism. Spin polarization is often determined by measuring the asymmetric angular distribution of decay particles such as α's, β's, γ's or nucleons. Measurements of this type are challenging and are often considered exotic experiments.

1.2 Polarization in Nuclear Reactions

Yamamoto and Kubo [2] produced a brief review of the theoretical and experimental work done concerning polarization produced in nuclear reactions. The following is a summary of that work.

In 1977, the polarization of ^{12}B produced through the 6 MeV/A incident energy heavy-ion reaction ^{100}Mo(^{14}N,^{12}B)^{102}Ru was measured [3]. This experiment drew attention to polarization phenomena in nuclear reactions and gave rise to several theoretical models interpreting the results. Ishihara *et al.* [4] reported that the frictional model alone was not enough to explain the polarization behavior. A semi-classical model proposed by Brink [5] qualitatively explained the sign and magnitude of the polarization with a consideration of continuum final states [2]. In a more quantitative fashion, Udagawa and Tamura [6] performed an exact finite-range (EFR) distorted wave Born approximation (DWBA) calculation that described the data rather well.

Polarization of excited nuclei produced in deep inelastic collisions can be understood on the basis of the frictional model [7]. The frictional model is based on the frictional force between two interacting bodies which sets them to rotating, i.e. the friction between the two nuclei induces spin polarization in both nuclei. The polariza-

tion of excited states in ^{20}Ne was measured by Pougheon *et al.* [8]. An EFR-DWBA calculation reproduces the observed angular distribution, but the spin polarization magnitude is overpredicted. Although the frictional model is not inconsistent with the observed spin polarization data, the authors claim it is too simple to make accurate predictions. Bond reached the same conclusion in Ref. [9].

Polarization measurements in the direct reaction energy regime for (^{14}N,^{12}B) at 8 and 15 MeV/A as measured by Tanaka *et al.* [10] qualitatively agree with the frictional model, but again the magnitude of spin polarization is overpredicted. The behavior of the polarization in that work demonstrates a competition between the frictional process and the direct transfer process at low energy loss for the fragments. Direct reactions are able to produce products with copious spin polarization, but rare isotopes cannot be produced with this reaction mechanism.

Polarization resulting from the reaction ^{197}Au(^{14}N,^{12}B) at 49 MeV/A incident energy was observed by Asahi *et al.* [11]. The semi-classical model developed by these authors provides a qualitative interpretation of the results, but again fails to reproduce the observed magnitude. This model is herein referred to as the Kinematical Model of Asahi, or the KMA. A semi quantum-mechanical model proposed by Ohnishi *et al.* [12] also gives only qualitative agreement with the results.

1.3 Fragmentation Reactions

The heavy-ion reaction Asahi *et al.* studied is in the energy regime of projectile fragmentation. Heavy-ion projectile fragmentation is a powerful technique for the production of rare isotopes. Fragmentation reactions are characterized by fast projectiles (100's of MeV/A) bombarding thin (100's of mg/cm^2, usually metal) stable targets. Fragments ranging in mass from 1 nucleon below the projectile mass down to helium are produced in varying quantities depending on the reaction parameters. Fragments

of interest are selected using some type of in-flight fragment separator and sent to the experimental end station. The fragments are produced with momentum close (usually within $\pm 5\%$) to the incident projectile momentum. Though fragmentation reactions are used at experimental accelerator facilities around the world to produce rare isotopes, the measurement of Asahi *et al.* was significant because it was the first observation of polarization produced as a direct result of the reaction mechanism itself.

1.4 Motivation

The interest in studying polarization produced in nuclear reactions in the late 1970's was with the goal of understanding reaction mechanisms. The present author's interest in polarization stems from a desire to optimize both polarization and yield in fragmentation reactions in order to exploit polarization for nuclear structure and reaction studies. The KMA proves to be a functional description of the trends observed for polarization produced in heavy-ion fragmentation reactions. Even though it is a macroscopic model depending only on classical conservation laws, it does a remarkable job describing the data; but it lacks predictive power.

The goals of this work were two-fold. The first was to develop the statistical KMA into a Monte Carlo fragmentation code capable of *quantitatively predicting* the spin polarization for fragments produced in intermediate-energy heavy-ion fragmentation reactions. To achieve quantitative predictability, the statistical KMA will be applied to its fullest extent. A workable Monte Carlo code based on the KMA would lend itself not only to understanding polarization phenomena, but also to experimental measurements requiring polarized beams.

The second goal of this work was to make a spin polarization measurement to test the predictive power of the classical model. The idea was that the successful implemen-

tation of the KMA into a Monte Carlo code would encourage systematic experimental measurements investigating the interesting polarization behavior demonstrated in the model. Ironically, in building a code to model fragmentation reactions, it became apparent that pickup reactions should show a large degree of spin polarization. Thus, the experimental portion of this work involved the measurement of the polarization of ^{37}K produced from a primary beam of ^{36}Ar. Furthermore, the KMA was extended to consider both fragmentation reactions and pickup reactions since the classical description is applicable for both systems. This model describes the polarization behavior of the ^{37}K pickup products and helps highlight the physics behind the observed polarization.

The development of the Monte Carlo code is dealt with in Chapter 2. This includes a discussion of the kinematical model and an earlier attempt to apply the kinematical model in a statistical treatment. Improvements and enhancements of this treatment including angular distributions, out-of-plane acceptance, the process of nucleon evaporation and γ-ray de-orientation will also be discussed. The results of the new statistical model are compared to previous data and shown to reproduce the trends and magnitude of the polarization. The statistical model is also applied to pickup reactions at fragmentation energies and suggests sizeable polarization can be produced in pickup products. The experimental details for the polarization measurement of a proton pickup product are contained in Chapter 3. The experimental results and interpretation of the results where the observed polarization is qualitatively explained using the kinematical model are in Chapter 4. Chapter 5 draws conclusions based on the results of the experiment and the calculations, and provides a future outlook. This chapter includes a critical analysis of the shortcomings and limitations of the statistical treatment as it is applied to polarization produced in fragmentation reactions.

Chapter 2

Polarization in Fragmentation Reactions

2.1 Kinematical Model of Asahi (KMA)

Polarized secondary fragments were first produced in intermediate-energy heavy-ion fragmentation reactions at finite fragment angles by Asahi *et al.* [11]. This represented the first measurement of polarization produced as a direct result of the fragmentation reaction mechanism. Asahi *et al.* also developed a model based on the classical transfer of angular momentum to the fragment in order to understand the mechanism governing the production of polarization in these fragmentation reactions.

The KMA considers a fast peripheral collision between a projectile nucleus and a target as occurring along a straight line; the nucleons in the overlap region of the target and projectile are removed from the projectile and the remaining projectile nucleons compose the outgoing fragment. An important feature of this model is that the fragment part of the projectile remains a spectator while the participating nucleons in both partners are abraded and removed. Considering conservation of both linear and angular momentum, there exists a correlation between the outgoing momentum

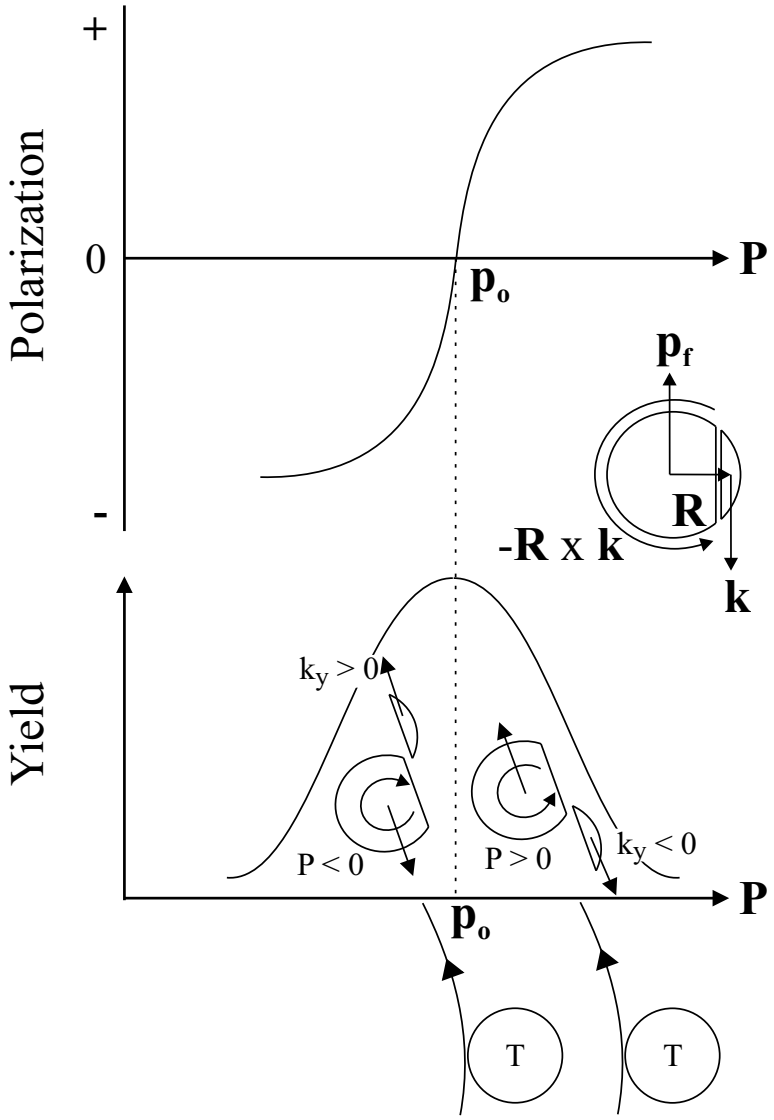

Figure 2.1: Schematic representation of near-side collision and resulting polarization (adapted from [11]).

p and the angular momentum **L** of the fragment, as shown in Figure 2.1. If $\mathbf{p}_0$ is the incident momentum of the projectile, **p** is the outgoing momentum of the fragment, and **R** is the vector pointing from the fragment to the removed portion, then $\mathbf{L} = -\mathbf{R} \times \mathbf{k}$ where **k** is the momentum of the removed portion in the projectile rest frame (as given by $\mathbf{p} = \mathbf{p}_0 - \mathbf{k}$). The projectile is assumed to have zero initial polarization, and the intrinsic spins of the removed nucleons are ignored for simplicity. The sign of the polarization is defined as positive when the spin is parallel to the vector $\mathbf{p}_0 \times$

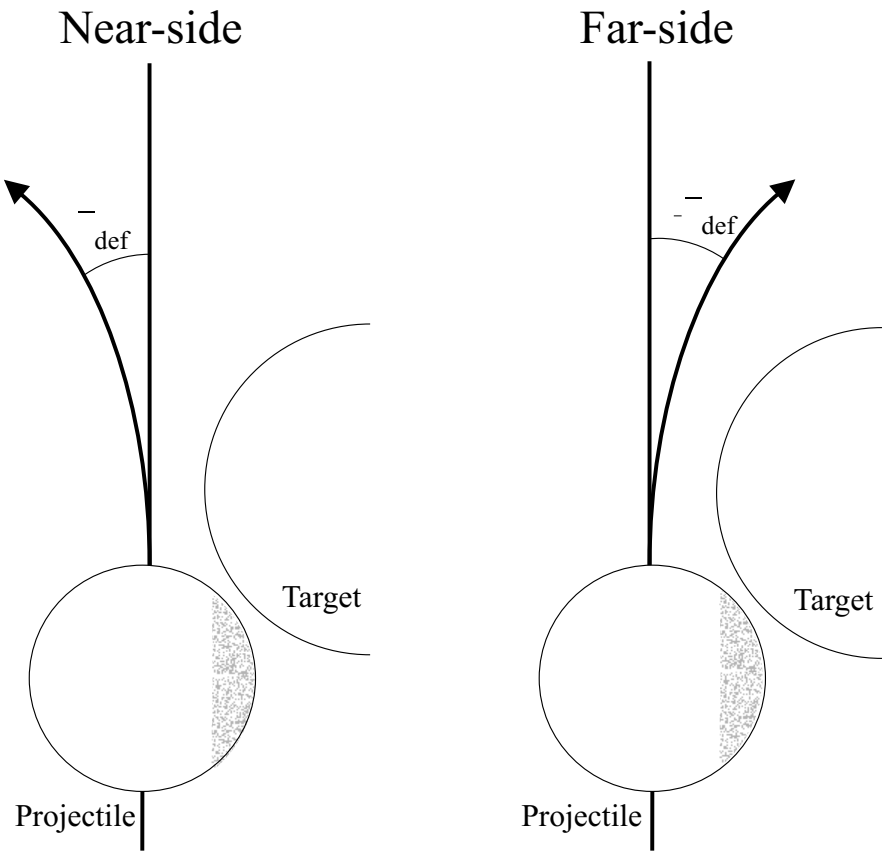

Figure 2.2: Schematic diagram of near- and far-side collisions.

p. Thus, negative(positive) polarization is expected when **k** is parallel(anti-parallel) to the beam direction. The magnitude of polarization is expected to be symmetric about $p = p_0$. Zero polarization is predicted at $p = p_0$, the peak of the production yield curve.

The above discussion assumes near-side trajectories. A near-side trajectory occurs when the fragment scatters to a positive mean deflection angle $\bar{\theta}_{\rm def}$ not crossing the plane of the target (see Figure 2.2). This is the result of the repulsive Coulomb potential dominating the interaction of the target and projectile. If the fragment scatters to a negative mean deflection angle (caused by the dominance of the attractive nucleon-nucleon potential), a far-side trajectory is followed. In this case the reversed relationship between the sign of the polarization and p is expected.

As mentioned in the introduction, the KMA was able to explain the polarization

of the ^{12}B fragments produced at a finite fragment angle from a reaction of ^{14}N on ^{197}Au at 40.6 MeV/A as measured by Asahi *et al.* [11].

To study more closely the effects of different targets and incident energies on the polarization of fragments, Okuno *et al.* [13] conducted a series of experiments to measure the polarization of fragments from fragmentation reactions. Selected results from their measurements are shown in Figure 2.3. Reaction (a) represents the near-side collision Asahi *et al.* studied, and reaction (e) represents a far-side collision. The qualitative behavior of 'pure' near- or far-side reactions follows the KMA. The maximum polarization is produced in the wings of the momentum distribution, while at the peak of the momentum distribution little or no polarization is produced. Closer examination of Figure 2.3 reveals a natural progression from a near-side collision in (a) to a far-side collision in (e), with trajectory 'mixing' in between. The trajectory mixing reactions are characterized by a small or zero mean deflection angle. The peak of the polarization for these reactions is observed at the peak of the momentum yield curve, and little or no polarization is observed in the wings of the momentum distribution.

Even though the polarization spectra for reactions (a) and (e) in Figure 2.3 qualitatively agree with the KMA, the reactions (b) through (d) deviate in that they have sizeable polarization at the peak of the momentum yield curve. This is a favorable condition for future experiments that may exploit polarization for nuclear structure or reaction studies. The appearance of polarization at p_0 can be explained within the KMA. The polarization is the z-component of angular momentum normalized to the total angular momentum

$$P = l_z/|\mathbf{L}| \tag{2.1}$$

where the z-component of angular momentum for the fragment is given by

$$l_z = -Xk_y + Yk_x \tag{2.2}$$

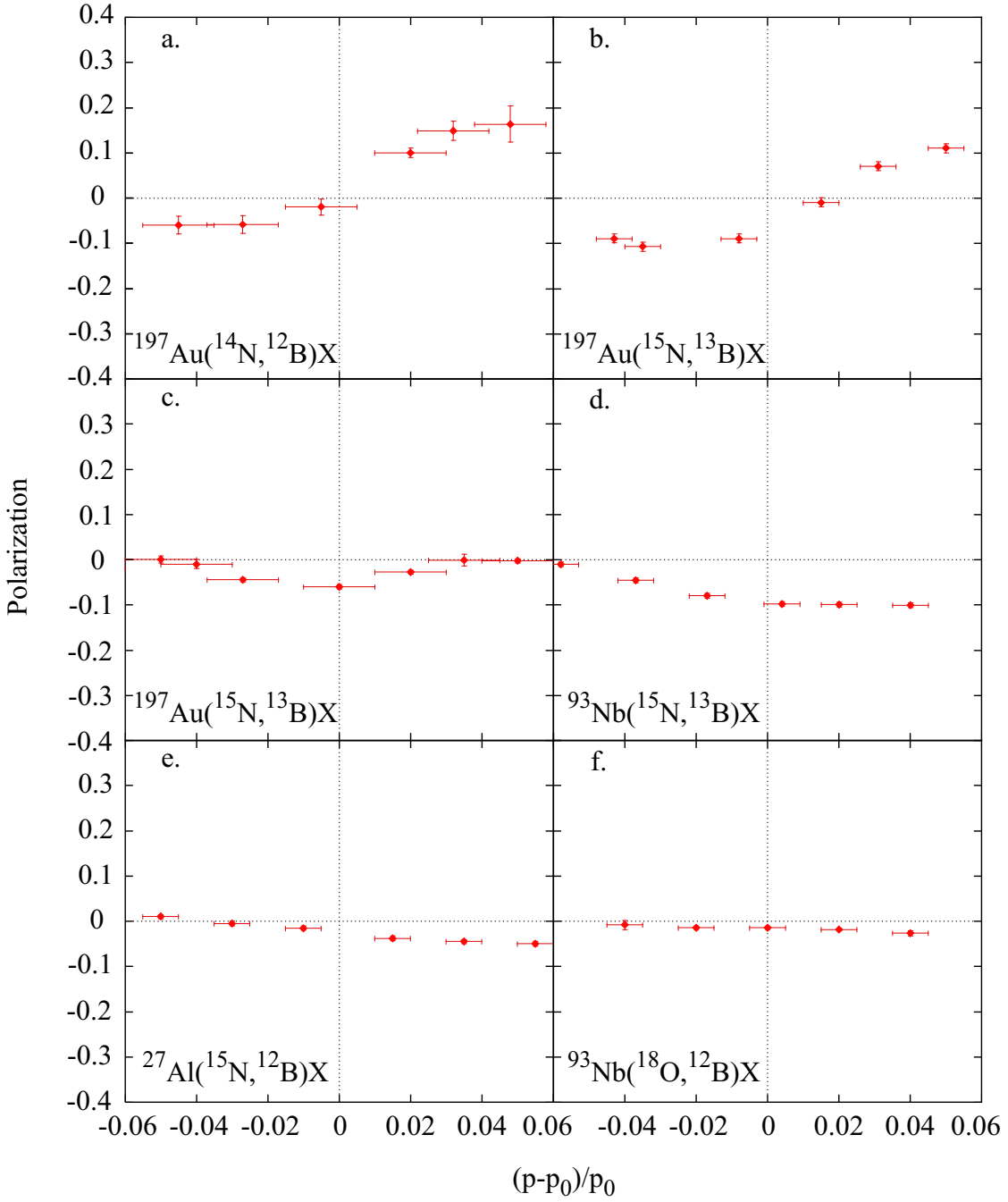

Figure 2.3: Measured spin polarization spectra as functions of relative fragment momentum for (a) ^{14}N (39.4 MeV/A) + ^{197}Au $\rightarrow$ ^{12}B (θ_L = 5.0°) + X, (b) ^{15}N (68.0 MeV/A) + ^{197}Au $\rightarrow$ ^{13}B (θ_L = 4.0°) + X, (c) ^{15}N (109.6 MeV/A) + ^{197}Au $\rightarrow$ ^{13}B (θ_L = 2.0°) + X, (d) ^{15}N (67.3 MeV/A) + ^{93}Nb $\rightarrow$ ^{13}B (θ_L = 2.5°) + X, (e) ^{15}N (68.0 MeV/A) + ^{27}Al $\rightarrow$ ^{12}B (θ_L = 1.0°) + X. The momentum of the projectile is given by p_0, and the momentum of the outgoing fragment is p. Data are taken from [13].

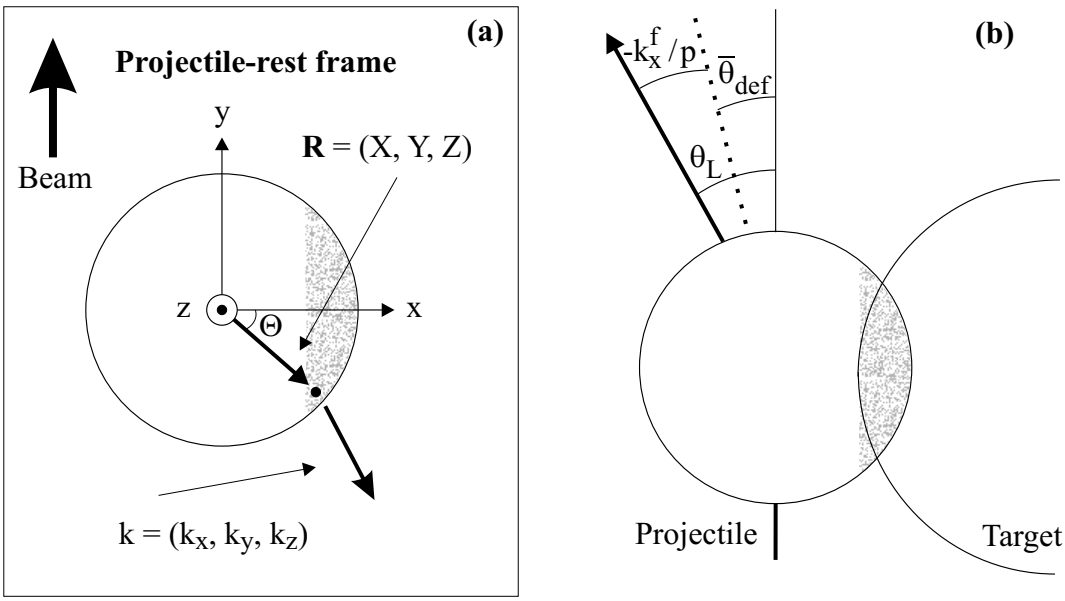

Figure 2.4: Variable definitions (adapted from Ref. [13]).

since the portion having $\mathbf{L} = -\mathbf{R} \times \mathbf{k}$ is removed. The definitions of $\mathbf{R}$ and $\mathbf{k}$ are the same as above and are shown in Figure 2.4(a). If the nucleon removal takes place uniformly over the overlap region, $X \approx R_0$, the radius of the projectile, and $Y \approx 0$, then $l_z \approx -R_0 k_y$. This leads to the zero crossing of P at p_0 since $k_y = 0$ in the projectile rest frame. However, if Y is not zero, l_z can take on non-zero values even at p_0 due to the Y k_x contribution in l_z (see Equation 2.2).

The final scattering angle of the fragment is given by the sum of the mean deflection angle ($\bar{\theta}_{def}$) and the change in angle caused by the transverse momentum component from the abraded nucleons (see Figure 2.5). This additional angle, $\Delta\theta$, is given by

$$\Delta\theta = \tan^{-1}(k_x^f/p) \tag{2.3}$$

so

$$\theta_L = \bar{\theta}_{def} - \tan^{-1}(k_x^f/p) \tag{2.4}$$

where θ_L is the fragment angle, k_x^f is the x-component of the linear momentum of the fragment and p is the total momentum of the fragment. The linear momentum of the

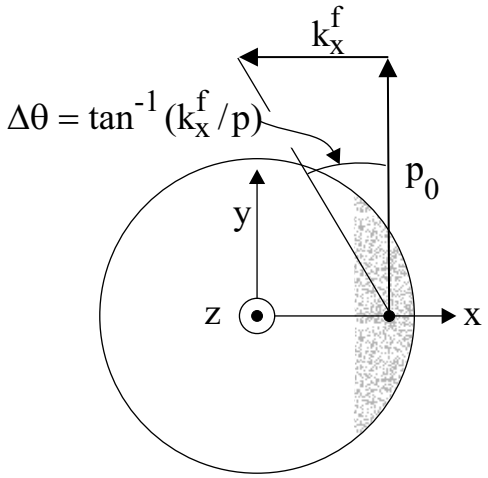

Figure 2.5: Schematic diagram of the angular impulse imparted to the fragment by the removed nucleons. k_x^f is the x-component of the fragment momentum, p_0 is the momentum of the incident projectile.

fragment and the momentum of the removed portion are related through a sign (i.e. $k_x = -k_x^f$). Thus, a positive k_x will result in a negative k_x^f, which must, according to Figure 2.4, serve to increase the scattering angle. This is the source of the minus sign in Equation 2.4.

In experiments, k_x will take on positive values since θ_L (the emission angle) is often set larger than the mean deflection angle, $\bar{\theta}_{def}$ (see Figure 2.4 (b)). If the average location of the removed nucleons is given by $X = R_0 \cos\Theta$ and $Y = -R_0 \sin\Theta$, where $\Theta > 0$ is the rotation angle (see Figure 2.4), Y k_x will yield a nearly constant negative polarization over a wide momentum range (k_x is positive and Y is negative independent of the momentum). This property accounts for the fact that P tends to be negative in reactions where $\bar{\theta}_{def} \approx 0$ (see Figure 2.3, Panels b-d). This is the extent of the KMA. The following sections contain a discussion of how the KMA was implemented to calculate polarization.

2.2 East Lansing Monte Carlo Polarization Code (ELPC)

Previously, Okuno *et al.* developed a Monte Carlo code to calculate polarization based on the KMA [13]. In this code (referred to herein as the Tokyo Polarization Code or TPC), the momenta of the removed nucleons were computed in Monte Carlo fashion and the KMA was used to calculate the polarization. To determine the position of the removed nucleons, the TPC used $X = R_0 \cos\Theta$ and $Y = -R_0 \sin\Theta$, where again $\Theta > 0$ is the rotation angle. This application insured that the removed nucleons only came from the surface of the projectile, as is required in peripheral collisions.

The TPC could achieve qualitative agreement with data, but quantitative results were lacking. The calculated magnitude was significantly greater than the experimental polarization magnitude. For example, scaling factors of 0.25 were required to match the calculated polarization to data in Ref. [13]. A more thorough implementation of the KMA into a Monte Carlo fragmentation code was required to adequately calculate polarization.

We have developed a Monte Carlo code based on the KMA in order to make more quantitative polarization predictions. This Monte Carlo code will herein be referred to as the East Lansing Polarization Code, or the ELPC. The ELPC takes as input parameters the mass of the target and projectile, the energy of the beam, the fragment angle, the impact parameter and the mean deflection angle. Calculation of the mean deflection angle requires the mass and charge of the target and projectile, the beam energy, the point of closest approach and the real part of the optical model potential as input parameters; see Appendix A. The production of the final nucleus involves both fragmentation and evaporation. The fragment polarization is then calculated using the KMA in an extended Monte Carlo framework as the z-component of angular momentum over the total angular momentum ($l_z/|\mathbf{L}|$) for each event and binned into

histograms.

Details on the abrasion process as it is handled by the ELPC as well as the improvements added to the KMA in the ELPC are discussed below.

2.2.1 Abrasion of Nucleons

The ELPC calculates the number of nucleons removed through the abrasion step using the equations given by Gosset *et al.* [14]. This method is based on the volume of intersection of a cylinder and a sphere where the number of nucleons removed is directly proportional to the overlap volume. These equations allow for several outcomes including a cylindrical groove of radius equal to the target radius cut into the projectile, a circular hole the size of the target punched through the projectile, and even complete obliteration of the projectile depending on the radius of the target, the radius of the projectile, and the impact parameter b separating the centers of the two objects. All of these options are available in the code, although the cases considered in this work are all peripheral collisions.

A removal position is calculated for each nucleon in the overlap region and these positions are then averaged together to give the position of the group of removed nucleons. This is necessary to maintain the integrity of the KMA; a group of nucleons is removed and it is this group that has a position and an angular momentum, not each individual nucleon. The single angle Θ previously used by the TPC to calculate removal positions was unsatisfactory, because the removal position was exactly the same for each and every event.

For the first implementation in the ELPC, the individual position of each nucleon was a random number limited only to the volume of intersection of two spheres, the target and the projectile. This yielded positions evenly distributed throughout the overlap region (i.e. average x positions that are positive, and average y and z positions of zero) in true Monte Carlo fashion. However, as examination of rescattering

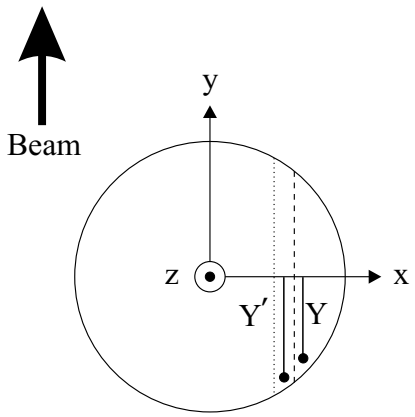

Figure 2.6: Schematic diagram of the average nucleon removal position in the projectile. Y′ is the y-coordinate for the position of the removed nucleons for the area bound by the dotted line, and Y is the coordinate for the smaller area bound by the dashed line.

by Okuno *et al.* [13] suggested that the average y-position be shifted backward in the projectile, i.e. the y-position should be less than zero (see Equation 2.4). Given the coordinate system where positive y is defined along the beam axis, the point of first contact with the projectile is at negative y positions in the fragment. This was implemented in the ELPC by providing an offset for the y-position while still maintaining the requirement that the position be within the overlap region.

A difficulty with this arrangement is that the y-offset is now a user-defined parameter. A y-offset of 1.0, giving the best agreement with data [13], is applicable for all general reactions. The sole exception is the data on the ^{93}Nb(^{18}O,^{12}B)X reaction [15] where a y-offset equal to 1.3 was found to be appropriate. The main difference for this reaction is that more nucleons are removed from the projectile. More nucleons removed requires a larger overlap volume, which in turn suggests the y position should be more negative, as shown in Figure 2.6. The area bound by the dashed line corresponds to a smaller overlap volume and thus has a smaller magnitude y-coordinate for the position than the area bound by the dotted line which corresponds to a larger overlap volume. A more negative y-coordinate for position corresponds to a larger y-offset.

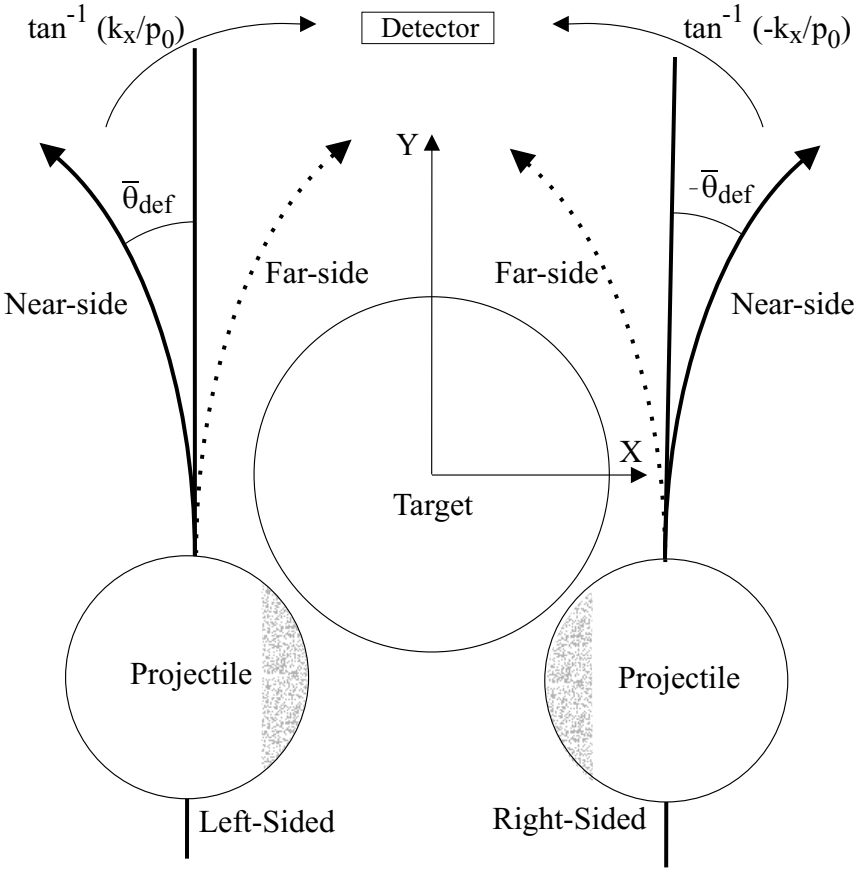

Figure 2.7: Schematic diagram of right- and left-sided collisions. The dotted lines are far-side interactions and the solid lines are near-side interactions.

As mentioned above, the interaction of the target and projectile is a fast, peripheral interaction. Fast means the reaction happens quickly (10^{-23} sec) and is a non-equilibrium process. Peripheral means the impact parameter is greater than zero, i.e. the projectile and target collide in an orientation other than head-on. For a peripheral interaction (in a plane), the projectile can interact with the target in two configurations: one where the projectile is on the left side of the target and one where the projectile is on the right side of the target (see Figure 2.7).

With the 'sided-ness' of peripheral collisions on one hand and the possibility of near- or far-side collisions (determined by positive or negative mean deflection angles, respectively) on the other, it was important to impose an absolute coordinate system on the calculations to maintain the correct relationship between the sign of the po-

larization, the emission angle of the fragment, and the momentum of the fragment. Thus, positive y is the beam direction, positive x is defined to the right of the target relative to the beam direction and positive z is perpendicular to the scattering plane forming a right-handed coordinate system. Positive angles are defined to the left of the y-axis, or toward negative x (see Figure 2.4). In most reactions, the fragments are collected at a positive angle relative to the incident beam direction of 0°. For left-sided interactions, a near-side(far-side) collision will scatter to the left(right), or to positive(negative) angles. For the interactions on the right of the target, a near(far)-side interaction must scatter to the defined negative(positive) angles, thus the signs of the mean deflection angles are changed within the code for these events.

After the group of removed nucleons is assigned an average removal position, the polarization is calculated via the KMA. The linear momentum (x-, y- and z-components) of the group of removed nucleons is calculated using a Gaussian distribution centered at zero with a width given by the Goldhaber formula [16],

$$\sigma = \sigma_0 \sqrt{A_{\mathrm{F}}(A_{\mathrm{P}} - A_{\mathrm{F}})/(A_{\mathrm{P}} - 1)} \tag{2.5}$$

where A_F is the fragment mass, A_P is the projectile mass and σ_0 takes on a value of about 80 MeV/c, slightly smaller than values obtained at relativistic energies [17].

The trajectory of the fragment is calculated by adding the mean deflection angle (see Appendix A for mean deflection angle calculation) to the change in angle caused by the transverse momentum component of the abraded nucleons (review Figure 2.4b and Equation 2.4). Typical $\bar{\theta}_{\mathrm{def}}$ values for most reactions fall within the range of $-3°$ to $+3°$. Values for the additional angle caused by the removed nucleons range from $-4°$ to $+4°$ for ^{197}Au(^{14}N,^{12}B)X at 39.4 MeV/A. This value comes from the linear momentum for the removed nucleons, which in turn is a Gaussian distribution about zero.

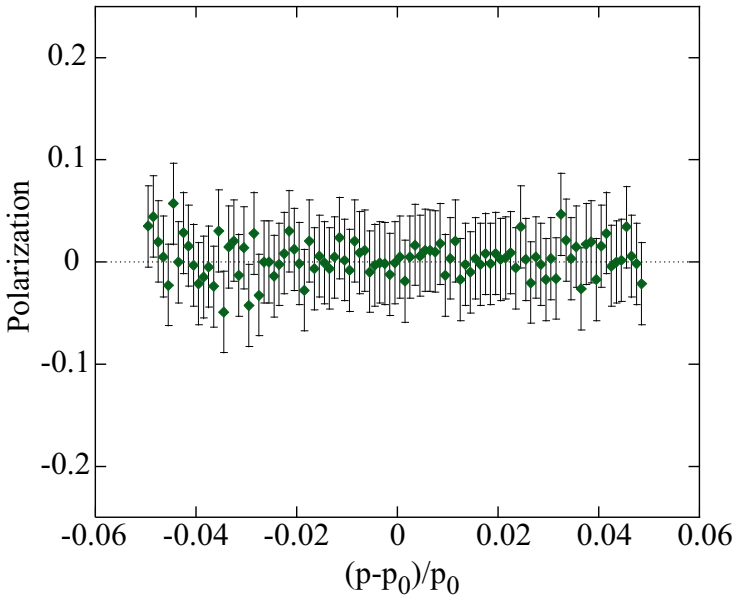

Figure 2.8: Calculated polarization as a function of relative fragment momentum for the fragmentation of 80 MeV/A ^{18}O in a target of ^{93}Nb to make ^{12}B at a fragment angle of 0°. p_0 is the momentum of the incident projectile and p is the momentum of the outgoing fragment.

Once the angle of the fragment is known, it can be determined whether the fragment makes it into the angular acceptance window, i.e. whether the fragment makes it to the 'detector'. If the fragment is within the acceptance window, the polarization for this event is histogrammed, if not, the event is ignored. The polarization is binned on the basis of the total number of nucleons removed, and at the end, the polarization is averaged for each momentum bin.

One of the fundamental phenomena in fragmentation reactions related to polarization is that no fragment spin polarization is observed at a fragment angle of zero degrees. Thus, a good Monte Carlo calculation of the polarization should yield zero polarization at a zero degree fragment angle. Shown in Figure 2.8 is the calculated polarization for 80 MeV/A ^{18}O fragmented in a target of ^{93}Nb to make ^{12}B at a fragment angle of 0°. The calculated polarization is equivalent to zero within the statistical error for the calculation. It is the allowance of right- or left-sided collisions that correctly accounts for the observed absence of spin polarization at an incident

beam angle of 0° (see Figure 2.7). Half of the events detected at 0° are from a right-sided interaction, and the other half are from left-sided interactions which will give fragments with polarization equal in magnitude to the right-sided events but opposite in sign, for an overall average of zero polarization. The lack of right- and left-sided interactions is one of the factors that limited the TPC from being able to calculate zero polarization at a 0° fragment angle.

2.2.2 Additions to the KMA in the ELPC

Since the TPC over-predicted the magnitude of the experimental polarization, it was important to identify shortcomings or assumptions within the TPC that may not be valid. The goal was essentially to explore the KMA to its fullest potential. The following sections give details on the implementation of angular distributions, out-of-plane acceptance, evaporation and γ-ray de-orientation in the ELPC that permit a more quantitative treatment of polarization in projectile fragmentation.

Angular Distribution Correction

The calculation of the mean deflection angle (see Appendix A) corresponds to one particular impact parameter, i.e. to a particular number of nucleons removed in the abrasion step. The original incarnation of the trajectory calculation (in the TPC) had a fragment scatter to a single mean deflection angle based on the number of nucleons removed plus the angular impulse given to the fragment by the x-direction linear momentum transfer (see Figure 2.5). This was a reasonable assumption to begin with, but the mean deflection angle is just that - a mean or average angle. For a given number of nucleons removed, fragments will actually scatter to a range of angles whose mean is the mean deflection angle for that particular number of removed nucleons. Thus, a distribution for the deflection angle whose average is the calculated mean deflection angle was incorporated into the ELPC. Equation 2.3, which governs

the final scattering angle of the fragment, was modified so that $\bar{\theta}_{\rm def}$ was replaced with $\theta_{\rm def}$, the specific deflection angle for an individual interaction.

Several different shapes for this deflection angle distribution were considered. The first choice was a Rutherford distribution. The Rutherford distribution describes classical elastic scattering and is strongly peaked at zero degrees. This distribution was problematic because fragmentation reactions are not classical elastic scattering, and the Rutherford distribution is incompatible with a mean angle larger than about 1°. An alternative distribution was a negatively-sloped straight line. A straight line is the second simplest approximation that can be made besides a constant or flat angular distribution. Such a line distribution is peaked at zero degrees, and by changing the slope, the correct average angle can be imposed on the distribution. A calculated angular distribution with $\bar{\theta}_{\rm def} = 3°$ is shown in Figure 2.9. The calculated polarization is shown as a function of momentum for 39.4 MeV/A ^{14}N fragmented in ^{197}Au to make ^{12}B ($\theta_{\rm L} = 5.0°$) and for 68 MeV/A ^{15}N fragmented in ^{27}Al to make ^{12}B ($\theta_{\rm L} = 1.0°$) with both the single mean deflection angle and the linear deflection angle distribution in Figure 2.10. The calculated magnitude of the polarization is reduced by about 10% for both reactions when using a linear distribution for the deflection angle.

Other shapes for the angular distribution were also investigated. Among them was a step function distribution from zero out to twice the mean deflection angle, which has an average value equal to the mean deflection angle. The step function distribution offered no improvement in the calculated polarization over the straight line distribution, and it gave a non-physical angular distribution. In particular, the maximum number of fragments did not occur at 0° as observed in experiment. Another candidate distribution was one shaped like a Fermi function (i.e a Woods-Saxon shape),

$$\mathrm{f}(\theta_{\rm def}) = \frac{1}{1 + \mathrm{e}^{(\theta_{\rm def} - \mathrm{x})/\mathrm{a}}} \tag{2.6}$$

where $a = 0.5$, θ_{def} is the scattering angle and the value of x is varied to make the

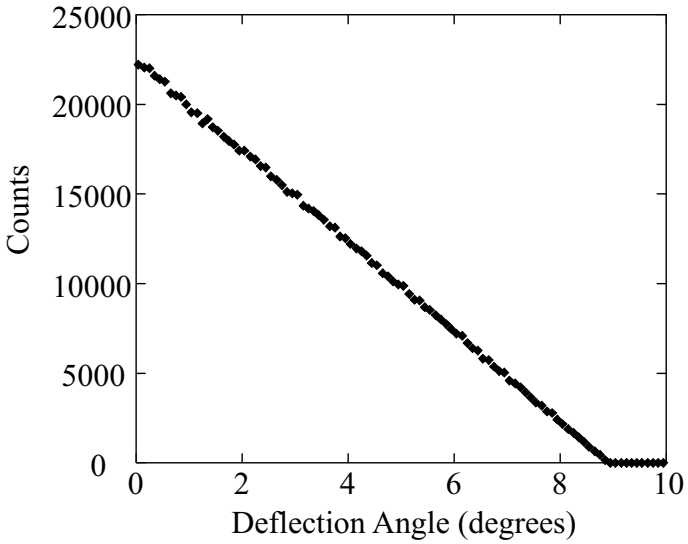

Figure 2.9: Linear angular distribution with $\bar{\theta}_{\mathrm{def}} = 3°$.

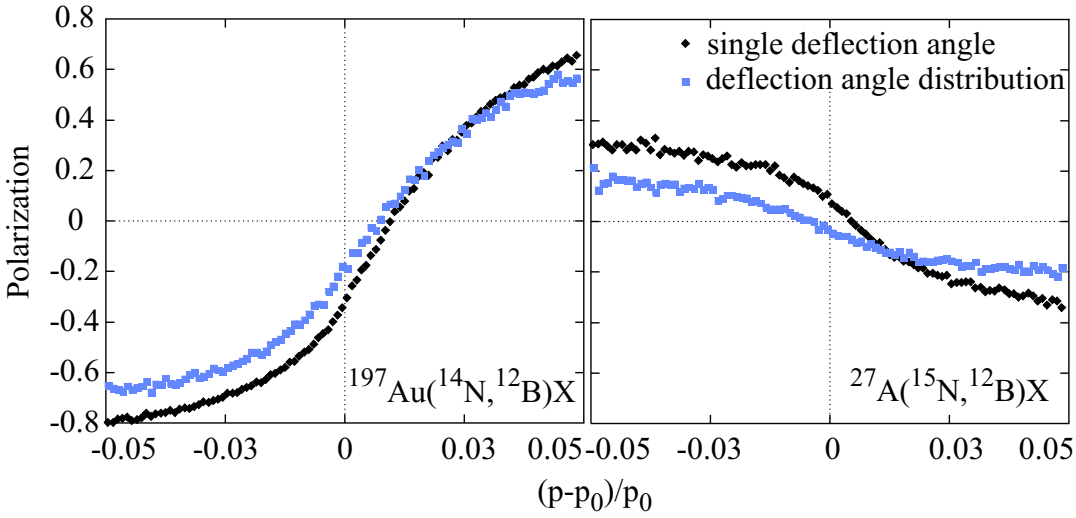

Figure 2.10: Polarization calculated as a function of relative fragment momentum. The left panel is ^{197}Au(^{14}N, ^{12}B)X at 39.4 MeV/A and the right panel is ^{27}Al(^{15}N, ^{12}B)X at 68 MeV/A. The black diamonds are calculated with a single mean deflection angle and the blue squares are calculated with a deflection angle distribution. (Some images in this dissertation are presented in color.)

mean of the distribution equal to the mean deflection angle. The correct mean for the distribution could only be achieved with a negative value for x, which is completely unphysical. Consequently, this distribution was judged inferior to the others and abandoned in favor of the straight line distribution.

Out-of-Plane Acceptance Correction

Another potential source of the over-prediction of the polarization in the TPC was associated with the deflection angle. Whether or not the fragments lead to products that reach the detector depends on the out-of-plane angular acceptance of the system. The coordinate system for the reaction as shown in Figure 2.4 has the reaction take place solely in the x-y plane. The beam travels along the y-axis and is scattered in either the positive- or negative-x direction, perhaps producing some polarization in the z-direction. However, the fragments should more realistically be able to interact with the target on the top, the bottom and all the angles in between, not just on the right or left side of the target in the horizontal x-y plane. Interactions of this sort are referred to as non-equatorial collisions. A non-equatorial collision would serve to decrease the z-component of angular momentum in the equatorial (or horizontal x-y plane) frame, as is depicted in Figure 2.11. The primed frame in the figure represents non-equatorial scattering and can be represented by a rotation of the coordinate system about the y-axis through the angle β (this is equivalent to rotating the x-y reaction plane). $\mathbf{L}$ is the angular momentum vector where $\mathrm{L_z}$ and $\mathrm{L'_z}$ are the z-components of $\mathbf{L}$ in the beam axis frame. $\mathrm{L'_z}$ can be written in terms of $\mathrm{L_z}$:

$$\mathrm{L'_z} = \mathrm{L}\cos(\alpha+\beta) = \mathrm{L}\cos\alpha\cos\beta - \mathrm{L}\sin\alpha\sin\beta. \tag{2.7}$$

Since $\mathrm{L}\cos\alpha = \mathrm{L_z}$ and $\mathrm{L}\sin\alpha = \mathrm{L_x}$, this becomes

$$\mathrm{L'_z} = \mathrm{L_z}\cos\beta - \mathrm{L_x}\sin\beta. \tag{2.8}$$

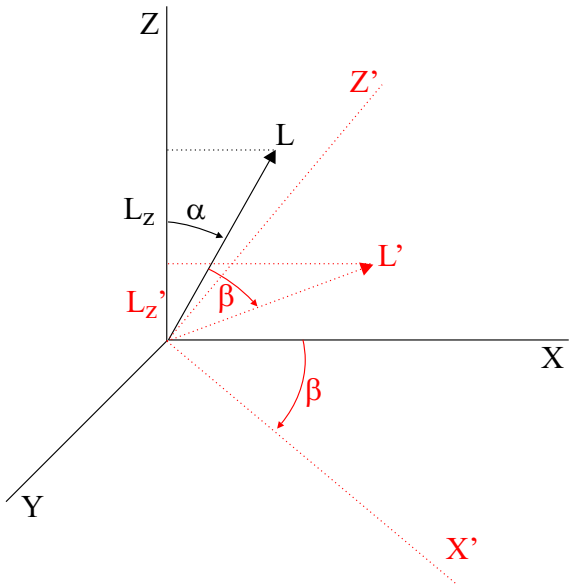

Figure 2.11: Representation of non-equatorial scattering of fragments (red, primed axes) and the scattering of fragments purely in the horizontal x-y plane (black, unprimed axes). Labels defined in the text.

The angle β ranges, in theory, from $-\pi/2$ to $+\pi/2$, because the fragment can scatter anywhere around the y-axis above and below the plane. Integrating all the possible contributions from the out-of-plane acceptance, and including a $1/\pi$ normalization factor from the interval of integration gives

$$L'_z = \frac{1}{\pi}\int_{\frac{-\pi}{2}}^{\frac{\pi}{2}} (L_z \cos\beta - L_x \sin\beta)d\beta = \frac{2}{\pi}L_z. \tag{2.9}$$

However, experimental devices have a limited angular acceptance, and thus the range on β will be smaller than $-\pi/2$ to $+\pi/2$. Figure 2.12 shows a schematic plot of the beam view of an angular acceptance window of $2°\pm0.5°$ horizontally and $\pm2°$ vertically. The out-of-plane acceptance of $\pm2°$ limits the range on β to $-53°$ to $+53°$ for this case. Equation 2.9 with these limits of integration and a normalization of $106°$ rather than of $180°$ gives $L'_z = 0.86\ L_z$. As the acceptance window moves further from the beam axis due to an increased fragment angle, the range on the angle β will decrease. This causes the value of L'_z to approach that of L_z. In most cases in this

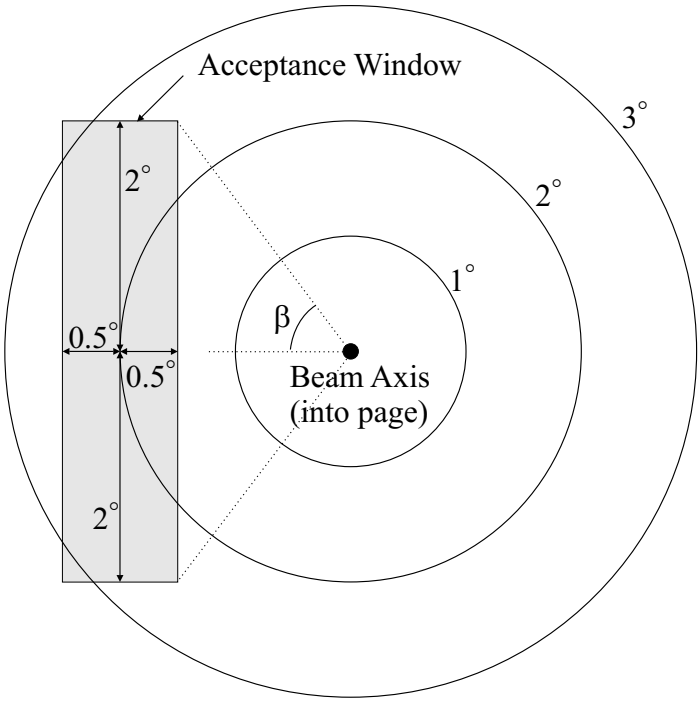

Figure 2.12: Representation of the angular acceptance window from a beam view. The fragment angle acceptance (horizontal acceptance) is 2°±0.5° and the vertical acceptance is ±2°.

Table 2.1: Corrective factors on the polarization due to non-equitorial scattering.

fragment angle (°)	β (°)	correction
2.0±0.5	53	0.86
5.0±2.5	39	0.92
4.0±2.5	53	0.86
2.0±2.5	90	0.64
1.0±2.5	90	0.64

work, the fragment angle acceptance is quite large, ±2.5°, which, when coupled with a small fragment angle, causes the acceptance window to extend to the beam axis giving an angular range on β of $-\pi/2$ to $+\pi/2$. Various example acceptance windows, β angles (i.e. ranges on β) and the resulting corrections for L_z in terms of L'_z are listed in Table 2.1 assuming ±2° vertical angular acceptance in all cases.

A factor of $2/\pi$ has been included in the ELPC as a multiplicative factor on the polarization. This value was chosen as a minimum value. As shown in Table 2.1, different angular acceptance windows could slightly increase this value.

Evaporation of Nucleons

In the framework of the abrasion-ablation model of fragment production that is the base of the KMA, the primary fragment receives some excitation energy (along with the linear and angular momenta). The primary fragment will undergo a statistical evaporation process emitting nucleons and then γ-rays, all of which can depolarize the angular momentum. The extent of the excitation energy and the consequent de-excitation are model dependent. The excitation energy for the ELPC is based on the statistical hole-energy model of Gaimard and Schmidt [18]. The statistical hole-energy theoretical model predicts an average of 13.3 MeV of excitation energy imparted to the fragment for every abraded nucleon. This value is an estimate of the average energy of single-particle levels vacated during the abrasion process relative to the Fermi surface of the projectile. The experimental work of Schmidt *et al.* [19] suggested the larger evaporation energy of 27 MeV per abraded nucleon. However, this value comes from an attempt to reproduce the cross sections over a large mass range for heavy isotopes (neutron number 95 to above 115) produced from heavy (^{197}Au) projectiles. Since the 13.3 MeV value comes from a general treatment, and the value deduced by Schmidt *et al.* is for nuclei well outside the mass regime of the ELPC, the lower value was adopted for these polarization calculations. However, this excitation energy is an input parameter in the ELPC and can be changed to accommodate heavier fragments.

During the abrasion step, the ELPC determines the number of removed nucleons. The mean excitation energy resulting from the abrasion step is calculated based on the number of abraded nucleons. A Gaussian distribution around this mean excitation energy is assumed with a width based on the examples given by Gaimard and Schmidt [18], similar to calculations by Friedman *et al.* [20]. This width is given by

$$\sigma = 4.928 \times \mathrm{x} + 27.214 \tag{2.10}$$

where σ is the width of the Gaussian and x is the number of abraded nucleons. This Gaussian distribution in excitation energy is then used as a probability distribution to allow variability in the number of nucleons evaporated, since the 13.3 MeV of excitation energy per abraded nucleon is an average value, not an absolute value. According to Ref. [18], 20 MeV of excitation energy is required to evaporate each nucleon. The number of nucleons evaporated is then given by the excitation energy divided by 20.0 where the result of this operation is truncated to the nearest lower integer. This procedure assures that the number of evaporated nucleons can range from zero to the maximum allowed based on the excitation energy while allowing for statistical variation in true Monte Carlo fashion. It is necessary to note that evaporation has been studied for many years within the framework of statistical models [21, 22]. However, the microscopic treatment of these works was more detailed than that consistent with the KMA. Therefore, the more 'average' approach with the evaporation of $13.3/20 = 0.665$ nucleons per abraded nucleon was employed in the ELPC.

After the number of evaporated nucleons is determined, each evaporated nucleon is assigned a random position on the surface of the spherical fragment. Evaporation in the ELPC is treated isotropically and evaporated nucleons are assigned a linear momentum equal to 194 MeV/c oriented normal to the surface. This value of 194 MeV/c is equivalent to the 20 MeV excitation energy required to evaporate each nucleon. This means each nucleon carries all of its excitation energy - none is lost to the fragment in overcoming the binding energy or in exiting the fragment. This choice is somewhat of an overestimate, but it will maximize any depolarization. Because the abrasion step endows the fragment with angular momentum, the evaporated nucleon will also have a component of momentum tangential to the surface of the spherical fragment at the point of evaporation. A calculation of this tangent vector can be found in Appendix B. The total momentum for the evaporated nucleon will be the

sum of the tangential component and the perpendicular component,

$$P^{i}_{total} = P^{i}_{perpendicular} + P^{i}_{tangential} \tag{2.11}$$

where i = x, y, or z. The angular momentum of each evaporated nucleon is calculated by taking the cross product of the evaporated nucleon's position and total linear momentum. Calculating the angular momentum in this manner is a little unconventional but follows the mechanical picture of the KMA. This process is repeated for each evaporated nucleon and the angular momentum values are summed. In order to conserve angular momentum, this total angular momentum value for the evaporated nucleons is subtracted from the original x-, y-, and z-components of angular momentum of the parent fragment to generate the final components of angular momentum for the fragment.

$$l^{i} = l^{i}_{fragment} - l^{i}_{evap} \tag{2.12}$$

where i = x, y, or z. $l_{fragment}$ is the angular momentum of the fragment following the abrasion step, and l_{evap} is the angular momentum of the evaporated nucleon. The polarization as $l_z/|\mathbf{L}|$ is then re-calculated with these new values of angular momentum.

In addition to the angular momentum, the total linear momentum must also be conserved. The linear momentum values for each evaporated nucleon are subtracted from the original components of linear momentum for the fragment before evaporation,

$$p^{i} = p^{i}_{fragment} - p^{i}_{evap} \tag{2.13}$$

where i = x, y, or z. These final linear momentum values are histogrammed and can be compared to experimental linear momentum distributions. Reactions where more nucleons are removed have broader momentum distributions [23]. Shown in Figure 2.13 are the calculated momentum distributions for 80 MeV/A ^{18}O in a ^{93}Nb target

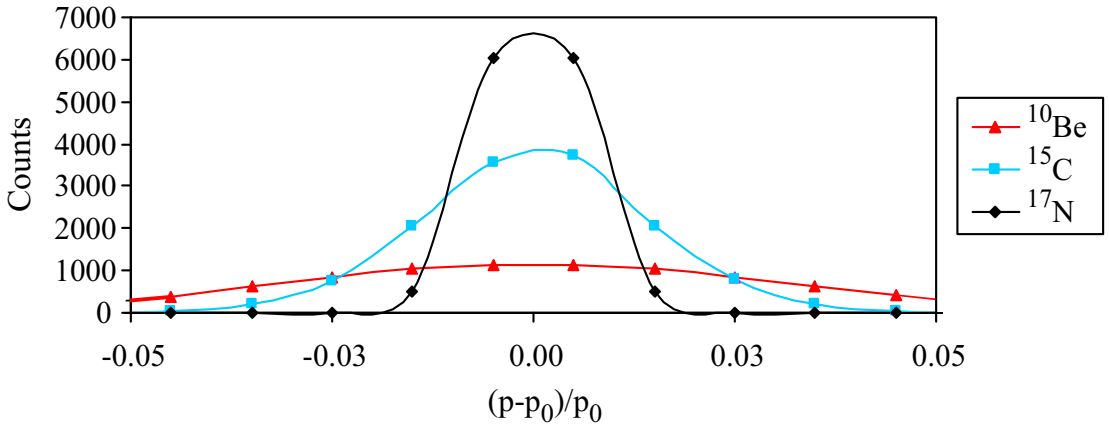

Figure 2.13: Calculated fragment momentum distributions for the fragmentation of 80 MeV/A ^{18}O in a target of ^{93}Nb at a beam angle of 3°. p_0 is the momentum of the incident projectile and p is the momentum of the outgoing fragment. The red triangles are for ^{10}Be, the blue squares for ^{15}C and the black diamonds are for ^{17}N.

to produce ^{10}Be, ^{15}C and ^{17}N at a 3° fragment angle. As more nucleons are removed, the calculated momentum distributions broaden.

Furthermore, this requirement of conserved linear momentum during evaporation can change the trajectory of the fragment. The equal and opposite amount of linear momentum from the evaporated nucleons imparts a change in the angular trajectory of the fragment. This change is calculated in the same manner as above (equation 2.4) with the exception that the linear momentum for the fragment after evaporation is used in place of p, the fragment momentum before evaporation, and the deflection angle is replaced by the angle of the fragment after the abrasion step. Thus,

$$\theta_L^{new} = \theta_L^{old} - \tan^{-1}(k_x^{evap}/p^{evap}). \tag{2.14}$$

Fragments with the appropriate angular trajectory are accepted into the detector window and grouped on the basis of the total number of nucleons removed from both the abrasion step and the evaporation step. For each number of removed nucleons, the polarization is binned on the basis of relative fragment linear momentum, and at the end, the polarization is averaged for each linear momentum bin.

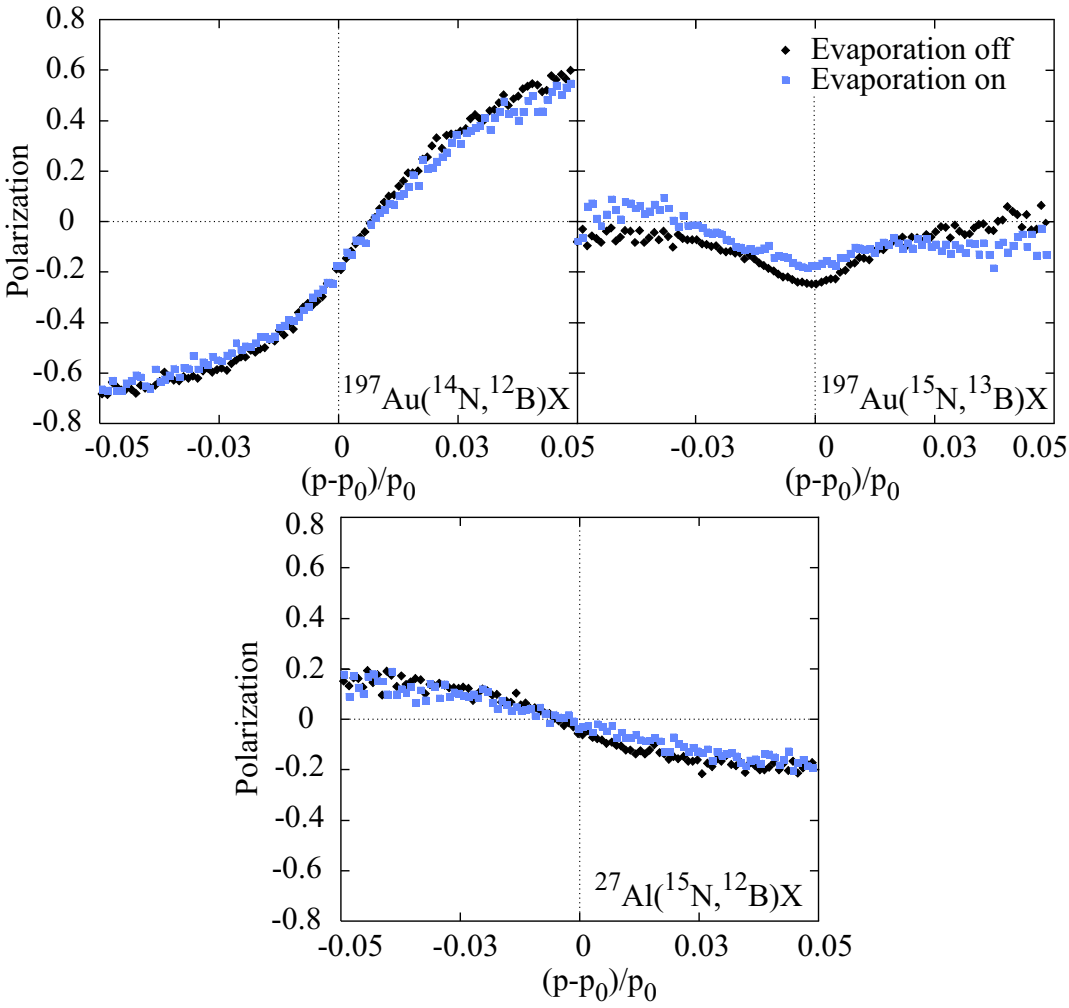

Figure 2.14: Polarization calculations as functions of relative fragment momentum for (a) ^{14}N (39.4 MeV/A) + ^{197}Au $\rightarrow$ ^{12}B ($\theta_L = 5.0°$) + X, (c) ^{15}N (109.6 MeV/A) + ^{197}Au $\rightarrow$ ^{13}B ($\theta_L = 2.0°$) + X, (e) ^{15}N (68.0 MeV/A) + ^{27}Al $\rightarrow$ ^{12}B ($\theta_L = 1.0°$) + X. The momentum of the projectile is given by p_0, and the momentum of the outgoing fragment is p. Black diamonds are calculations with evaporation off, blue squares are calculations with evaporation on.

The polarization calculated as a function of fragment momentum for three of the reactions studied by Okuno *et al.* [13] is shown in Figure 2.14. The black diamonds are the results of calculations with the process of evaporation excluded and the blue squares are the calculations with evaporation included. Evaporation only slightly decreases the calculated magnitude of polarization, demonstrating that evaporation does not play a significant role in the reaction processes for these light nuclei. This is

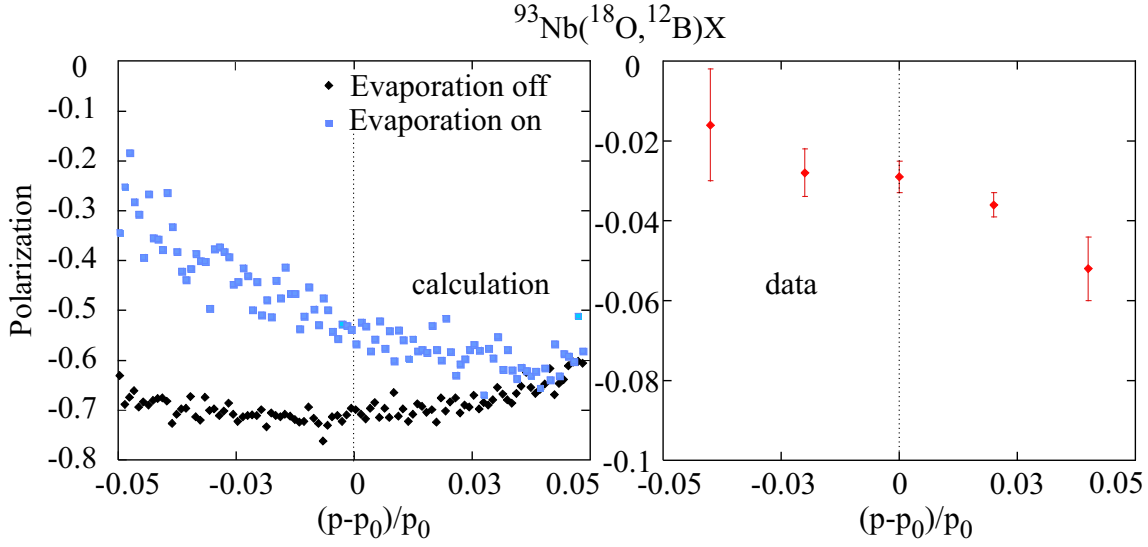

Figure 2.15: Calculated polarization (left) and polarization data (right) as functions of relative fragment momentum for the fragmentation of 80 MeV/A ^{18}O in a target of ^{93}Nb to make ^{12}B at a fragment angle of 3°. p_0 is the momentum of the incident projectile and p is the momentum of the outgoing fragment. The black diamonds are the calculation with evaporation off and the blue squares are the calculation with evaporation on. Data are taken from [15]

attributed to the small number of nucleons removed from the projectile to make the fragment. The reactions studied by Okuno *et al.* were chosen to specifically limit the influence of evaporation. Fragment masses that differ significantly from the beam are expected to be more dependent on evaporation.

Shown in Figure 2.15 are both polarization calculations and data for the fragmentation of 80 MeV/A ^{18}O in a target of ^{93}Nb to make ^{12}B at a fragment angle of 3°. Since this reaction removes six nucleons, evaporation is likely to play a larger role than in previous cases. Examination of Figure 2.15 shows this to be the case within the ELPC. Not only does the incorporation of evaporation decrease the magnitude of the polarization, it also changes the slope of the polarization dependence on fragment momentum. For the case of ^{12}B produced from ^{18}O, a qualitative agreement with data is achieved. Thus, the inclusion of evaporation may be important for reactions where many nucleons are removed.

Gamma Ray De-Orientation Correction

After the evaporation of nucleons, the fragment may be left with some amount of excitation energy ranging from 0 MeV up to 20 MeV, the evaporation threshold. One potential pathway to remove this excitation energy is through γ-ray emission. Emitted γ-rays have the potential to de-orient the fragment. The presence of γ-rays produced by fragmentation reactions is a subject open for some debate. Experimental in-beam γ spectroscopy on isotopes produced in fragmentation reactions have detected a significant exponential background and a few discrete γ-rays from low-lying excited states [24]. The composition of the exponential background is uncertain. Since fragmentation reactions are so violent, other processes that produce γ-rays may accompany the production of fragments. Examples include delta-rays, heavy-ion bremsstrahlung, and reactions from secondary protons, neutrons etc. The consequences of this high background are that it obscures weaker discrete γ-ray lines from fragments and it also renders the detection of statistical γ-rays from the de-excitation of the highly excited fragments impossible.

Other experiments have studied isomers produced in fragmentation reactions [25]. These isomer experiments are carried out remotely from the target which allows the detection of gamma rays in the absence of the prompt reaction background. The presence of isomers at high excitation energies, with spins upwards of $10\hbar$, implies that fragments can be produced in excited states, and that these fragments have the potential to decay to their ground states via the emission of γ-rays. Thus, it seems likely γ-rays from higher-lying states are indeed present in the in-beam spectroscopy γ-ray spectra, but they are hidden under the intense background. Therefore it is reasonable to expect that at least a few γ-rays are emitted from each fragment and the effects these gamma emissions have on the polarization will now be considered. (As an exception, it should be noted that certain nuclei with unbound states have been produced in fragmentation reactions. This implies these nuclei are produced in

the ground state with no excitation energy, and thus can emit no γ-rays.)

In order to include gamma-ray de-orientation in the ELPC, it was necessary to understand how γ-ray emission affects the polarization. De-orientation is usually discussed in terms of the statistical tensor [1] which specifies the orientation of each state:

$$\rho_k^{new} = U_k \rho_k^{old} \tag{2.15}$$

where the U_k are the de-orientation parameters which modify the orientation of the state. The ρ_1 statistical tensor is proportional to the polarization,

$$\rho_1 \propto \frac{l_z}{|\mathbf{L}|}. \tag{2.16}$$

Thus, the polarization can be multiplied by these U_1's for each radiative emission to propagate the de-orientation along a γ-ray cascade of arbitrary length. The U-coefficients depend on the initial state spin, the final state spin and the multipolarity of the emitted γ-ray for each transition [26]. For any cascade, the spin changes and polarization loss must be traced from the initial (or entry) spin and excitation energy to the ground state.

It can be anticipated that nuclear structure effects and the discrete level sequence at low energy will affect the γ-ray relaxation process on a case by case basis. However, as a first approximation, the decay can be generically treated by assuming a statistical cascade through a continuum of levels using a Monte-Carlo simulation similar to that described by Leander [27].

Within this Monte Carlo simulation, the nuclear level density is specified by a constant-temperature level-density formula with the parameters determined by von Egidy *et al.* [28] from fits to extensive data. No nuclear structure effects or specific discrete levels are included, and the transition rates in the continuum are given single-particle strength. No attempt was made to include enhanced E2 transitions or

collectivity in the continuum. This is justified as a first approximation because the nuclei of interest, which have relatively low masses, do not have strongly collective structures.

Beginning from a specified initial excitation energy and spin, the decay to the ground state is tracked. For each transition, the type (E1, E2 or M1) and spin change are determined by random numbers, as is the γ-ray energy. The γ-ray de-orientation coefficients are evaluated at each step and multiplied together to evaluate the cumulative loss of de-orientation along the path. The average de-orientation coefficient for each entry point is evaluated by repeating the random walk 10^6 times. Finally, a weighted average over the entry distribution in excitation energy and spin is made based on the output of the ELPC. The spin distribution is calculated with the ELPC by converting the total angular momentum generated in the fragmentation reaction (after the particle evaporation step) into units of $\hbar$. The excitation energy is taken as a uniform distribution on the interval 0 to 20 MeV which is a good approximation to the output of the ELPC. Further details of the technical aspects of the Monte-Carlo γ-ray de-orientation simulation will be presented elsewhere [29].

The de-orientation coefficients, average entry spins and average γ-ray multiplicities calculated using the above method for selected reactions are shown in Table 2.2. It is interesting to note that reactions producing fragments with odd spins are more likely to maintain their polarization for a given γ-ray cascade. This is due to the lack of spin 0 states in the level structure which give orientation parameters of zero. Based on the magnitude of the U-coefficients in the table, the γ-ray relaxation step has the potential to significantly de-orient the fragment.

Shown in Figure 2.16 is the final calculated polarization as a function of relative fragment linear momentum for several of the reactions presented above with γ-ray de-orientation included. No scaling factor was used. The calculations show remarkable agreement with data both in general behavior and in polarization magnitude. The

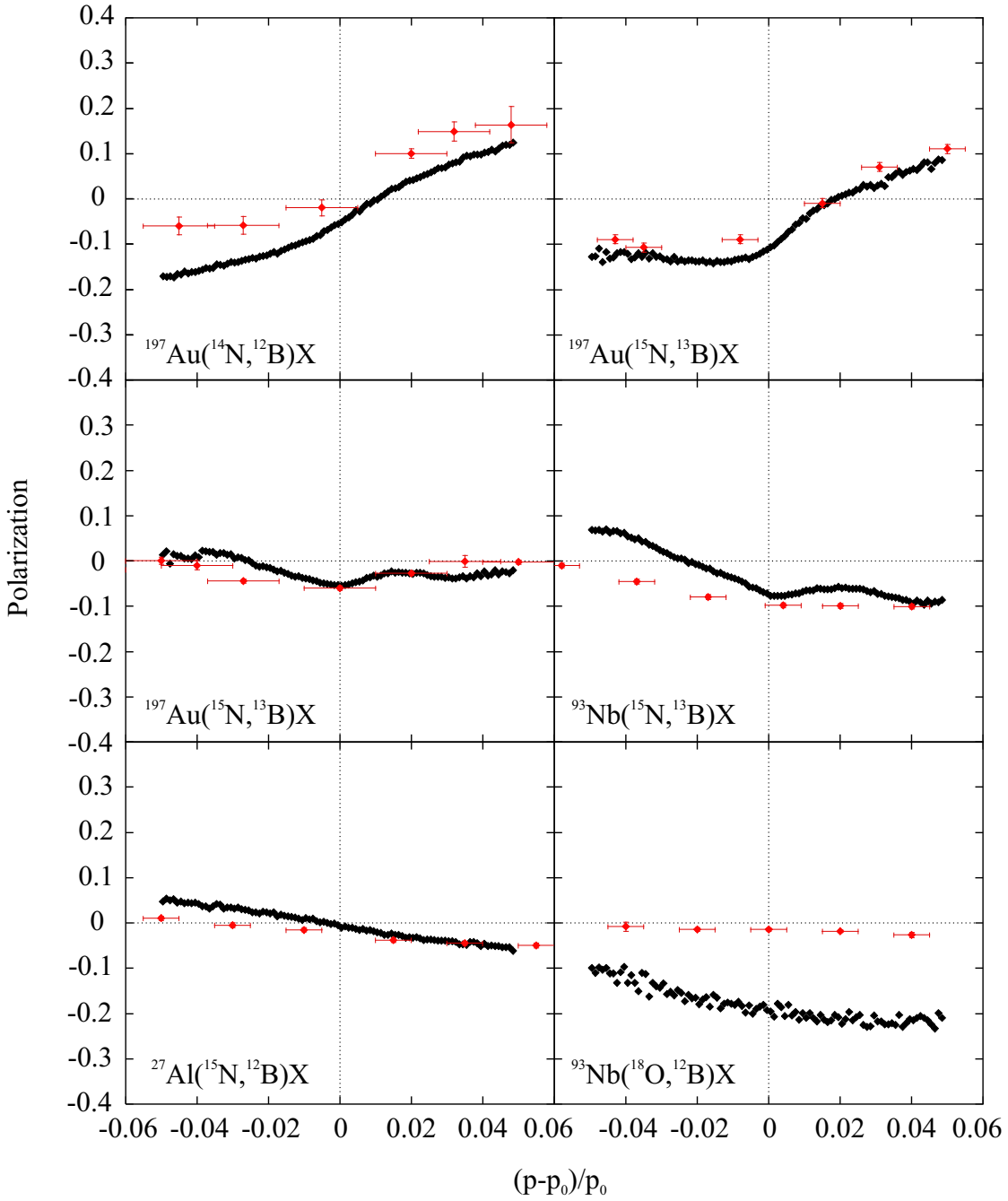

Figure 2.16: Final calculated polarization (black lines) including γ-ray de-orientation and polarization data (red points) as functions of relative fragment momentum for ^{197}Au(^{14}N, ^{12}B) at 39.4 MeV/A, ^{197}Au(^{15}N, ^{13}B) at 68 MeV/A, ^{197}Au(^{15}N, ^{13}B)X at 109.6 MeV/A, ^{93}Nb(^{15}N, ^{13}B)X at 67.3 MeV/A, ^{27}Al(^{15}N, ^{12}B)X at 68 MeV/A, ^{93}Nb(^{18}O, ^{12}B)X at 80 MeV/A. p_0 is the momentum of the incident projectile and p is the momentum of the outgoing fragment. Data are taken from [13, 15].

Table 2.2: De-orientation coefficients for selected reactions.

Reaction	Energy (MeV/A)	U_1	Avg Entry Spin	Multiplicity
^{197}Au(^{14}N, ^{12}B)X	39.4	0.368	1.30	2.33
^{197}Au(^{15}N, ^{13}B)X	109.6	0.511	1.52	2.37
^{27}Al(^{15}N, ^{12}B)X	68.0	0.473	1.96	2.52
^{93}Nb(^{18}O, ^{12}B)X	80.0	0.645	4.23	3.34

same polarization distributions as functions of momentum were calculated using the TPC in Ref. [13] required a scaling factor of 0.25 to be brought into agreement with the data.

2.2.3 Summary

The previous sections detail the development of the ELPC. The ELPC is a Monte Carlo simulation which calculates the polarization observed in fragmentation reactions with quantitative accuracy while maintaining the integrity of the KMA. The ELPC has been modified from the TPC in that it assigns individual positions to removed nucleons, and projectiles are allowed to interact on either side of the target. It has gone beyond the TPC in that fragments scatter to a deflection angle distribution rather than a single mean angle, and the out of reaction plane acceptance has been taken into account. The process of nucleon evaporation and its direct effects on the angular momentum of the fragment are included, as is any de-orientation due to γ-ray relaxation. The angular distribution implementation reduces the calculated polarization magnitude by about 10% and the out-of-plane acceptance reduces the polarization magnitude by about 30%. The calculated polarization magnitude is corrected by about 20% due to nucleon evaporation and by another 50% due to γ-ray de-orientation.

2.3 Predictions

A survey of the published polarization data reveals few experiments that have been performed to investigate systematic trends in polarization phenomena. However, with the complete ELPC to predict polarization, these various trends and behaviors can now be investigated with confidence. It is interesting to study the dependence of the polarization on the emission angle, the energy of the incident projectile, and the number of nucleons removed. These relationships will be examined in detail in the following sections.

2.3.1 Polarization vs. Fragment Angle

As the fragment angle increases, the production rate for the nucleus of interest is observed to decrease. The TPC could not reproduce this experimental observation. Shown in Figure 2.17 is the calculated (with the ELPC) and the experimental relationship between the number of counts and an increasing emission angle for 80 MeV/A ^{18}O fragmented on ^{93}Nb to produce ^{12}B. The number of events for the experimental data drops to $\approx 65\%$ of the maximum value at a fragment angle of 2°. The calculated number of events drops to $\approx 80\%$ of the maximum value at 2°. This discrepancy may be related to the simplicity of the deflection angle distribution employed within the ELPC. A negatively-sloped straight line peaked at 0°, although correct in a gross or average way, is not entirely realistic. A more exact angular distribution formalism within the code would alleviate this problem. However, the code does presently reproduce the proper trend for the number of counts relative to the changing fragment angle.

Conventional wisdom holds that a larger fragment emission angle (or beam angle) corresponds to larger polarization magnitude produced in any given reaction. Measurements by Matsuta *et al.* [30, 31] support this notion. Shown in Figure 2.18 is the

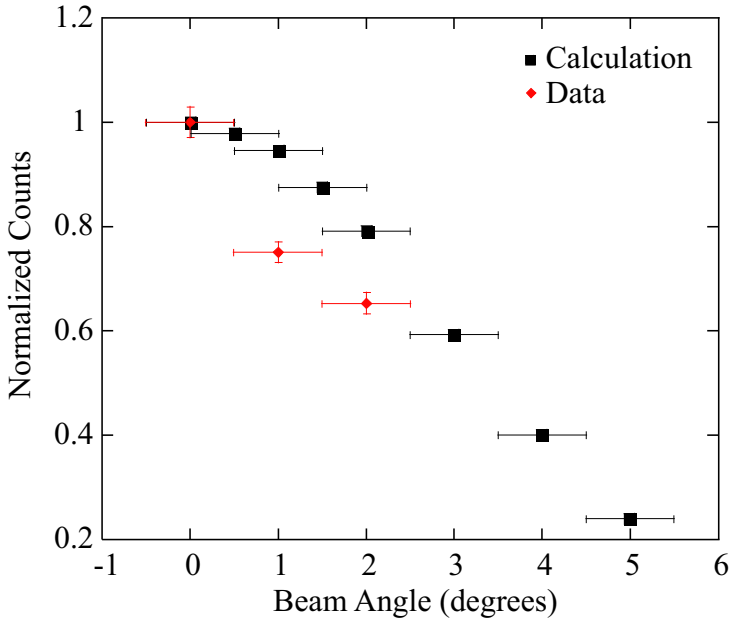

Figure 2.17: Calculated and experimental normalized counts as a function of fragment angle for the fragmentation of 80 MeV/A ^{18}O on ^{93}Nb to produce ^{12}B.

polarization at $-1.00\pm0.05\%$ relative fragment momentum calculated as a function of fragment angle for two reactions, the ^{197}Au(^{49}Ca,^{37}K) reaction Matsuta studied and ^{197}Au(^{14}N,^{12}B). In both cases the calculated polarization magnitude increases slightly as the fragment angle increases. This behavior can be understood considering the flight angle of the fragment.

As shown in Figure 2.19, the final flight trajectory for a fragment, θ_L, is the sum of the deflection angle, $\theta_{\rm def}$, and the angular impulse imparted to the fragment, $\tan^{-1}(\mathrm{k_x/p})$,

$$\theta_{\rm L} = \theta_{\rm def} - \tan^{-1}(\mathrm{k_x/p}) \tag{2.17}$$

where $\mathrm{k_x}$ is the linear momentum of the removed nucleons and p is the total momentum of the fragment.

As the fragment angle ($\theta_{\rm L}$) increases, the fragment must scatter to ever larger angles to still be accepted into the detector window. Since the deflection angle does not change, the angular impulse imparted to the fragment must increase. This means

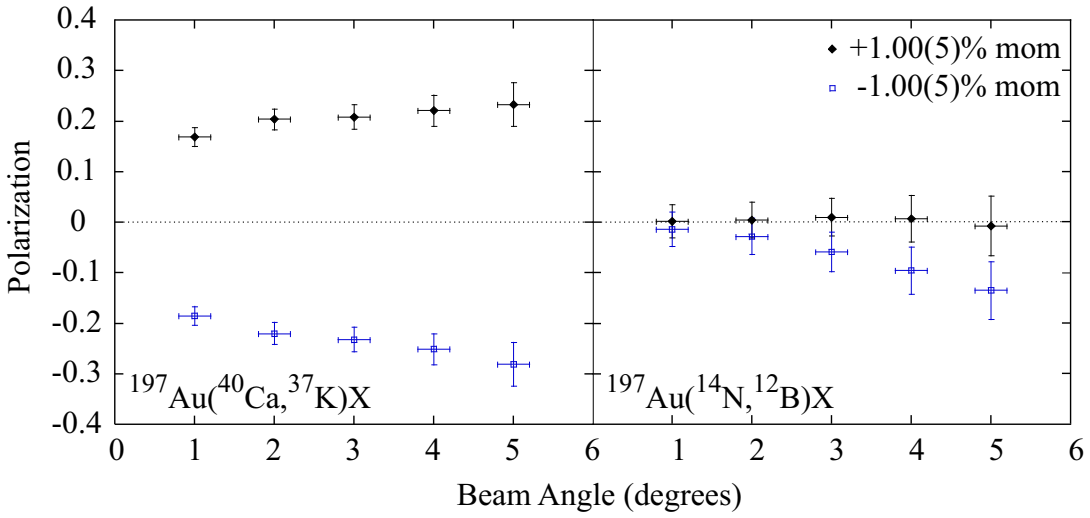

Figure 2.18: Calculated polarization as a function of fragment angle for the fragmentation of 106 MeV/A ^{40}Ca on ^{197}Au to produce ^{37}K (left) and 39.4 MeV/A ^{14}N on ^{197}Au to produce ^{12}B (right). In all cases the fragment angle acceptance was $\pm 0.2°$.

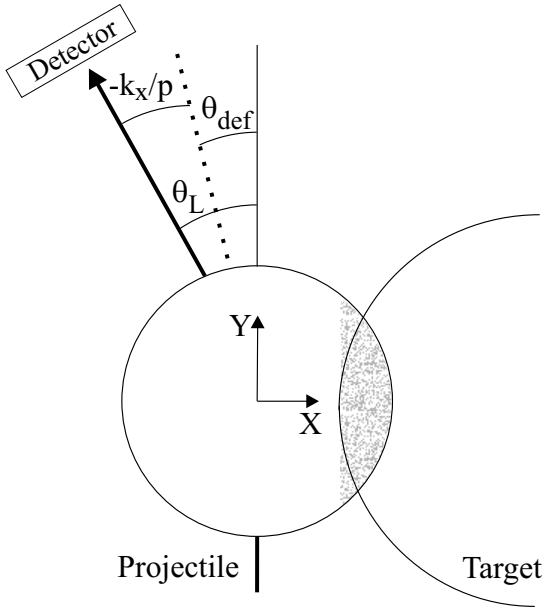

$$\text{Angle} = \theta_{def} - \tan^{-1}(k_x/p)$$

Figure 2.19: Schematic representation of the fragment trajectory.

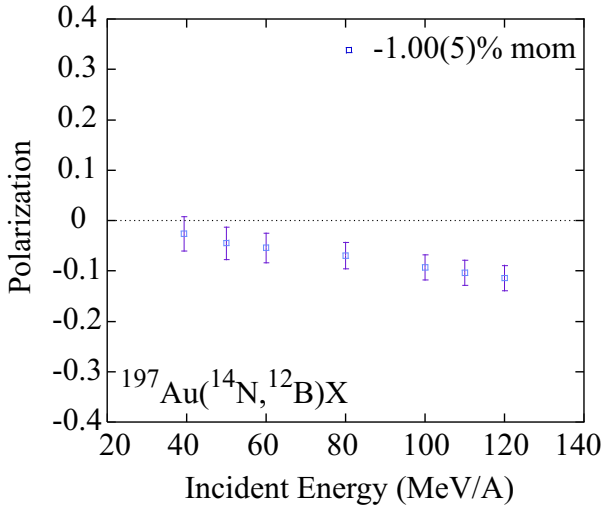

Figure 2.20: Calculated polarization as a function of beam energy for the fragmentation of ^{14}N on ^{197}Au to produce ^{12}B at a fragment angle of 2.0±0.2°.

k_x is increasing as the fragment angle is increasing. Since the polarization is calculated using the linear momentum of the fragment through $\mathbf{L} = -\mathbf{R} \times \mathbf{k}$, larger k_x means larger magnitude polarization, and this is exactly what is both observed and calculated.

2.3.2 Polarization vs. Beam Energy

The variation of the calculated polarization as a function of incident projectile energy in shown in Figure 2.20. The reaction is the fragmentation of ^{14}N in a target of ^{197}Au to make ^{12}B at a fragment angle of 2° at −1.0% momentum. As the incident energy increases, so does the calculated magnitude of the polarization. This can again be understood considering Figure 2.19 using similar arguments as in the polarization vs. fragment angle case above. As the incident energy increases, the deflection angle will decrease (see Appendix A). In order for the fragment to scatter to the same lab angle and be detected, the angular impulse imparted to the fragment must increase to make up the difference. Like before, as the value of k_x increases, so will the magnitude of the polarization.

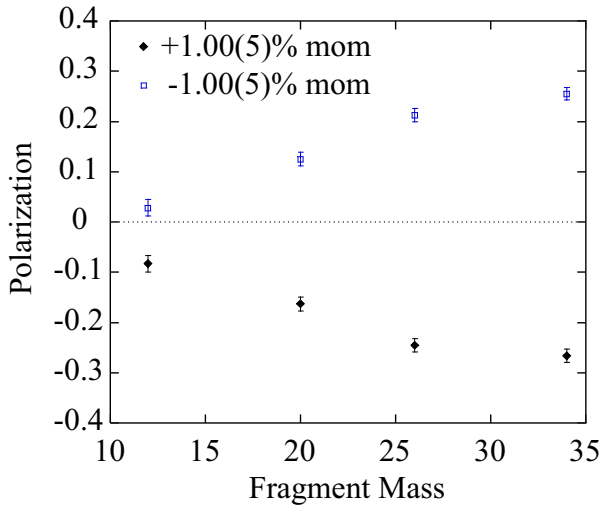

Figure 2.21: Calculated polarization as a function of fragment mass at a fragment angle of 2.0±0.2°. The energy was ≈ 100 MeV/A for each reaction and an ^{27}Al target was used in all cases.

2.3.3 Polarization vs. Fragment Mass

Shown in Figure 2.21 is the calculated polarization as a function of fragment mass. The reactions are the fragmentation of appropriate projectiles on a target of ^{27}Al to remove two nucleons at a fragment angle of 2.0±0.2° at ±1.0% momentum. The primary beam energy was held roughly constant at about 100 MeV/A. The slight variation in energy comes from the necessity for a constant $\bar{\theta}_{\rm def}$ between reactions. The reaction conditions were as rigid as possible in order to isolate any effect the fragment mass has on the polarization. The results of the calculation suggest that as the fragment mass increases, so should the magnitude of the polarization. This can be understood by considering the KMA. The polarization is based on the cross product of the position of the removed nucleons and their momentum. As the fragment mass increases, so does the radius. As the radius increases, so does the position of the removed nucleons. Thus, the polarization increases through the cross product.

2.4 Pickup Reactions

It is apparent from the above work that the magnitude of the polarization is strongly dependent on the amount of linear momentum transferred to the fragment from the removed portion. Indeed, the polarization is defined as the z-component of angular momentum normalized by the total angular momentum,

$$P = \frac{l_z}{|\mathbf{L}|}. \tag{2.18}$$

In the KMA, this angular momentum is calculated by the cross product $\mathbf{L} = -\mathbf{R} \times \mathbf{k}$ where $\mathbf{L}$ is the angular momentum of the fragment, $\mathbf{R}$ is the position of the removed nucleons and $\mathbf{k}$ is the linear momentum of the removed nucleons. Thus, the z-component is

$$l_z = -Xk_y + Yk_x \tag{2.19}$$

where X and Y are the x-(y-)components of the position, and k_x and k_y are the x-(y-)components of linear momentum. Clearly, the spin polarization is dependent on the linear momentum transfered from the removed nucleons to the fragment.

Souliotis *et al.* [23] have shown that in heavy ion fragmentation reactions, charge pickup products (fragments with $Z > Z_{projectile}$) have momentum transfers that deviate significantly from those of the fragmentation products. More specifically, the nucleon picked up by the fragment has a longitudinal momentum equal to the Fermi momentum inside the target nucleus. If the charge pickup reaction is at all similar to fragmentation, a large momentum transfer should correspond to a large degree of spin polarization through Equations 2.18 and 2.19.

Polarization for pickup reactions has not been previously measured and could shed great light on the underlying reaction mechanism. Thus, we have measured the polarization for the pickup product ^{37}K produced from an ^{36}Ar primary beam incident on a ^{9}Be target. This reaction was chosen because it is a single proton pickup process,

and as such, is the simplest reaction to study since evaporation will play no part. Details on the experimental setup and the method for measuring polarization, as well as the results and the interpretation of the results are contained in the following chapters.

Chapter 3

Experimental Setup

As stated in Section 2.4, a measurement of the polarization of a proton pickup product appeared promising, both in the understanding of polarization phenomena and for the future of polarized secondary fragment production. We have measured the polarization for ^{37}K produced from an ^{36}Ar primary beam incident on a ^{9}Be target. This reaction was chosen because it is a single proton pickup process, and as such, is the simplest reaction to study since evaporation will play no part. Furthermore, a primary beam of ^{36}Ar is relatively easy to produce with the Coupled Cyclotrons at the NSCL, and the ^{37}K nucleus has decay properties (e.g. half-life, end point energy, and asymmetry parameter) that facilitate the measurement of the polarization. The technique employed to measure polarization depends on the beta decay of the polarized nucleus. Details on the experimental technique will begin with a brief review of beta decay.

3.1 Technique

3.1.1 Beta Decay Angular Distribution

Beta decay is the process where a proton(neutron) within the nucleus transforms into a neutron(proton). As a result of this change, a neutrino(anti-neutrino) and a positron(electron) are emitted. Beta decay can be characterized into three types:

(1). β^- decay: ${}^{A}_{Z}\mathrm{X}_{N} \rightarrow {}^{A}_{Z+1}\mathrm{X}'^{+}_{N-1} + \mathrm{e}^- + \bar{\nu}$

(2). β^+ decay: ${}^{A}_{Z}\mathrm{X}_{N} \rightarrow {}^{A}_{Z-1}\mathrm{X}'^{-}_{N+1} + \mathrm{e}^+ + \nu$

(3). electron capture: ${}^{A}_{Z}\mathrm{X}_{N} \rightarrow {}^{A}_{Z-1}\mathrm{X}'_{N+1} + \nu$

β^- decay is the transformation of a neutron into a proton with the concomitant emission of an electron and an anti-neutrino. β^+ decay is the transformation of a proton into a neutron, accompanied by the emission of a positron (anti-electron) and a neutrino. In electron capture, the analog of β^+ decay, an atomic electron is captured by the nucleus during the transformation of a proton into a neutron, and a neutrino is released. Since the captured electron leaves a vacancy in the atomic shell structure, x-rays are generally emitted as higher-energy electrons relax down into the vacant shell below.

Beta decay is governed by the parity-violating weak force, and it can be anisotropic under certain conditions. The emitted electrons in all cases obey the general angular distribution equation:

$$W(\theta) = 1 + \sum B_\lambda A_\lambda U_\lambda Q_\lambda P_\lambda(\cos\theta) \tag{3.1}$$

where θ is the angle of emittance relative to the orientation axis, B_λ are the orientation parameters of the parent nucleus, A_λ are the angular distribution coefficients, U_λ are the de-orientation parameters, Q_λ are the solid angle correction factors and P_λ are the Legendre polynomials of order λ [32]. The orientation parameters (B_λ)

take into account the orientation (i.e. polarization) of the nuclei; $B_\lambda = 0$ for an unoriented sample. The angular distribution coefficients (A_λ) account for the degree of anisotropy in the beta decay for a particular isotope. They are a fundamental property of the nuclear transition for the isotope under study, and they depend on the angular momentum of the initial and final states. The de-orientation parameters (U_λ) account for any loss of orientation from unobserved decay prior to the observed (or studied) decay. The solid angle correction factors (Q_λ) are for sources and detectors that are not geometrical points.

For beta decay of polarized nuclei, all of the even λ terms vanish; furthermore, all of the terms above $\lambda = 1$ are ignored because their contributions are small. With no unobserved decays to de-orient the sample and neglecting solid angle correction factors ($U_1 = 1$ and $Q_1 = 1$), the angular distribution equation becomes

$$W(\theta) = 1 + PA_\beta \cos\theta \tag{3.2}$$

where $A_\beta = A_1$, $\cos\theta$ is the first order Legendre polynomial, and the polarization P is given by

$$P = \frac{B_1}{\sqrt{3}\rho_1^{max}(I)} \tag{3.3}$$

where ρ_1^{max} is the value of the statistical tensor for maximum spin polarization (see Equation 1.2).

The technique for measuring polarization takes advantage of this angular anisotropy of the emitted beta particles. If the nucleus of interest has some spin polarization, the betas will have an angular distribution governed by Equation 3.2, provided the transition has a nonzero asymmetry parameter. If the nuclei of interest have zero polarization, the distribution will be isotropic regardless. The angular distribution, then, can be used as a probe for detecting polarized nuclei. A description of the technique follows.

3.1.2 Pulsed-Field Polarization Method

Polarization was measured following the technique developed by Anthony and co-workers [33]. Although there are many ways to measure polarization, the key to the technique of Anthony *et al.* is that it does not require prior knowledge of the magnetic moment. Furthermore, it is suitable for short-lived nuclei with long spin lattice relaxation times (T_1) relative to the decay half-life ($T_{1/2}$) which is ideal for isotopes produced by fragmentation reactions. The combination of short $T_{1/2}$ and long T_1 insures the nuclei β-decay before significant polarization loss occurs through spin lattice relaxation.

In an external magnetic field, a nucleus that is oriented ($B_1 \neq 0$) with some nonzero asymmetry parameter A_β will show different counting rates in a detector placed at $\theta = 0^\circ$ and one placed at $\theta = 180^\circ$ relative to the direction of the external field. This difference is rooted in the fact that the angular distribution equation (Eq. 3.2) has a maximum when $\theta = 0^\circ$ and a minimum for $\theta = 180^\circ$. The method of Anthony *et al.* involves measuring the magnetic field double-ratio

$$R = \frac{(\text{up/down})_{\text{field on}}}{(\text{up/down})_{\text{field off}}} \tag{3.4}$$

where the externally applied magnetic field is pulsed on and off, and 'up' and 'down' represent the number of beta particles counted in detectors placed at 0° and 180° respectively. When the field is on, the β-decay will be directionally anisotropic if the nuclei have some spin polarization. When the field is off, the β-decay will be directionally isotropic. The de-polarization of the spin system when the field is off is due to quadrupolar interactions that may dominate at the location of the impurity in a face centered cubic host material [34]. Nuclei implanted without polarization will give a ratio of unity, while nuclei implanted with spin polarization will give a ratio different from unity. Any deviation from unity, then, will be proportional to the

magnitude of the spin polarization:

$$R = \frac{(up/down)_{field\ on}}{(up/down)_{field\ off}} = \frac{(W(0°)/W(180°))_{field\ on}}{(W(0°)/W(180°))_{field\ off}} = \frac{1 + A_\beta P}{1 - A_\beta P} \tag{3.5}$$

where A_β is the asymmetry parameter and P is the polarization. Typical values for the polarization are a few percent, and with asymmetry parameters with typical values of roughly 0.5, the ratio R takes values near 0.9. The double ratio is used to eliminate any systematic asymmetries inherent to the apparatus.

The major error for these measurements is statistical and therefore goes like the square root of the number of counts. The statistical error on R is given by the expression

$$\sigma_R = R\sqrt{\left(\frac{\sqrt{N}}{N}\right)^2_{up,on} + \left(\frac{\sqrt{N}}{N}\right)^2_{up,off} + \left(\frac{\sqrt{N}}{N}\right)^2_{down,on} + \left(\frac{\sqrt{N}}{N}\right)^2_{down,off}} \tag{3.6}$$

where N is the number of counts. If each detector is counted to a similar level, the above equation simplifies to

$$\sigma_R = R\sqrt{\left(\frac{4}{N}\right)}. \tag{3.7}$$

Generally, enough counts are collected to achieve 3σ statistics. That is, a ratio must have enough counts to be at least three 'error bars' away from one (or from the normalizing ratio). As an example, if the polarization is 1% and $A_\beta = 0.5$, then R = 0.990 (by Equation 3.5) and σ needs to be 0.003. This requires approximately 440,000 counts in each detector (calculated using Equation 3.7).

3.2 Radioactive Beams

Radioactive ions studied at the National Superconducting Cyclotron Laboratory (NSCL) are produced using the technique of projectile fragmentation. At the cou-

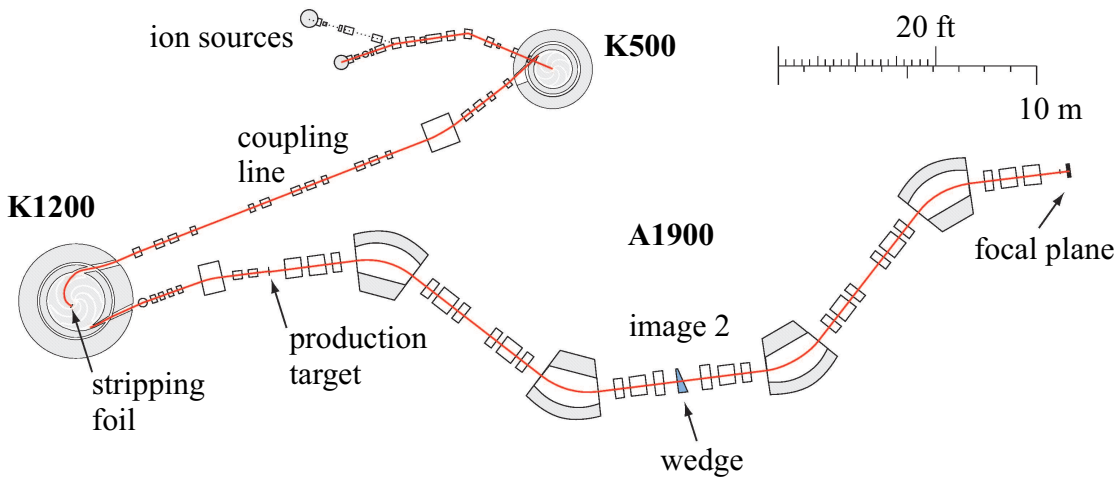

Figure 3.1: Schematic representation of the ion source, the K500 and K1200 cyclotrons and the A1900 fragment separator at the NSCL Coupled Cyclotron Facility.

pled cyclotron facility, stable isotopes are excited into a vapor state and partially ionized in the ion source. They are first accelerated in the K500 cyclotron, injected into the K1200 cyclotron, fully stripped and finally accelerated up to 200 MeV/A and directed onto a thick production target (see Figure 3.1). The projectiles are abraded in the target producing a host of stable and radioactive nuclei ranging in charge and mass from the primary beam to helium. These fragments proceed into the A1900 fragment separator [35, 36] where they are separated based on rigidity (momentum to charge ratio) in the first half of the spectrometer and nuclear charge using a thick wedge material at the intermediate image. The second half of the spectrometer is used to focus the fragments with different momenta back into a single spot at the focal plane - this makes the A1900 an achromatic spectrometer.

For the present work, two beams of secondary fragments were studied. ^{32}Cl was produced from a primary beam of 150 MeV/A ^{36}Ar on a 765 mg/cm^2 ^{93}Nb target. A polarized ^{32}Cl beam was produced in an earlier experiment at the NSCL [37] to determine the magnetic moment of this nucleus. ^{32}Cl was produced for the present work under similar conditions to test the experimental apparatus. The primary beam was directed onto the target at a beam angle of $+2^{\circ}$ (positive angles for this experiment

are defined to the right of the beam axis facing downstream), and an aperture was placed in the beam path 12.7 cm downstream from the target to limit the angular acceptance to $\pm 0.5^\circ$ into the A1900. This reproduced the experimental conditions that were used with the A1200 fragment separator in the previous experiment. The new A1900 has a larger momentum acceptance ($\pm 2.5\%$) and a larger angular acceptance ($\pm 2.5^\circ$) than the A1200, thus the aperture plate was employed. A diagram of the 1.285 cm thick heavy metal (97% tungsten) aperture plate is shown in Figure 3.2. Each hole has a diameter of 2.08 mm, which corresponds to $\pm 0.5^\circ$ angular acceptance for the plate positioned 12.7 cm downstream form the target, and the vertical alignment was such that the central hole labeled C in the figure corresponds to the beam axis. Holes B and D correspond to -1° and $+1^\circ$ fragment angles and holes A and E correspond to -2° and $+2^\circ$ fragment angles. The fragments could only pass through one hole to reach the focal plane of the A1900. This arrangement allows for beam angles larger than the magnets in the beam line can actually produce. For example, the beam steered to a beam angle of $+2^\circ$ in combination with hole D in the aperture plate results in a total angle of $+3^\circ$. Only the central hole (C) was used for this work. The ^{32}Cl fragments were selected in the A1900 with $B\rho_1 = 3.1040$ Tm and $B\rho_2 = 2.0058$ Tm using a 971 mg/cm^2 acrylic wedge at the image 2 position with a momentum acceptance of $\pm 0.5\%$.

^{37}K ions were produced from the same primary beam of 150 MeV/A ^{36}Ar with a 578 mg/cm^2 ^{9}Be target. The primary beam was steered to a beam angle of $+2^\circ$, and the beam pipe of the A1900 provided a physical beam angle acceptance of $\pm 2.5^\circ$ (i.e. no aperture was used). The ^{37}K fragments were separated using the same 971 mg/cm^2 acrylic wedge. Various momentum values with an acceptance of $\pm 0.5\%$ were selected and the $B\rho$ values for these settings are summarized in Table 3.1. These momentum values were selected by first centering the production peak at the A1900 intermediate image, and then moving off the central momentum by 0.5%, -0.5% and 1.0%.

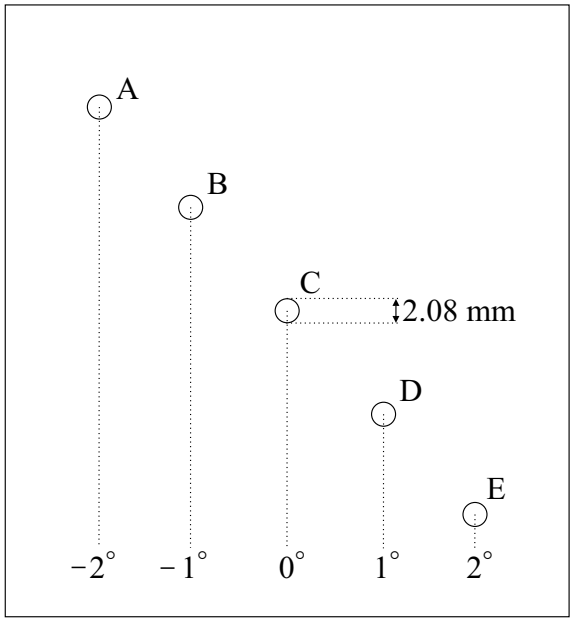

Figure 3.2: Diagram of the aperture plate used to select the beam angle acceptance for the ^{32}Cl measurement.

In both cases, the fragments were sent to the polarization measuring apparatus in the S1 experimental vault with approximately 95% transmission.

As a final check that the ^{32}Cl and ^{37}K nuclei were properly identified in the A1900, the beam was pulsed on and off and a half-life was measured for the nuclei that were implanted in the catcher foil in the S1 vault.

3.3 Beta-NMR Apparatus

The fragments to be studied passed through a 500 μm Si PIN and a capton window, traveled 20 cm in air and came to rest in a catcher foil in the center of the gap

Table 3.1: A1900 Bρ values for the various momentum settings for ^{37}K.

Momentum (%)	Bρ_1 (Tm)	Bρ_2 (Tm)
-0.5	3.14208	1.6345
0.0	3.15787	1.7004
0.5	3.17366	1.7636
1.0	3.18945	1.8260

between the poles of a room temperature dipole magnet (see Figure 3.3). This magnet has a pole gap of 10.7 cm and provided the external field that maintained the initial polarization of the implanted secondary fragments. The magnet was energized to 40 amps ($\approx$ 1000G) for ^{32}Cl and at 120 amps ($\approx$ 3000G) for the ^{37}K measurement, respectively. The detector system for this setup consisted of two β telescopes located at 0° and 180° relative to the field direction of the dipole magnet. The telescopes were each composed of one 4.4 cm x 4.4 cm x 3 mm thick ΔE plastic scintillator and one 5.1 cm x 5.1 cm x 20 mm total energy plastic scintillator. Each scintillator was coupled to an acrylic light guide with a 45° angle to place the photomultiplier tubes out of the dipole magnet fringe field (see Figure 3.4). The telescopes were placed 2.4 cm above and below the catcher foil and in total, covered approximately 27% of the 4π solid angle ($\approx$14% for each detector telescope). The detectors are numbered one through four starting at the top, and any references to the detectors are done so using this numbering system: B1 (thick detector on top), B2 (thin detector on top), B3 (thin detector on bottom) and B4 (thick detector on bottom) (refer to Figure 3.4). Additional details regarding the β-NMR apparatus can be found elsewhere [15].

For the ^{32}Cl measurement, beta attenuators were placed between the thin and thick detectors to absorb the low energy betas that come from a predicted ^{31}S contaminant in the ^{32}Cl beam. These attenuators were one 1.2 mm thick by 2-inch square piece of stainless steel and one 1.0 mm thick by 2-inch square piece of Al on both the top between B1 and B2 and again on the bottom between B3 and B4. Together, these attenuators absorb betas with energies up to $\approx$1.9 MeV. These attenuators were not used in the ^{37}K measurement, because there were few expected beam contaminants and the Q-value for ^{37}K is low.

The implantation host where the radioactive nuclei produced from the fragment separator come to rest was a 25 mm diameter, 2.5 mm thick cubic-lattice NaCl crystal for the ^{32}Cl measurement [37] and a 22 mm diameter, 4 mm thick cubic-lattice KBr

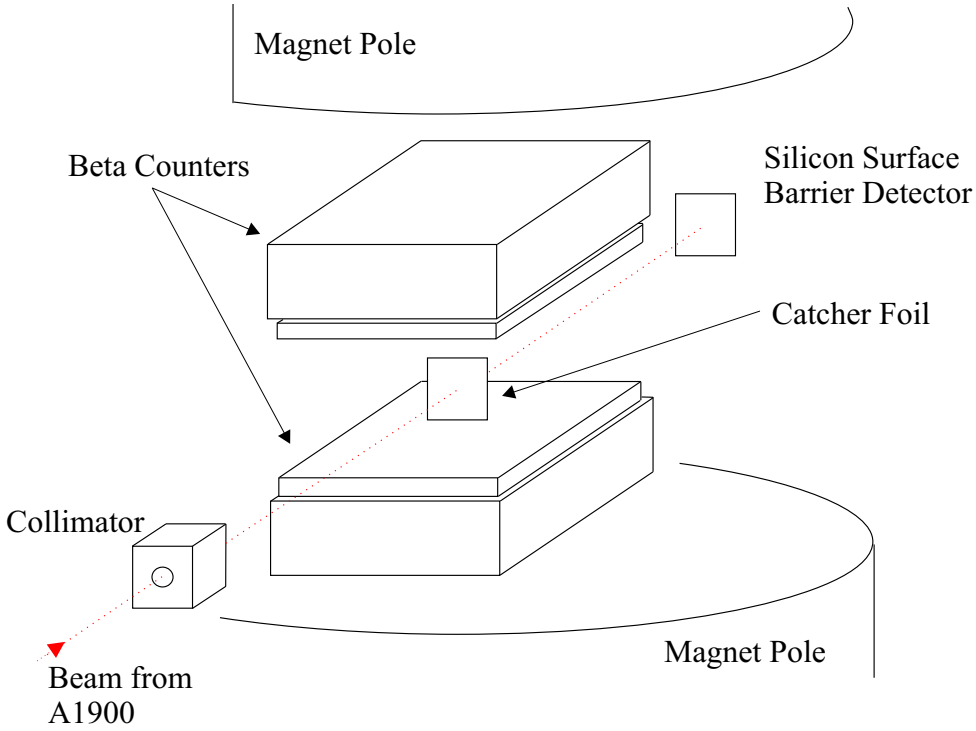

Figure 3.3: Schematic representation of the experimental setup for measuring polarization.

crystal for the ^{37}K measurement. The catcher foil material was chosen for each specific nucleus to ensure that interactions of the implanted nuclei with the host material are small, resulting in long spin lattice relaxation times. It has been shown that a large percentage of the original spin polarization is preserved upon implantation into a crystal host containing the same type of positive ions [38]. Loss of polarization due to relaxation effects for ^{37}K in KBr should not be a factor due to the short half-life (1.23 sec [39]) and the typically long relaxation time (several seconds at T=273 K) for ^{37}K in KBr [30]. The catcher foil was mounted between the detector telescopes and tilted at an angle of 45° with respect to the holding field of the dipole magnet. The goal was to minimize the amount of material the emitted β particles must traverse before reaching the detectors. A 0.9 cm thick Al collimator placed 4 cm upstream from the catcher foil was used to limit the beam spot to a diameter that only illuminates the catcher foil. A silicon surface barrier detector was placed 26 cm downstream from the

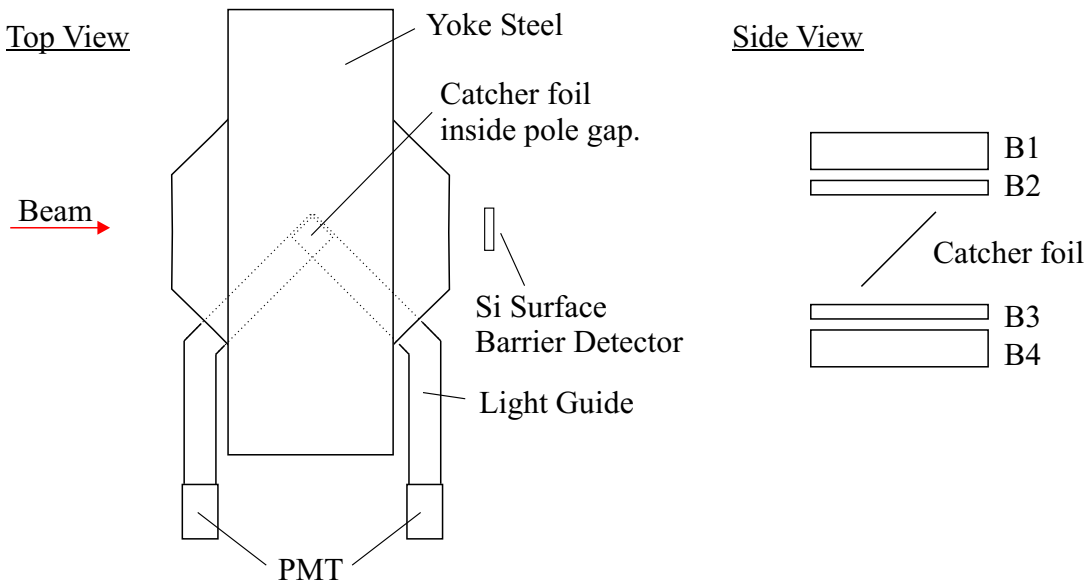

Figure 3.4: Top and side views of the experimental apparatus.

catcher foil and used as a veto detector.

Offline measurements with radioactive sources demonstrated that the apparatus has some inherent asymmetry. Shown in Figure 3.5 are beta spectra from detector B1 for a ^{60}Co source placed at the catcher foil position for two magnetic field settings (40 amps and 120 amps). A field dependent asymmetry is evident. Various shielding configurations around the PMT's using both mu-metal and soft iron altered but did not eliminate the problem. A final shielding configuration utilizing 1 cylindrical mu-metal shield of 0.66 mm thickness was placed around each photo tube with $\approx$1 cm hanging over the front of each tube. In light of this asymmetry, all measurements were accompanied by a corresponding measurement at a beam angle of 0°. A 0° measurement will produce nuclei that have zero polarization, and thus serve as a normalization for any polarization measurement.

3.3.1 Electronics

Shown in Figures 3.6 and 3.7 are schematic diagrams for the detector electronics used during this experiment. ADC and TDC readout was through VME, coincidences and

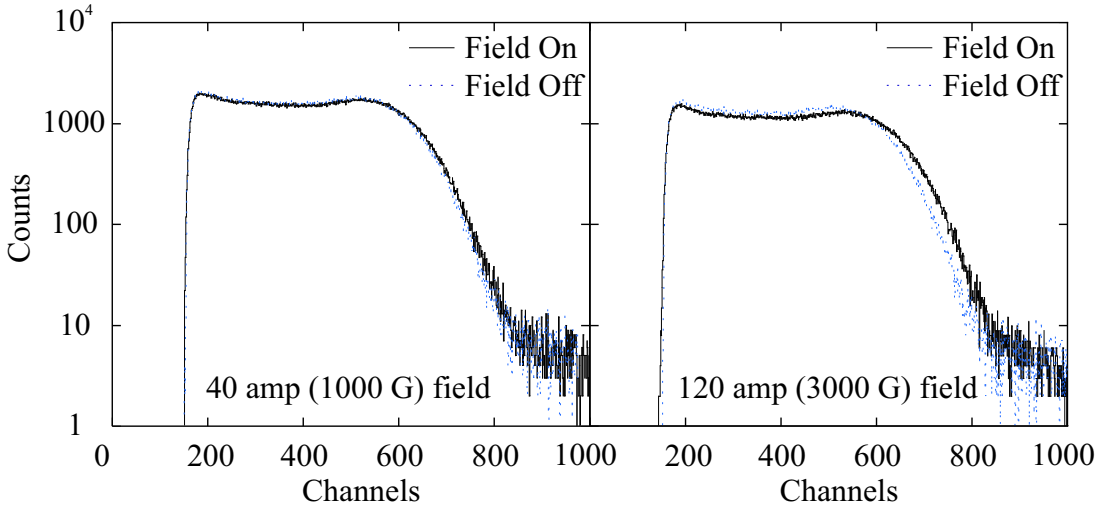

Figure 3.5: Detector B1 decay spectra of a ^{60}Co source placed at the catcher foil position. Two magnetic field settings were used.

scalers were read out using CAMAC, and all other electronics used NIM. Beam pulsing for the half-life measurements was accomplished by shifting the phase in the C-Dee in the K500 cyclotron by providing a TTL signal from a programmable dual gate generator to the input of the cyclotron RF control system. This pulsing in the RF triggered the reset in a real-time clock which was read out on each beta event, thus giving a beta decay spectrum. The master gate was triggered either by the PIN or by the any one of the beta counters as indicated by the OR-gate in Figure 3.7. The master gate trigger by the PIN was downscaled by a factor of 100 to prevent these triggers from dominating the master gate. Furthermore, when the beam rate was greater than ≈7000, the PIN was removed from the beam path all together, and the beta counters were the only master trigger. Magnet pulsing was accomplished through a NIM signal from a pulser module in combination with a dual gate generator set to switch on and off every 60 seconds.

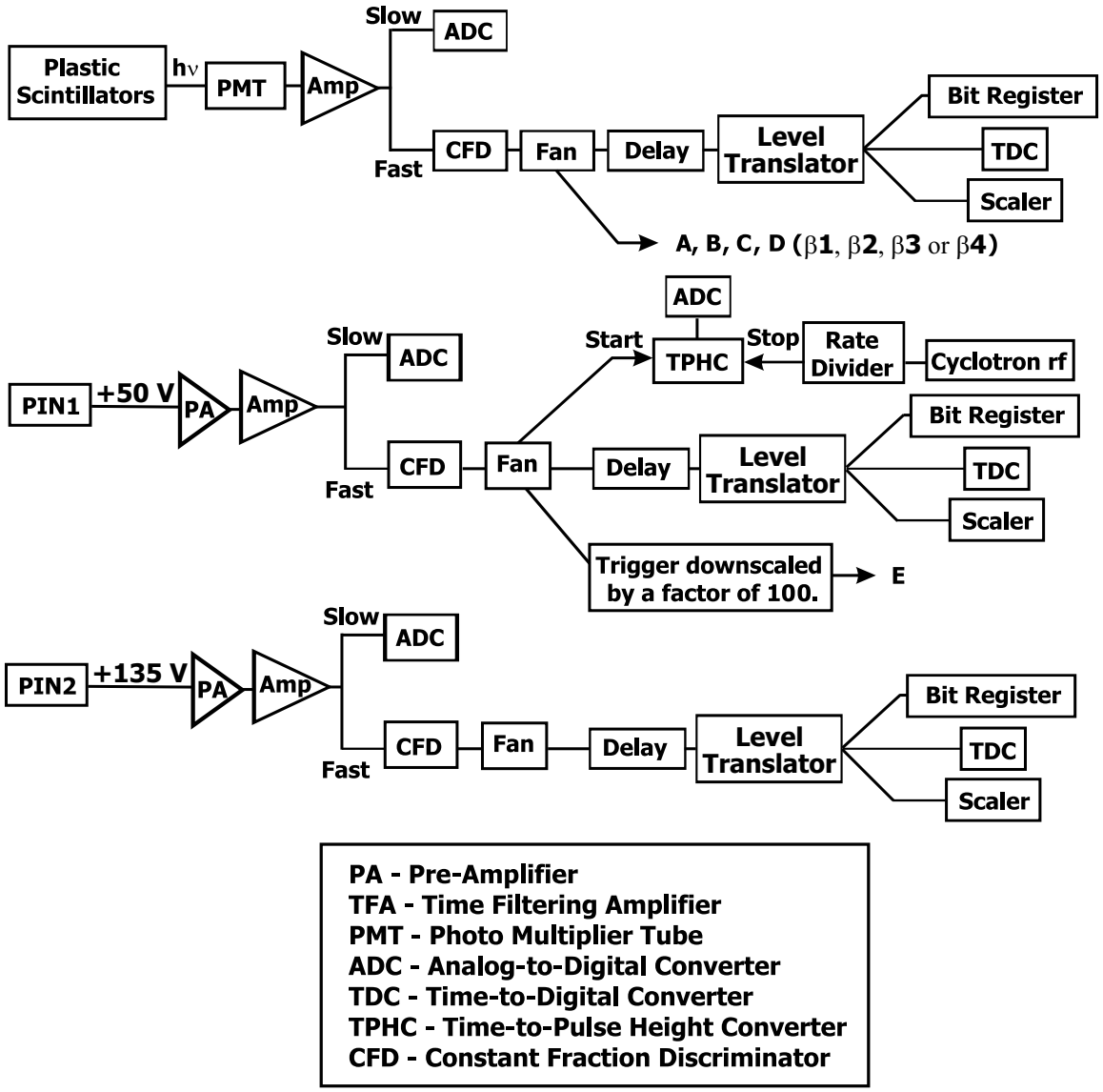

Figure 3.6: Plastic scintillator, PIN1, and Si surface barrier detector (PIN2) electronics diagram.

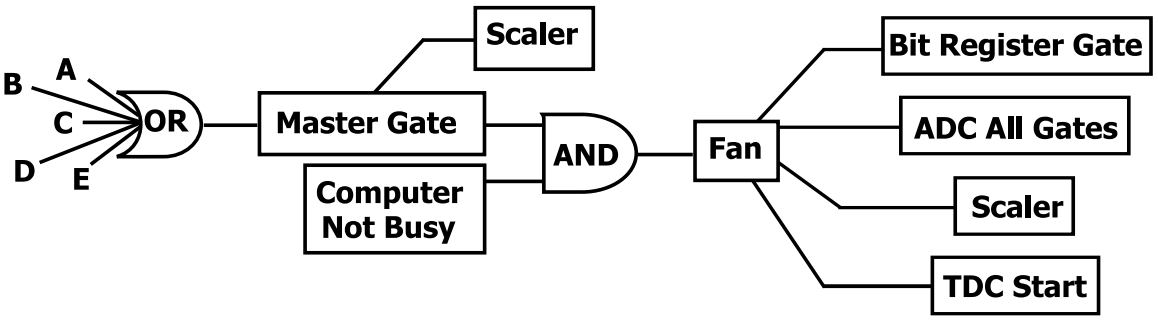

Figure 3.7: Master gate electronics diagram. A, B, C, D, and E come from Figure 3.6.

Chapter 4

Experimental Results & Interpretation

4.1 ^{32}Cl

4.1.1 Particle Identification

Since the polarization measurement is based on the detection of β particles, the purity of the beam is important. The detected beta particles come from activities implanted in the catcher crystal without any knowledge or correlation to the parent from which they come. Thus, impurities in the beam will give betas from different nuclei which may interfere with the results. As described in the experimental section, the ^{32}Cl fragments were separated from the other reaction products using the A1900 fragment analyzer before being sent to the experimental end station. The ΔE-TOF particle identification plot for ^{32}Cl ions is shown in Figure 4.1. Here ΔE is measured in PIN 1 and TOF (time-of-flight) is measured as the time difference between a signal in PIN1 and the rf frequency of the K1200 cyclotron. The PID shown in Figure 4.1B is for a beam angle of 0° with no aperture, and the spectrum has almost no contaminants. The PID shown in Figure 4.1A is for a beam angle of 0° with the aperture in place

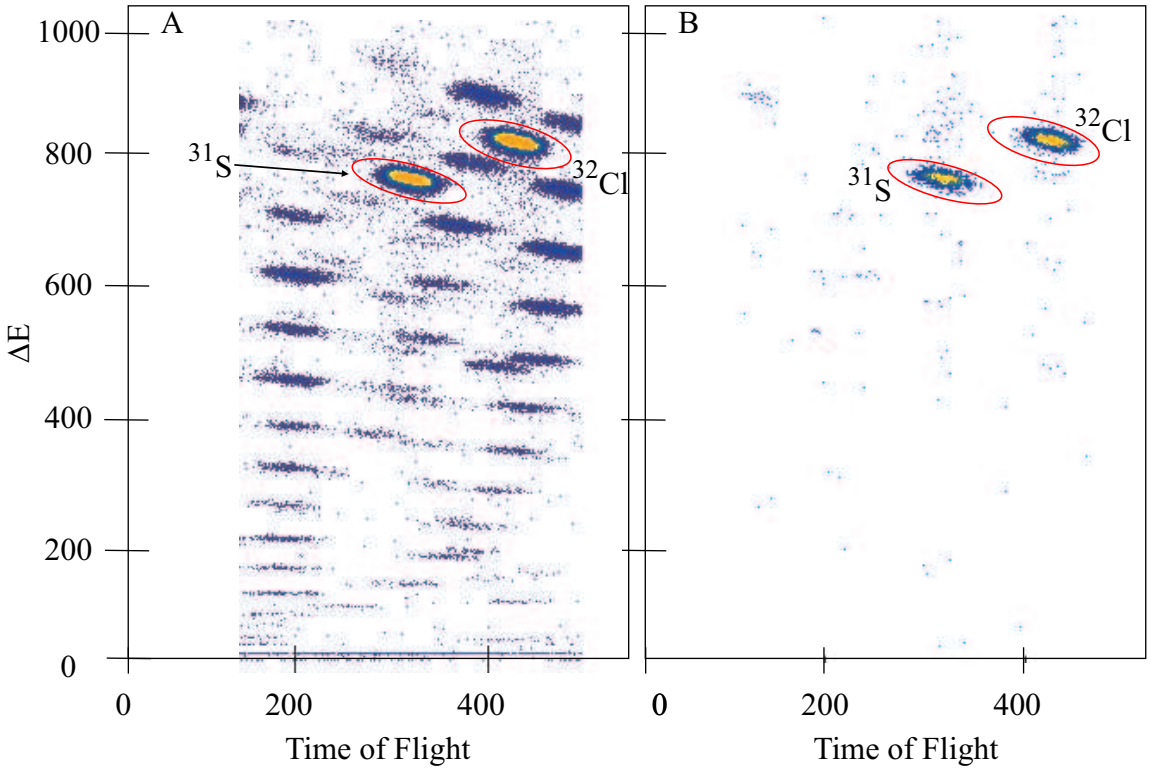

Figure 4.1: Delta E-TOF plot for ^{32}Cl produced at a 0° beam angle with the aperture (A), and without the aperture (B).

in position C. Each individual contour represents a different nucleus. Clearly, ^{31}S and ^{32}Cl make up most of the beam, but there are other contaminants present. Using the same thick acrylic wedge described in the experimental setup, LISE [40] predicts ^{31}S to be the only contaminant in the ^{32}Cl beam, as observed with no aperture in place. Other contaminants probably come from primary beam interacting on the edges of the aperture holes, losing energy and traveling through the A1900 to the image two position. At the image two position, this primary beam subsequently causes nuclear reactions in the wedge degrader. Since these fragments are produced by the wedge, there is no further separation in the A1900 (except maybe a slight rigidity cut in the second half of the A1900) and they travel to the experimental end station as contaminants. Thus, all 0° runs were performed without the aperture (giving them an angular acceptance of ±2.5°). This is acceptable since the 0 degree data will have no polarization, and therefore no 'signal' to reduce by opening up the angular

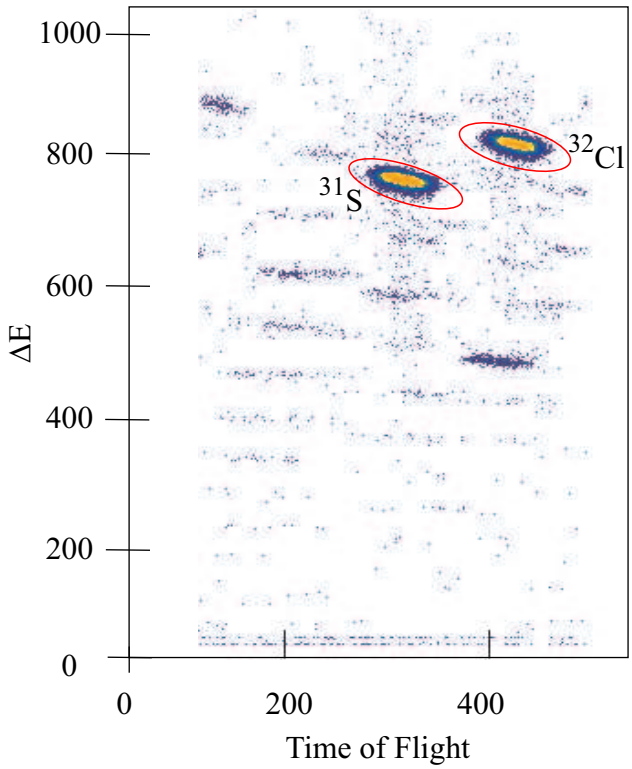

Figure 4.2: Delta E-TOF plot for ^{32}Cl produced at a 2° beam angle with the aperture in place.

acceptance. The removal of the aperture at 0° increases the count rate.

The data collected at a 2° beam angle require the aperture to limit the angular acceptance since polarization may be evident. Recall that using the aperture was necessary to limit the angular acceptance in order to reproduce the experimental conditions of the earlier measurement. Shown in Figure 4.2 is a ΔE-TOF plot at a 2° beam angle with the aperture limiting the acceptance to ±0.5°. This spectrum is relatively clean with 40% ^{32}Cl and 57% ^{31}S, even with the aperture in place. In this case, the 2° beam angle causes the primary beam to fall outside the ±0.5° beam acceptance, thus reducing the nuclear reactions in the wedge that were present at the 0° beam angle and providing a ^{32}Cl beam with only a ^{31}S contaminant.

Shown in Figure 4.3 are ^{32}Cl beta spectra for the two thick detectors (B1 and B4) and for the two thick detectors in coincidence with the thin detectors (B2 and B3). The beta spectra from only the thick detectors have low energy features not present

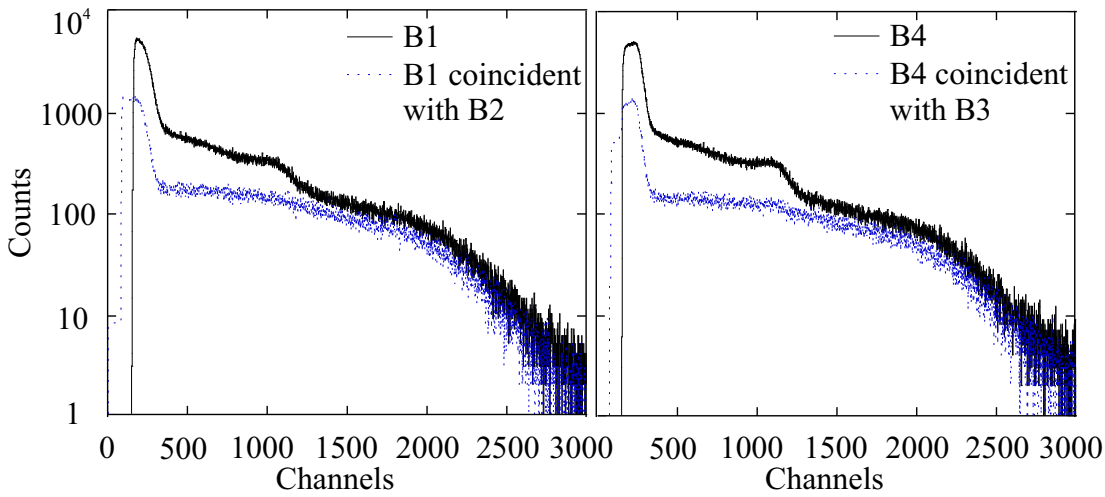

Figure 4.3: ^{32}Cl beta decay spectra for the two thick detectors (B1 left and B4 right) as the solid black line and the thick detectors in coincidence with the thin detectors (B1 with B2 left and B4 with B3 right) as the dashed blue line. The fragments were produced at a 2° beam angle.

in the coincident spectra. The requirement that the detected particle traverse both detectors (the coincidence) implies whatever particles make the low energy features in the thick detectors are not betas, because betas will interact with the plastic scintillators in either the thick or thin detectors with almost 100% certainty. Gamma rays, however, will have a very low probability of interacting with the thin detectors, but are more likely to interact with the thick detectors. Gamma rays will be present because ^{32}Cl decays to excited states in the ^{32}S daughter almost 100% of the time, see Figure 4.4. (^{31}S decays almost exclusively to the ground state in ^{31}P, thus there are no associated gamma rays). The coincident requirement effectively removes these gammas from the decay spectrum.

Shown in Figure 4.5 are the coincident beta spectra for both magnetic field on (solid black line) and off (dashed blue line). There does not appear to be a large magnetic field dependent asymmetry in the beta spectra. This is in agreement with the offline source data (see Figure 3.5), where the magnet power supply was set to 40 amps (field $\approx$ 1000 G).

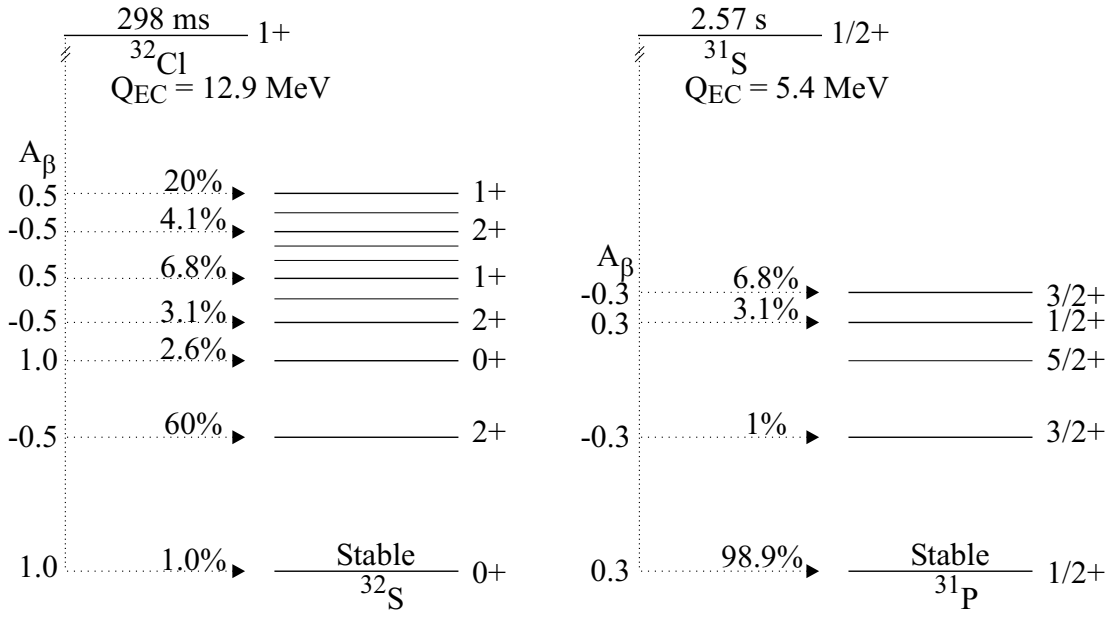

Figure 4.4: Decay schemes for ^{32}Cl and ^{31}S [39]. Asymmetry parameters (A_β) from [41] assuming pure GT transitions are listed in the figure.

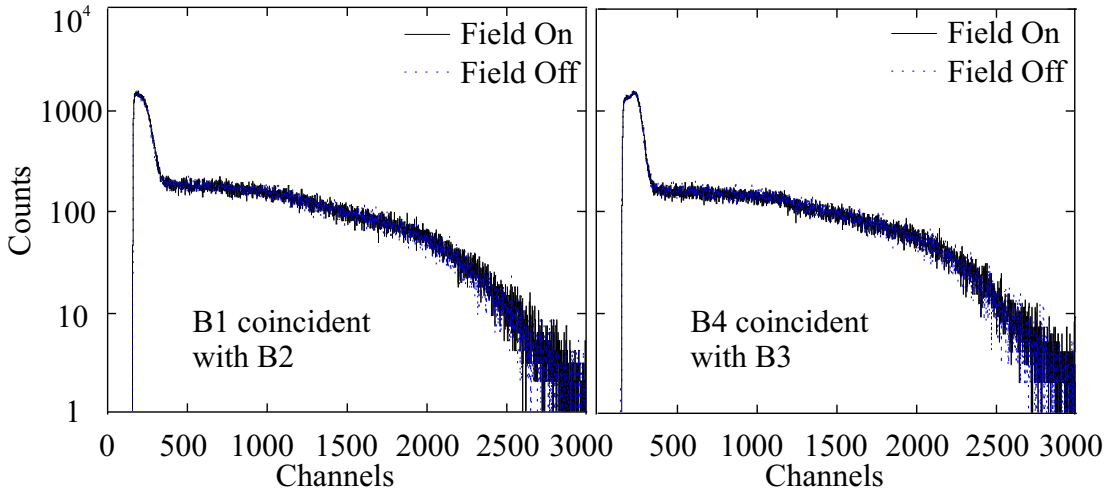

Figure 4.5: ^{32}Cl beta decay spectra for the thick detectors in coincidence with the thin detectors (B1 with B2 left and B4 with B3 right) with the field on spectra as the solid black line and the field off spectra as dashed blue line. The fragments were produced at a 2° beam angle.

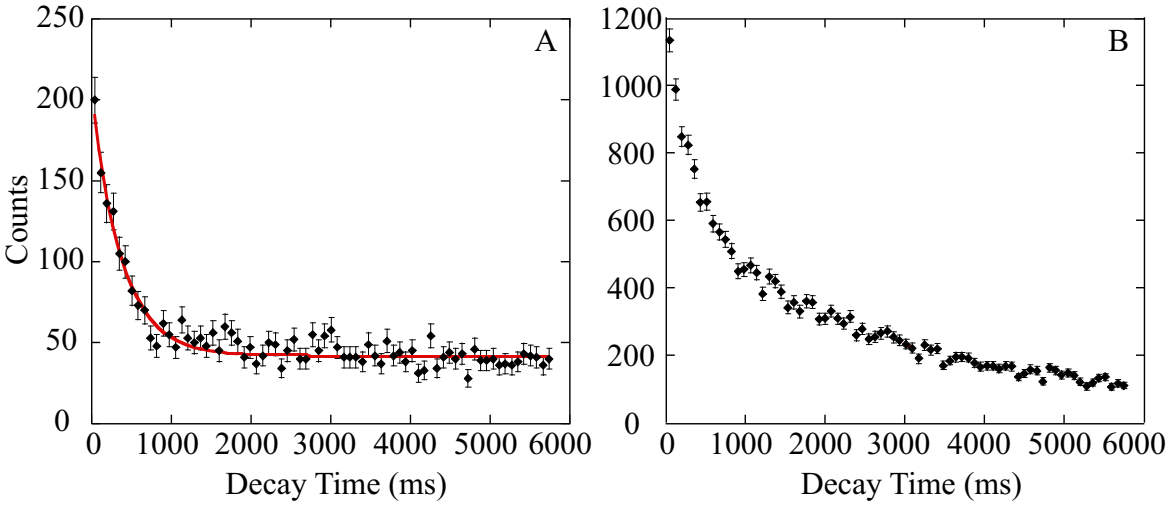

Figure 4.6: ^{32}Cl decay curve for B1 coincident with B2 (Panel A) and for B2 alone (Panel B). The red line in Panel A is a single exponential fit.

4.1.2 Decay Curve

Prior to the polarization measurement, a half-life was measured to verify the identity of the implanted fragments. Shown in Figure 4.6A is the measured decay curve for the implanted fragments with a gate on betas coincident in detectors B1 and B2 (thick and thin), and the decay for betas in detector B2 alone is shown in Figure 4.6B. The coincident spectrum should contain only ^{32}Cl betas, whereas the spectrum from detector B2 alone will contain both the low energy ^{31}S betas and the ^{32}Cl betas. Recall that beta attenuators were installed between the thick and thin detectors to remove the low energy betas from ^{31}S, which has a Q-value of 5.4 MeV [39]. The reduction in background is readily apparent in the decay curve for coincident B1 and B2 detectors. A single exponential fit to the coincident decay curve (red line in Panel A) reveals a half-life of 259$\pm$20 ms which agrees with the accepted half-life of 298$\pm$1 ms [42] for ^{32}Cl. These spectra show that ^{31}S is indeed present in the thin detectors, but the attenuators effectively eliminate the low-energy beta particles.

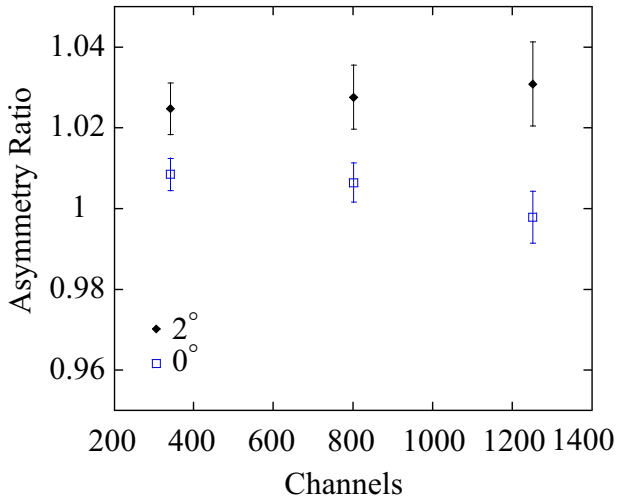

Figure 4.7: ^{32}Cl asymmetry ratios as a function of the energy threshold in the thick detectors.

4.1.3 Polarization

Based on the characteristics of the β-spectra (Figure 4.3), the ratios calculated to determine polarization were based on coincidences between thin and thick detectors within a given telescope. The coincident requirement eliminates the low-energy betas from ^{31}S and any delayed γ-rays. Shown in Figure 4.7 are the measured asymmetry ratios for both the 0° and the 2° measurements as a function of threshold in the thick detectors. As the energy threshold increases, more low-energy betas are excluded from the ratio. This is desirable, because with a Q-value of 12.7 MeV [39], the highest energy betas should come from ^{32}Cl. A measured asymmetry of 3.5±0.9% for the 2° data relative to the 0° is evident in the figure. The asymmetry measured in the previous experiment by Rogers *et al.* [37] was 3.1±0.5%, in good agreement with the present work.

The work of Anthony *et al.* [33] to develop the pulsed magnetic field technique deduced a polarization result only 60% of that obtained by the traditional NMR technique. However, the agreement between the asymmetry of this measurement and that of Rogers *et al.* [37] indicates the pulsed field technique is capable of measuring the full polarization of implanted nuclei. The main difference between the present

measurement and the work of Anthony *et al.* is that a Pt catcher foil was used for their measurement of ^{12}B polarization while a NaCl foil was used for our measurement of ^{32}Cl. Perhaps the difference between the host material and the implanted nuclei resulted in polarization loss upon implantation. Recall Ref. [34] in which it was shown that polarization is preserved for nuclei implanted into a crystal host containing the same type of positive ions. Alternatively, unknown quadrupolar interactions in the host crystal could have maintained the polarization when the field was pulsed off. This would raise the 'background' asymmetry and reduce the magnitude of any measured polarization.

Overall, the agreement between the current measured asymmetry and the previous asymmetry for ^{32}Cl is evidence that both the A1900 and the β-NMR apparatus function properly and can be used to readily detect polarization of ^{37}K fragments produced by proton pickup.

4.2 ^{37}K

4.2.1 Particle Identification

Shown in Figure 4.8 is a ΔE-TOF plot at a beam angle of 0° at central momentum (0%) with a momentum acceptance of $\pm$0.5% with no aperture. The spectrum shows a relatively pure beam of ^{37}K with ^{36}Ar and ^{35}Ar as contaminants. The ^{36}Ar does not pose a problem because it is β-stable. The ^{35}Ar is problematic as its half-life (1.78 s) and Q-value (6.0 MeV) are similar to ^{37}K (Figure 4.9). Fortunately, this contaminant is a low enough percentage of the total beam that any contribution will be minimal (see Table 4.1).

The goal was to study the momentum dependence of the ^{37}K polarization at several different fragment momentum values, p. Data were collected at -0.5%, 0%, 0.5% and 1% from the central momentum, where p_0 is now defined as the peak

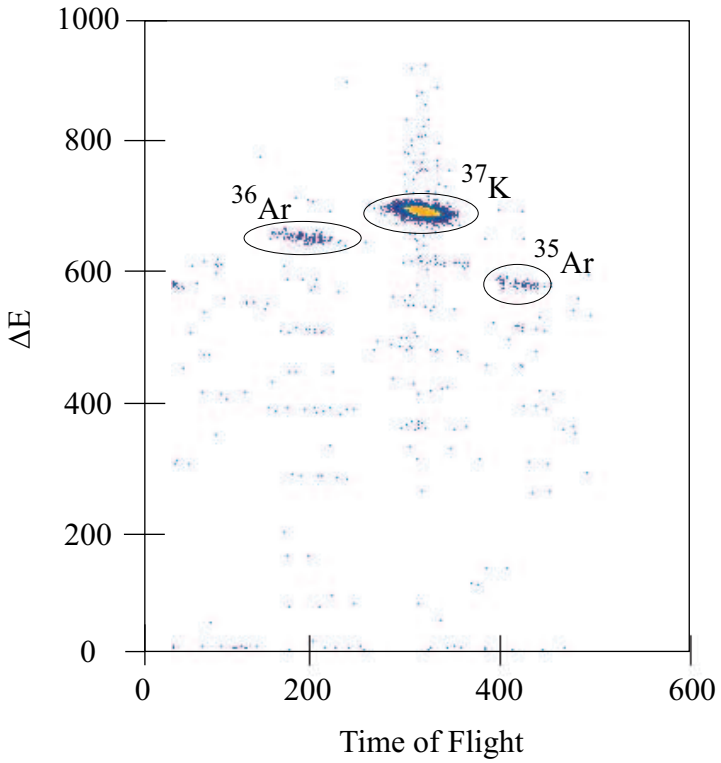

Figure 4.8: Delta E-TOF plot for ^{37}K produced at a beam angle of 0° and at 0% momentum.

in production for ^{37}K. A specific central value is required due to the large shift in fragment momentum away from the projectile momentum in the pickup process. The full momentum acceptance of the A1900 was set to ±0.5% using slits at image 2. Changing momentum values requires changing the Bρ vales for the A1900, which could conceivably change the composition of the secondary beam. Table 4.1 lists the beam components with percentages as identified at the A1900 focal plane for each momentum setting. In every case the ^{35}Ar contamination is below 10%.

Table 4.1: Beam contaminants at the various momentum settings for ^{37}K.

	Beam Components (%)		
Momentum (%)	^{37}K	^{36}Ar	^{35}Ar
-0.5	99.0	0.5	0.5
0.0	98.0	1.6	0.4
0.5	94.0	5.0	1.0
1.0	73.0	19.0	8.0

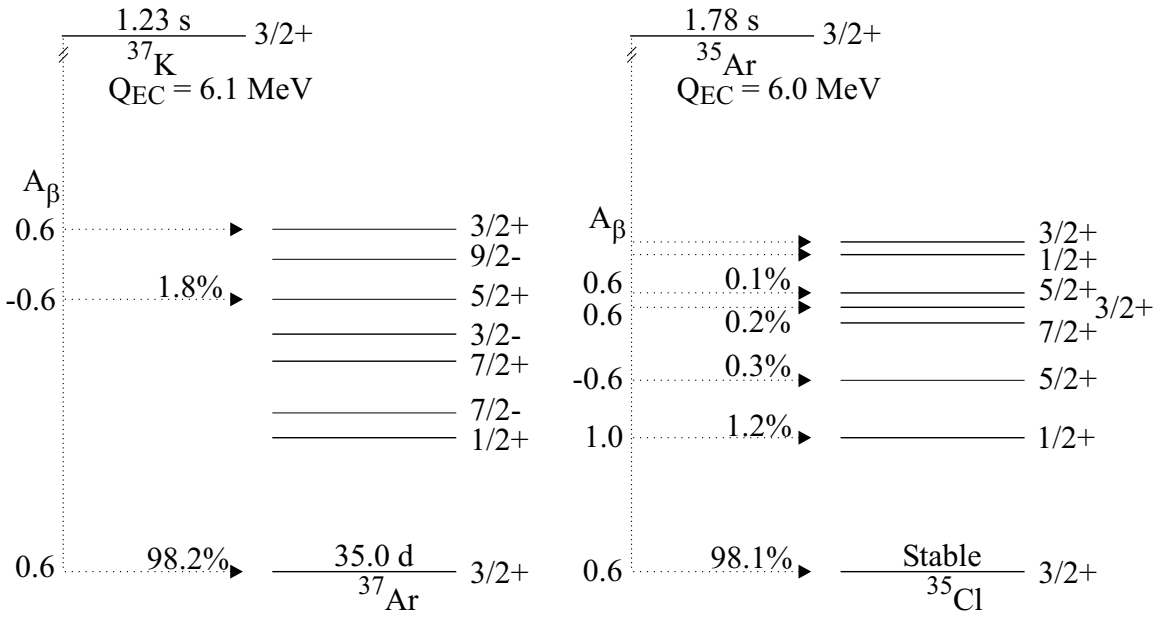

Figure 4.9: Decay schemes for ^{37}K and ^{35}Ar [39]. Asymmetry parameters (A_β) from [41] assuming pure GT transitions are listed in the figure.

The momentum distribution for the ^{37}K fragments, measured by reconstructing the position of the fragments at the image 2 position in the A1900, is shown Figure 4.10. The individual momentum values for each of the A1900 Bρ settings and for the primary beam are listed in Table 4.2. The ratio of the measured centroid of the momentum distribution of ^{37}K fragments relative to the beam momentum for the ^{37}K fragments is 0.975, in good agreement with the ratio Souliotis *et al.* [23] obtained from their measurement of neutron pickup products. An exponential fit excluding the lower 50% of the data on the low momentum side produces a $\sigma_{\|}$ of approximately 90 MeV/c, which is slightly greater than the value obtained in [23]. Given the mass dependence of $\sigma_{\|}$ as defined in [23], this is to be expected with the larger mass projectile used in this case.

The beta spectra for the thick and thin detectors for magnetic field on (solid black line) and for field off (dashed blue line) are shown in Figure 4.11. The beta spectra show the expected shape, but a magnetic field dependent asymmetry is evident in B4, where the field-on spectrum has more counts at higher energy than the field-off

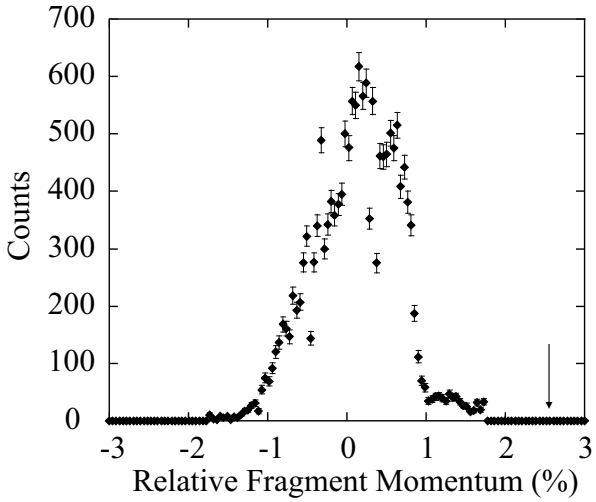

Figure 4.10: Experimental momentum distribution for ^{37}K fragments. 0% corresponds to the peak of the production yield. The beam momentum is indicated by the arrow.

spectrum. The beta spectrum for B4 in coincidence with B3 is shown in Figure 4.12. The asymmetry observed for B4 is not due to the behavior of fast electrons, which will trigger both B3 and B4, because the field on/off asymmetry is not evident when the thin detector is included in coincidence. More than 98% of the beta decays of ^{37}K go to the ground state of ^{37}Ar, which in turn decays to the ground state of β-stable ^{37}Cl 100% of the time (see Figure 4.9). The half-life of ^{37}Ar is 34 days, so background activity from the daughter decay should not affect the measurement. There are no gamma rays produced in the beta decay of these nuclei, so the asymmetry observed in B4 cannot be from decay gamma rays.

The source of the asymmetry in B4 remains somewhat of a mystery. However,

Table 4.2: Fragment momentum values for each fragment momentum point and for the incident beam.

Momentum (%)	Bρ1 (Tm)	Momentum (MeV/c)	Momentum (A·MeV/c)
-0.5	3.14208	17897	483.7
0.0	3.15787	17987	486.1
0.5	3.17366	18077	488.6
1.0	3.18945	18169	491.0
beam	3.32800	17959	498.9

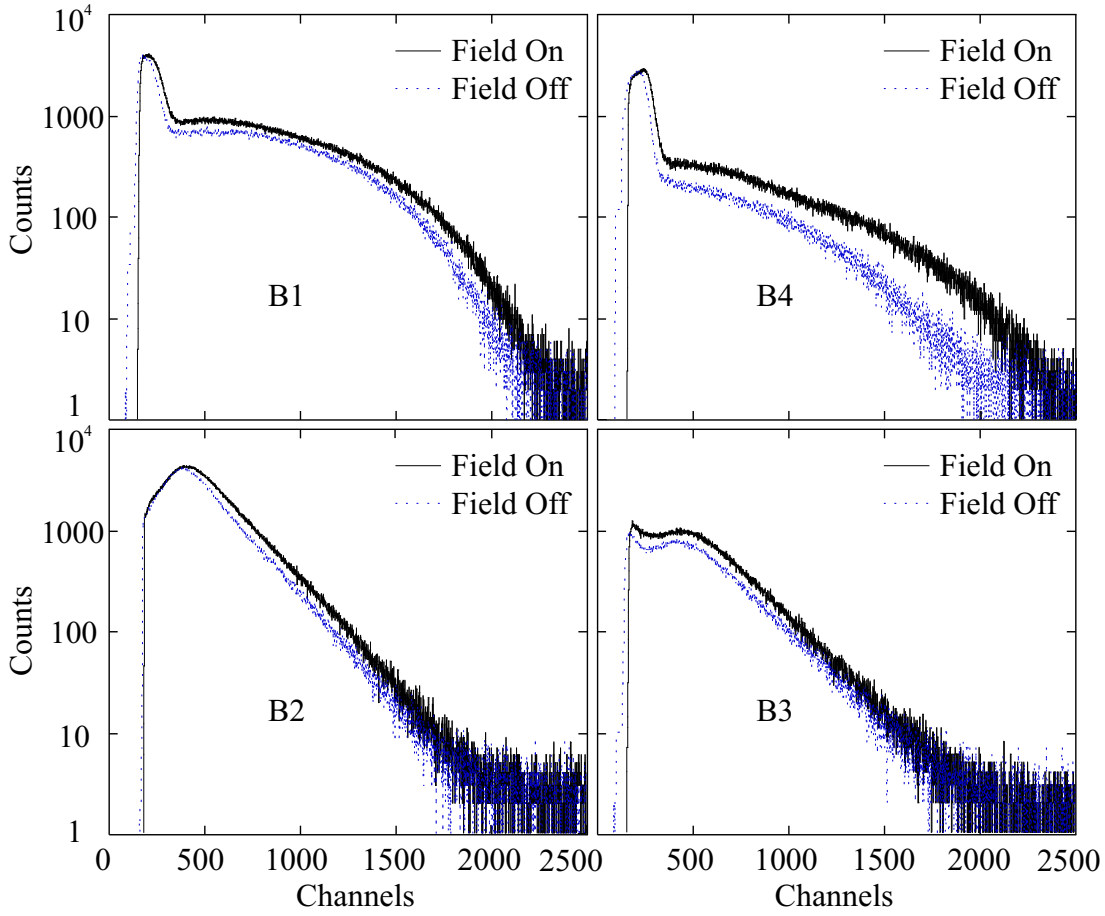

Figure 4.11: ^{37}K beta decay spectra for all 4 detectors (B1 top left, B4 top right, B2 bottom left, B3 bottom right). The field on spectra are solid black lines and the field off spectra are dashed blue lines. Data collected at a 0° beam angle.

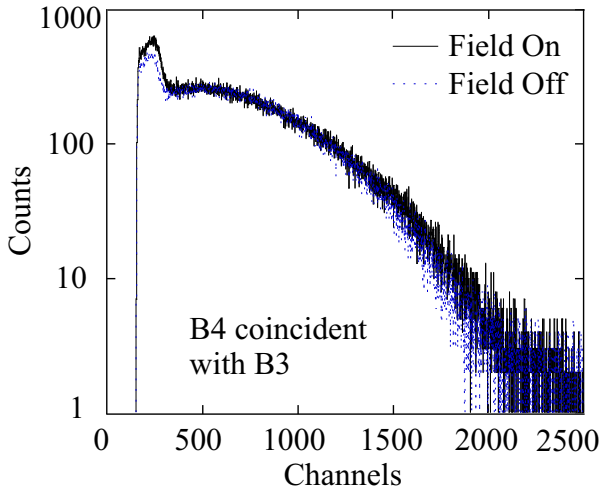

Figure 4.12: ^{37}K beta decay spectra for B4 coincident with B3. The field on spectrum is the solid black line and the field off spectrum is the dashed blue line. ($\theta_L = 0°$.)

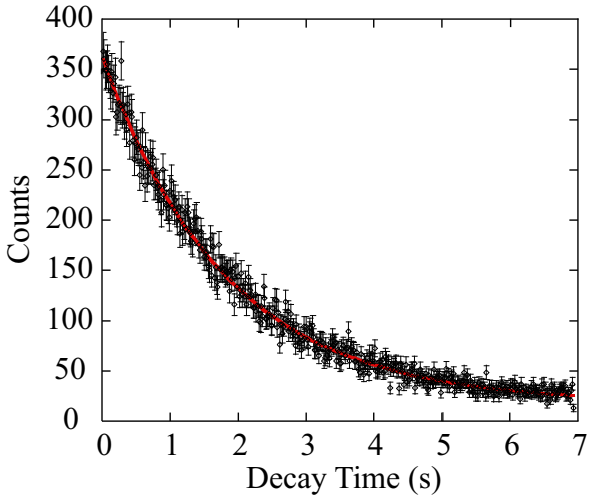

Figure 4.13: ^{37}K decay curve for B1 with red exponential fit.

since the coincidence data does not show such a pronounced effect, the asymmetry can be removed by simply using the coincident ratios. Furthermore, the data taken at $+2^{\circ}$ for a given momentum point have an accompanying 0° measurement as a normalization. Therefore, this asymmetry will be eliminated upon calculation of the double ratio, R.

4.2.2 Decay Curve

As in the ^{32}Cl case, prior to the polarization measurement, a half-life was measured to confirm the identity of the implanted fragments. The decay curve obtained for ^{37}K and the accompanying exponential fit are shown in Figure 4.13. The deduced half-life of 1.25(2) s agrees with the literature value of 1.226(7) s [43].

4.2.3 Polarization

For the polarization of ^{37}K, the coincident ratios were used for the reasons discussed above. As a check of the data, Figure 4.14 shows the asymmetry ratios for each individual run. Any sudden deviations or unexpected changes in the values for a set of conditions (beam angle and momentum) could signify anomalous behavior that

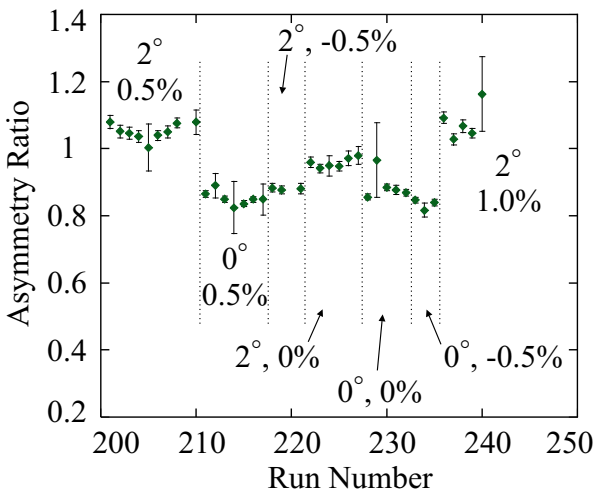

Figure 4.14: ^{37}K asymmetry ratios as a function of run number. Labels in figure correspond to beam angle (in degrees) and fragment momentum (as a percentage shift from central momentum).

deserves scrutiny. Clearly, the data are stable from run to run.

The asymmetry ratios for the four momentum points as a function of threshold energy for B1 and B4 are shown in Figure 4.15. A higher energy threshold has a better chance of removing any impurities that may be present. The polarization deduced using Equation 3.5 with an asymmetry parameter A_β=0.485±0.032 (as calculated in Appendix C) is shown in Figure 4.16. The asymmetry ratios used in this calculation were taken from the highest energy threshold shown in Figure 4.15. The polarization is plotted as a function of the relative fragment momentum, where p_0 is the momentum at the peak of the yield curve and p is the fragment momentum.

An alternative method of data analysis involved creating a plot of the thin detector versus the thick detector for both the up and down detectors. The thin detector should have a uniform response independent of beta energy, i.e. all betas will deposit the same amount of energy as they pass through the detector. The thick detector will have an energy dependent response since many of the betas will come to rest in this detector. The detector thickness of 2.0 cm is sufficient to stop 4 MeV β-particles. The average β-energy is expected to be about 1/3 of the Q-value, around 2 MeV for ^{37}K. Shown

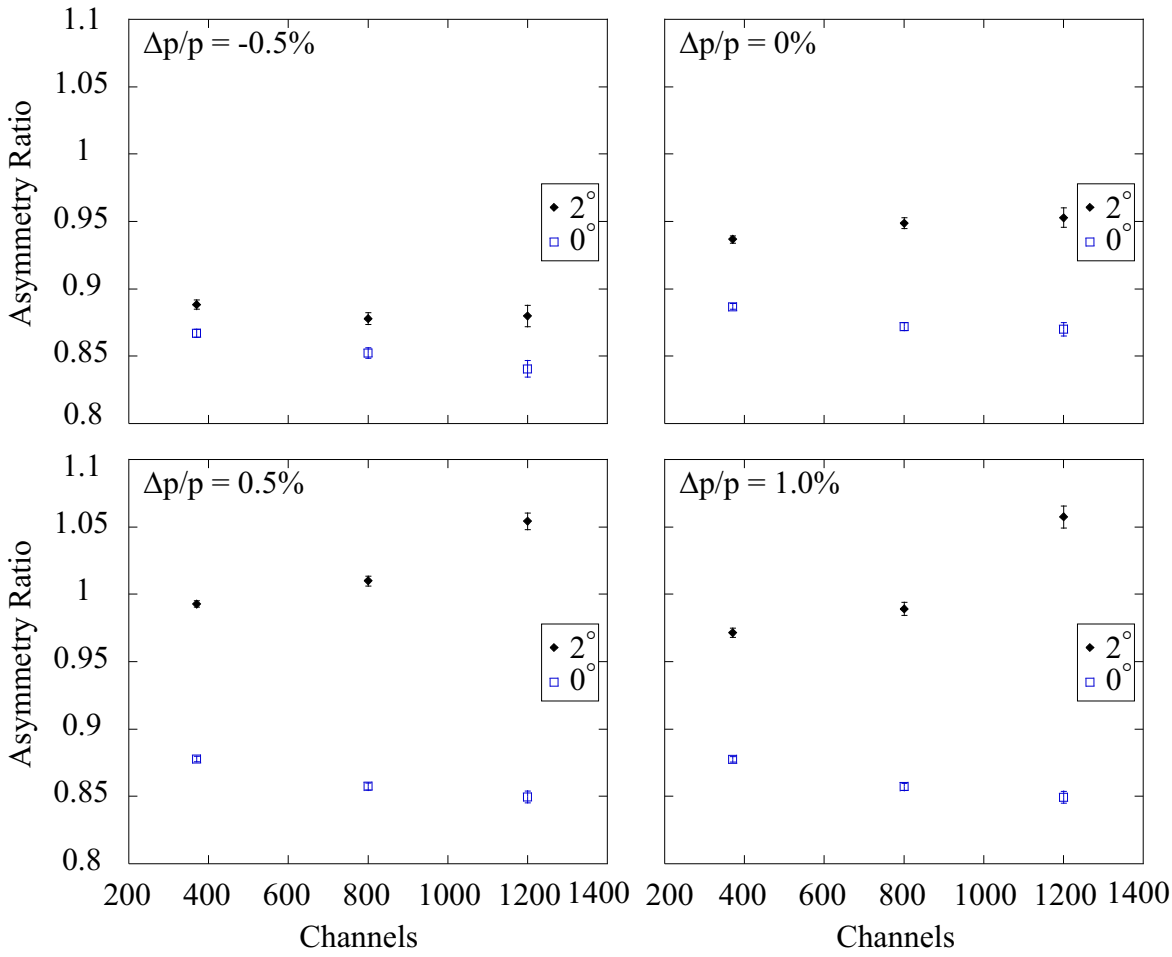

Figure 4.15: ^{37}K asymmetry ratios as a function of thick detector energy threshold.

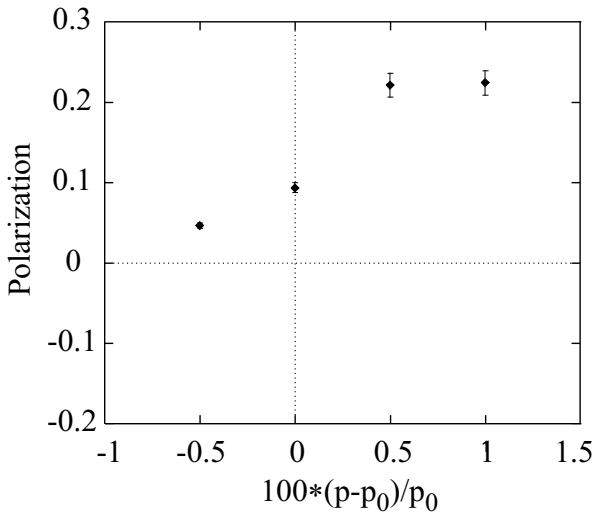

Figure 4.16: ^{37}K polarization (from the threshold method) as a function of relative fragment momentum (momentum error = $\pm$0.5%).

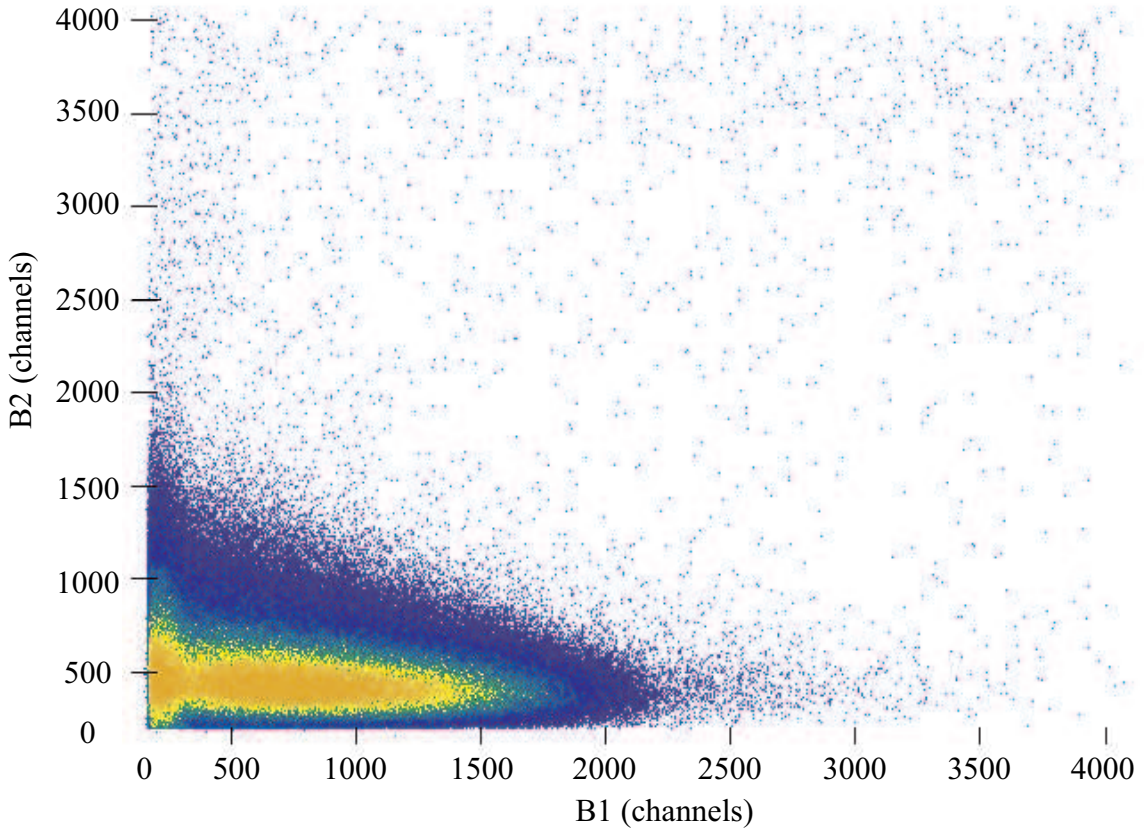

Figure 4.17: ^{37}K decay spectrum where B2 is plotted on the y-axis and B1 is plotted on the x-axis.

in Figure 4.17 is B2 plotted against B1 for the field on condition. The bright yellow areas show the uniform response on the y- (or B2-)axis and the energy dependent response on the x- (or B1-)axis. Setting thresholds that only accept events that fall within this area is a method to remove spurious events, and optimize the apparatus response by selecting only 'ideal' events.

Shown in Figure 4.18 is the polarization deduced using this 2-D technique, and the data are also tabulated in Table 4.3. These points have the same behavior as a function of momentum as do the values calculated using the traditional threshold method, except the deduced magnitude of the polarization extracted from the 2-D analysis is slightly lower. This is expected since the threshold on B1 and B4 is low, around 300 channels, and the lower energy threshold data have slightly lower

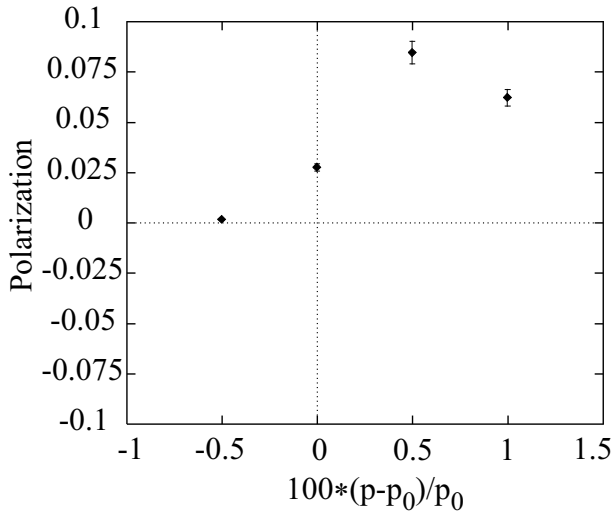

Figure 4.18: ^{37}K polarization as a function of relative fragment momentum calculated using the 2-D method of data analysis with an asymmetry parameter of 0.485. p_0 is the fragment momentum at the peak of the yield curve and p is the outgoing fragment momentum (momentum width = $\pm$0.5%).

Table 4.3: ^{37}K polarization values for each momentum setting as deduced using the 2-D method.

Momentum (%)	Polarization (%)
-0.5	0.19(01)
0.0	2.78(20)
0.5	8.48(56)
1.0	6.26(41)

asymmetry ratios, as evident in Figure 4.15. Since there are no features in the beta spectra that justify using the threshold of 1200 channels in the threshold analysis, the adopted polarization values will be taken from the 2-D analysis method.

4.3 Interpretation

The intent of the ^{32}Cl measurement was to test the A1900 and the β-NMR apparatus, and judging from Figure 4.7, that test was successful. Since the measured asymmetry ratios agree with the previous values [37], the aperture plate successfully limited the larger angular acceptance of the A1900. The interpretation, then, is that any attempt

to measure the polarization for ^{37}K will be possible. Either polarization that is present will be detected and characterized, or no polarization will be produced and therefore none will be measured.

The measured momentum distribution for ^{37}K is in good agreement with the pickup reaction studied by Souliotis *et al.*. Furthermore, the observation of polarization for ^{37}K produced by proton pickup from the target changing with fragment momentum is significant. Not only was polarization produced in a proton pickup reaction observed for the first time, but it was also produced with sizeable magnitude - up to 8% near the peak of the momentum distribution (see Figure 4.18). Such a large polarization was achieved even with the large angular acceptance ($\pm 2.5^{\circ}$) of the A1900. The original motivation for the measurement was the observation that large momentum transfers between the fragment and the removed nucleons in fragmentation reactions results in large polarization produced in those reactions. Since nucleon pickup reactions have large momentum transfers, they are expected to show large polarization if the classical momentum conservation used to model fragmentation can also be applied to pickup reactions.

The work of Souliotis *et al.* [23] to describe the centroids of momentum distributions for pickup products lead to the conclusion that the picked up nucleons have an average momentum equal to the Fermi momentum oriented parallel to the beam direction. By conservation, the momentum of the fragment will be given by

$$\langle p_f \rangle = \langle p_{pf} \rangle + \langle p_t \rangle \tag{4.1}$$

where $\langle p_f \rangle$ is the average fragment momentum, $\langle p_{pf} \rangle$ is the average momentum of the projectile part of the fragment and $\langle p_t \rangle$ is the average momentum of the picked up nucleon. As is shown in Table 4.2, the total momentum of the fragment is larger than the momentum of the incident projectile. Therefore, $\langle p_t \rangle$ will be positive and $\langle p_{pf} \rangle$

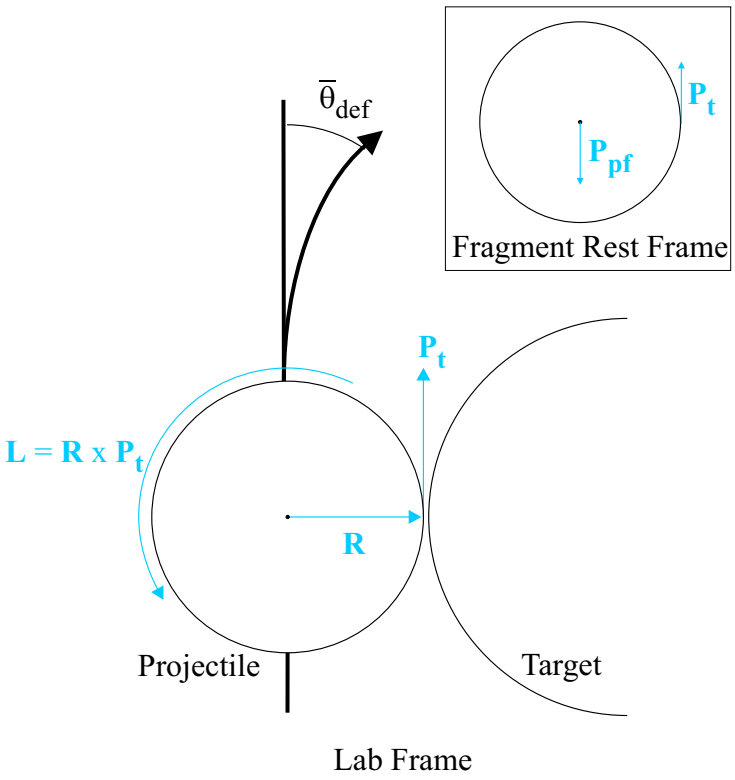

Figure 4.19: Schematic representation of the polarization produced in a pickup reaction. **R** is the position of the picked up nucleon, $\mathbf{P}_t$ is the linear momentum of the picked up nucleon, $\mathbf{P}_{pf}$ is the momentum of the projectile part of the fragment and **L** is the angular momentum of the fragment. The inset represents the fragment rest frame.

will be negative in the fragment rest frame, as shown in the inset of Figure 4.19. Thus, in the lab frame, the picked up nucleon will induce a positive fragment polarization through the cross product of its momentum, $\mathbf{P}_t$, and position, **R**, as depicted in Figure 4.19. Furthermore, as the momentum of the fragment increases, $\mathbf{P}_t$ will increase (because $\langle p_{pf} \rangle$ remains fixed) and result in larger polarization. This is indeed the case: Figure 4.18 depicts positive polarization that increases with increasing fragment polarization. This verifies the original assumption of Souliotis *et al.* that the Fermi momentum of the picked-up particle must lie parallel to the beam axis [23]. A far-side reaction is depicted in Figure 4.19 because the ^{9}Be(^{36}Ar,^{37}K)p reaction is dominated by the strong nuclear interaction. The sign of the polarization is predicted to be reversed for near-side reactions.

It is significant that the polarization is positive at the peak of the momentum distribution for the pickup case studied above. Fragmentation reactions, in general, produce negative polarization at the peak of the momentum yield curve. Yet, as a model based on the conservation of linear momentum, the KMA can describe the behavior of the polarization as a function of fragment momentum in both nucleon pickup and fragmentation reactions.

Chapter 5

Conclusions & Outlook

A statistical Monte Carlo code (the ELPC) has been developed and shown to quantitatively predict the polarization produced in intermediate-energy heavy-ion fragmentation reactions. The ELPC is based on a purely classical momentum conservation model (the KMA). The ELPC can be used as an optimization tool to predict polarization under different reaction conditions. Changing the beam angle, beam angle acceptance, fragment momentum etc. effects the polarization in different ways and understanding these processes is vital to producing maximally polarized secondary fragments.

However, there are several limitations in the applicability of the ELPC. Since nuclear structure is not included in any capacity, even-even nuclei with spin zero ground states are not properly treated by the ELPC. Nuclei with $s_{1/2}$ ground states are also treated incorrectly. Since these nuclei have zero angular momentum in their ground state, the statistical model should not be able to produce polarization through the angular momentum conservation of the KMA. Along similar lines, neglecting intrinsic nucleon spin and treating protons and neutrons identically can also influence the polarization calculations using the ELPC. Including such nuclear structure information would provide for the proper treatment of polarization production in the ELPC.

A further limitation lies in the range of applicability of the ELPC. Since most of the comparison with data involves light fragments, the applicability of the ELPC to heavier fragments remains to be fully explored. Although the code does not have assumptions that specifically limit it to the lighter mass fragments, the predictive power of the code has not been tested in a higher mass regime.

Within the ELPC, the process of nucleon evaporation has been shown to decrease the calculated polarization magnitude and change the behavior of the polarization as a function of fragment momentum for the test reaction of ^{93}Nb(^{18}O,^{12}B)X. However, this is only one test case. More examples would help validate the importance of evaporation. Yet, even with just the one test case, the process of nucleon evaporation as it is implemented in the ELPC does not fully account for the discrepancy between calculated and experimental polarization magnitudes. Currently, the evaporation step is approximate, treated in an average way and ignores the type of particle that is evaporated from the fragment. Indeed, the whole process of evaporation in the ELPC only reduces the angular momentum of the fragment by a fraction of an $\hbar$. This fragment angular momentum value is probably too low, and changes should be made to increase it nearer to $1\hbar$. These changes would most likely deal with how the evaporated particle leaves the fragment and the conservation of linear and angular momentum for the evaporation event. Furthermore, given that the binding energy of lighter mass fragments is low (in the 5 MeV range), the 20 MeV evaporation threshold in the ELPC is too large. After the evaporation step, a ^{12}B fragment, which has a neutron separation energy of 3.4 MeV, could have an excitation energy up to 20 MeV. Clearly, evaporation as implemented in the ELPC needs improvement. Perhaps a statistical evaporation code like CASCADE [21] which correctly models evaporation in fusion evaporation reactions could be modified and used as the basis for the evaporation step in the ELPC. A more detailed incorporation of evaporation into the ELPC could improve the ELPC's ability to predict polarization produced in reactions

where many nucleons are removed.

Changing the way evaporation is handled in the ELPC will also have consequences for the γ-ray de-orientation process. The implementation of γ-ray de-orientation will not change, only the input parameters for the cascade will change with changes in evaporation. Specifically, a reduction in the evaporation threshold will reduce the amount of excitation energy left over after the evaporation step, and changing the way the evaporation process affects the polarization will potentially change the final spin of the fragment. Since γ-ray de-orientation depends on both the amount of excitation energy and the spin of the fragment, altering these things will change the de-orientation. Lower excitation energy and fragment spin will result in fewer emitted γ-rays. Fewer emitted γ-rays will, in general for a given spin, lead to less de-orientation. The current state of the ELPC probably makes up for the underestimation of the effects of evaporation with an overestimation of the γ-ray de-orientation. The high excitation energy left in the fragment after evaporation leads to a longer γ-ray relaxation cascade which increases the resulting de-orientation. Thus, improving the incorporation of evaporation into the ELPC could also have a positive influence on γ-ray de-orientation in the ELPC.

The ELPC could also be modified to have a more realistic deflection angle distribution. This would give the proper *quantitative* behavior of the number of counts with increasing beam angle and also slightly modify the polarization behavior by affecting which fragments get accepted into the detector window.

Errors in the polarization calculations using the ELPC will manifest inherently in the simple assumptions used for the polarization calculations (i.e. in using a statistical model). Treating the removed nucleons as a group, although effective in a gross or average way, could no doubt be improved upon by treating each nucleon individually. But this would require a different model and a different set of assumptions, which themselves will have error. Perhaps this is a viable alternative to using the

KMA for predicting spin polarization resulting from intermediate-energy heavy-ion fragmentation reactions.

The ELPC was originally designed to calculate polarization produced in fragmentation reactions. The ability to calculate m-state distributions and thus alignment would be useful and relatively straightforward to add to the code. Since the angular momentum components for all three axes are already calculated, the m-state population can be calculated relative to the y-axis (beam axis) using the relation

$$\cos\theta = \frac{\mathrm{l_y}}{\mathrm{L}} \tag{5.1}$$

where $\mathrm{l_y}$ is the y component of angular momentum and L is the total angular momentum. The m-state distribution can be estimated using

$$\cos\theta = \frac{\mathrm{m}}{\sqrt{\mathrm{I(I+1)}}} \tag{5.2}$$

where m is the magnetic quantum number and I is the spin of the fragment. From the m-state distribution the alignment can be calculated. The integration of this alignment supplement into the existing code is underway and will be reported elsewhere.

The ELPC also has the potential to calculate isomer production yields. Isomers produced in fragmentation reactions have been studied by Daugas *et al.* [44], and the TPC was applied to understand their results. The ELPC, which has quantitative predictive power, could readily be applied to understand isomer fractions produced in heavy-ion fragmentation reactions.

In the experimental portion of this work, we have for the first time measured the polarization produced via the proton pickup production mechanism. We have extended the classical conservation model used to characterize polarization produced in fragmentation reactions to explain the observed polarization for pickup reactions. This work supports the conclusions drawn by Souliotis *et al.* that nucleon pickup

reactions can be understood on the basis of momentum conservation. Specifically, that the nucleon(s) that get picked up carry an average momentum equal to the Fermi momentum oriented along the beam direction.

The observation of polarization produced in pickup reactions has shed light on the pickup reaction mechanism. Further measurements using different targets could increase this understanding by examining the effects of near- and far-side reactions. It could also give more insight into the momentum conservation model developed by Souliotis *et al.*. Furthermore, measurements of the polarization of different mass fragments could increase the understanding of depolarization processes. For example, ^{35}K produced from ^{36}Ar requires 1 proton pickup and 2 neutron evaporation. Studying the polarization of ^{35}K would provide a direct measure of the effects of evaporation on spin polarization. This new method provides an avenue to produce polarized nuclei of very neutron-deficient nuclei that other production techniques (e.g. fragmentation) can not efficiently reach.

Appendix A

Mean Deflection Angle Calculation

The mean deflection angle is the average scattering angle through which a projectile is deflected as a result of an interaction with a stationary target. For a single interaction, the deflection angle θ (see Figure A.1) is given by

$$\theta = \pi - 2\phi \tag{A.1}$$

with

$$\phi = \int_{r_{\min}}^{\infty} \frac{b\,dr}{r^2\sqrt{1 - \frac{b^2}{r^2} - \frac{U(r)}{E}}} \tag{A.2}$$

where b is the impact parameter, r is the distance between the centers of the two objects, U(r) is the potential governing the interaction of the two objects, $r_{\min}$ is the separation between the centers of the two point-like objects at the distance of closest approach and the energy, E, is given by

$$E = \frac{1}{2}mv_{\infty}^2 \tag{A.3}$$

where v_{∞} is the velocity of the projectile at $r = \infty$ [45]. The projectile is assumed to move away from the target after the scattering event with momentum equal to the incident momentum, thus $E(v_{\infty}) = E(v_{\text{incident}})$. This formula is general for any

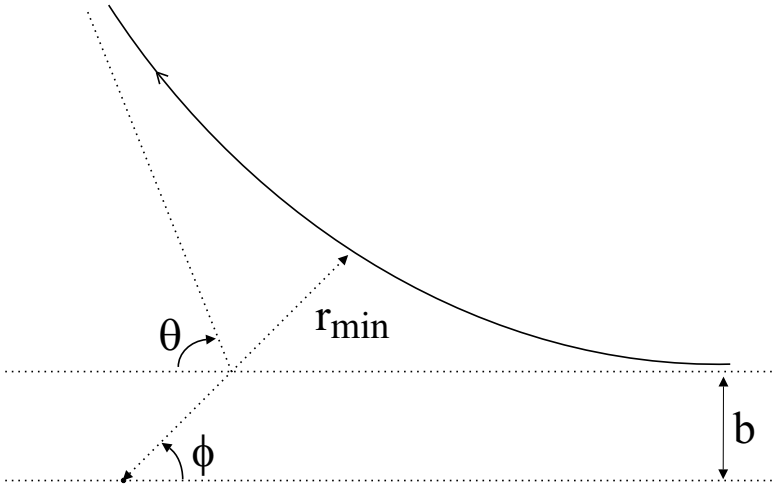

Figure A.1: Variable definitions for mean deflection angle calculation.

spherically symmetric potential.

The potential U(r) is defined by

$$U(r) = U_{\text{Coulomb}}(r) + U_{\text{nuclear}}(r). \tag{A.4}$$

The Coulomb part of the potential is repulsive and is equal to

$$U_{\text{Coulomb}}(r) = \frac{1.438\, q\, Q}{r} \tag{A.5}$$

where q and Q are the charges on the projectile and target respectively, and r is the separation in fm. The nuclear part of the potential is based on the real part of the optical model [46], and is attractive:

$$U_{\text{nuclear}}(r) = \frac{-V_0}{1 + e^{(\text{r}-\text{R})/\text{a}}}. \tag{A.6}$$

Here V_0 is the depth of the optical model potential, $R = 1.2\ (\sqrt[3]{A_1} + \sqrt[3]{A_2})$ where A_1 and A_2 are the masses of the projectile and target respectively, and a is a measure of the diffuseness of the nuclear surface. V_0 and a are parameters fit to experimental data with values usually in the range $a \approx 0.5$ and $V_0 \approx 50$ MeV. There are very limited

nucleus-nucleus scattering data, and an exact determination or parameterization of V_0 is difficult for any given projectile-target combination. Typically this is not a problem because in head-on collisions, the nuclear potential does not have a large influence. However, the treatment of peripheral collisions depends on the optical potential. In the minimum, a determination of V_0 for each reaction is needed. A parameterization of V_0 based on energy and/or number of nucleons removed would suffice. Such a parameterization does not presently exist; therefore a value of 50 MeV has been used for V_0 in all calculations except where prior knowledge of a mean deflection angle is present.

The angle ϕ is calculated via numerical integration using Equation A.2 with an upper limit for r of 1x10^9 and a step size of 0.00001. The input parameters are the charge and mass of the projectile and target, the energy of the projectile and the distance of closest approach, r_{min}. The mean deflection angle is then calculated from ϕ using Equation A.1.

This distance of closest approach (one of the aforementioned input parameters) is calculated using one of two equations from Gosset *et al.* [14]:

$$\frac{N_1}{A_1} = \frac{3}{4}(1-\nu)^{1/2}\left(\frac{1-\beta}{\nu}\right)^2 - \frac{1}{8}[3(1-\nu)^{1/2}-1]\left(\frac{1-\beta}{\nu}\right)^3 \tag{A.7}$$

or

$$\frac{N_1}{A_1} = \frac{3}{4}(1-\nu)^{1/2}\left(\frac{1-\beta}{\nu}\right)^2 - \frac{1}{8}(\xi)\left(\frac{1-\beta}{\nu}\right)^3 \tag{A.8}$$

where

$$\xi = \frac{3(1-\nu)^{1/2}}{\mu} - \frac{[1-(1-\mu^2)^{3/2}][1-(1-\mu)^2]^{1/2}}{\mu^3}. \tag{A.9}$$

Equation A.7 corresponds to a target with radius R_2 and mass A_2 gouging a cylindrical channel with radius greater than R_1 into a projectile with radius R_1 and mass A_1 (see Figure A.2). Equation A.8 corresponds to a target with radius R_2 and mass A_2 gouging a cylindrical channel with radius smaller than R_1 into a projectile with radius R_1 and

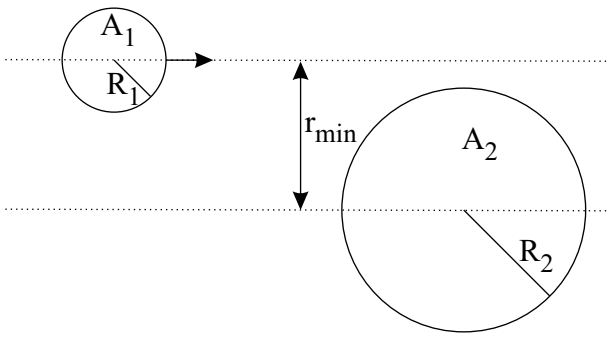

Figure A.2: Variable definitions for Equations A.7 and A.8.

mass A_1. In the equations, N_1 is the number of nucleons removed from the projectile, A_1 is the mass of the projectile, and ν, β and μ are normalized parameters given by

$$\nu = \frac{R_1}{R_1 + R_2} \tag{A.10}$$

$$\beta = \frac{r_{min}}{R_1 + R_2} \tag{A.11}$$

and

$$\mu = \frac{R_2}{R_1} \tag{A.12}$$

where R_1 is the radius of the projectile, R_2 is the radius of the target and r_{min} is the point of closest approach as shown in Figure A.2. To determine r_{min}, the appropriate equation (either A.7 or A.8) is solved for β using a known number of removed nucleons N_1. Equation A.11 is then solved for r_{min}.

The impact parameter used in Equation A.2 is determined from knowledge of r_{min}. According to [45], r_{min} could be determined from a zero of the radicand of Equation A.2,

$$0 = 1 - \frac{b^2}{r_{min}^2} - \frac{U(r_{min})}{E}, \tag{A.13}$$

but this requires the impact parameter, b, which is not known. Since Gosset's equations allow the determination of r_{min}, Equation A.13 can instead be used to calculate b using the known values of r_{min}, $U(r_{min})$ and E.

Appendix B

Tangential Vector Calculation

A point randomly selected on the surface of a sphere with angular momentum oriented along an arbitrary axis in space will have a momentum tangent to the surface. The components of this tangent vector in a fixed axis frame can be calculated using the vectors defined in Figure B.1. The vector **L** is the angular momentum of the fragment after abrasion; its components L_x, L_y and L_z are known. The vector **R** is the random position of the nucleon to be evaporated; its components R_x, R_y and R_z are known through knowledge of the random angles θ and ϕ and the radius of the fragment R. The radius of the circular trajectory of the nucleon before evaporation is determined by the angle γ. P_x, P_y and P_z are the components of the tangent vector **T** and are to be calculated.

The angle γ can be calculated with knowledge of the directional cosines of the vectors **R** and **L** and is given by

$$\gamma = \cos^{-1}\left(\frac{L_x R_x + L_y R_y + L_z R_z}{LR}\right) \tag{B.1}$$

where L and R are the magnitudes of **L** and **R** respectively. Using γ, the magnitude of **T** can be calculated recalling that $L = I\omega$ and I is the moment of inertia. Assuming a spherical shape, $I = 5/2mR^2$ where m is the mass of the fragment and R is the

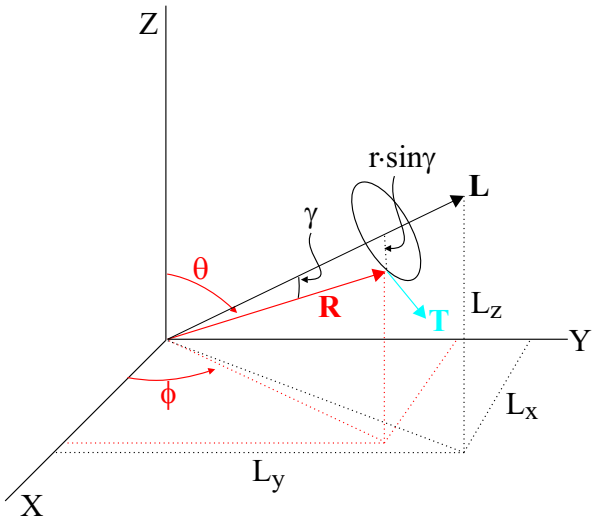

Figure B.1: Schematic representation of tangent vector **T** at position **R** relative to an angular momentum **L**.

radius:

$$T = R\omega \sin\gamma. \tag{B.2}$$

If the magnitude of **T** is known, then

$$P_x^2 + P_y^2 + P_z^2 = (mR\omega \sin\gamma)^2 \tag{B.3}$$

where m is the mass of the nucleon to be evaporated in units of nucleons.

Since **T** is the tangent vector to the sphere, it will be perpendicular to **L**. Furthermore, it is apparent from Figure B.1 that **R** will also be perpendicular to **T**. Thus, the scaler product of **T** with both **R** and **L** will be zero,

$$P_xR_x + P_yR_y + P_zR_z = 0 \tag{B.4}$$

$$P_xL_x + P_yL_y + P_zL_z = 0 \tag{B.5}$$

where the P_i, R_i and L_i, i = x, y, or z are the components of **P**, **R** and **L** respectively.

Solving for P_x in Equation B.5 gives

$$P_x = \frac{-P_y L_y - P_z L_z}{L_x}. \tag{B.6}$$

Substituting Equation B.6 into B.4 yields

$$P_y = \frac{R_x P_z L_z - R_z P_z L_x}{R_y L_x - R_x L_y}. \tag{B.7}$$

Using B.6 and B.7 in B.3 and solving for P_z gives

$$P_z^2 = \frac{R^2 \omega^2 \sin^2 \gamma}{\left(\frac{R_z L_x L_y - R_x L_y L_z}{R_y L_x^2 - R_x L_x L_y} - \frac{L_z}{L_x}\right)^2 + \left(\frac{R_x L_z - R_z L_x}{R_y L_x - R_x L_y}\right)^2 + 1}. \tag{B.8}$$

All of the quantities in Equation B.8 are known. Once P_z is calculated, it can be substituted in to Equation B.7; P_z and P_y can then be used in Equation B.6 to calculate P_x.

Appendix C

^{37}K Asymmetry Parameter Calculation

Calculating the polarization from asymmetry ratios requires knowledge of the asymmetry parameter, A_1. The asymmetry parameter for $\beta^{\pm}$-decay is calculated using

$$A_1(\beta^{\pm}) = \frac{2}{3}\frac{p}{E}\frac{\mp F_1(11I_fI_i) + yF_1(01I_fI_i)}{1+y^2} \tag{C.1}$$

where p is the electron momentum, E is the total relativistic energy, $F_1(LL'I_fI_i)$ is the generalized F-coefficient for a transition between states I_f and I_i with mixed multipolarities L and L′ and

$$y = \frac{C_V < F >}{C_A < GT >} \tag{C.2}$$

where $C_A(C_V)$ is the axial(vector) coupling constant, and <F>(<GT>) represents the Fermi(Gamow-Teller) matrix element. Equation C.1 and tabulated F-coefficients can be found in [32].

Ordinarily, the Fermi matrix element is small and the Fermi contribution to the asymmetry parameter can be ignored. However, since ^{37}K decays into its mirror partner ^{37}Ar (with 99.85% branching to the ground state [47]), the Fermi contribution is

significant and must be included. Ironically, the mirror decay which requires knowledge of the Gamow-Teller and Fermi contributions also makes calculating the matrix elements and coupling constants straightforward, only requiring the $ft_{1/2}$ value [48]:

$$ft_{1/2} = (6139 \pm 7)\,[< F > + < GT > \left(\frac{C_A}{C_V}\right)^2]^{-1} \tag{C.3}$$

where the constant 6139±7 comes from [49].

Because this case is mirror decay [48], the Gamow-Teller matrix element can be taken as

$$< GT >= \frac{j}{j+1} = 0.60 \tag{C.4}$$

for $j = l - 1/2$ using $j = 3/2$, the ground state of ^{37}K, and $l = 2$ for the $d_{3/2}$ proton that decays. The Fermi matrix element is 1.

Using log ft = 3.66(01) for ^{37}K [47] in Equation C.3,

$$\frac{C_A}{C_V} = 0.7564 \pm 0.0268 \tag{C.5}$$

which gives

$$y = \frac{C_V < F >}{C_A < GT >} = 2.2034 \pm 0.0781 \tag{C.6}$$

for an asymmetry parameter of

$$A_1(\beta) = 0.485 \pm 0.032 \tag{C.7}$$

for the decay of the ^{37}K into ^{37}Ar.

Bibliography

[1] K. Alder and A. Winther. *Electromagnetic Excitation.* North-Holland, Amsterdam, 1975.

[2] Y. Yamamoto and K.-I. Kubo. *Phys. Rev. C*, **49**:360, 1994.

[3] K. Sugimoto, N. Takahashi, A. Mizobuchi, Y. Nojiri, T. Minamisono, M. Ishihara, K. Tanaka, and H. Kamitsubo. *Phys. Rev. Lett.*, **39**:323, 1977.

[4] M. Ishihara, K. Tanaka, T. Kammuri, K. Matsuoka, and M Sano. *Phys. Lett. B*, **73**:281, 1978.

[5] D. M. Brink. *Phys. Lett. B*, **40**:37, 1972.

[6] T. Udagawa and T. Tamura. *Phys. Rev. Lett.*, **41**:1770, 1978.

[7] W. Trautmann, J. de Boer, W. Dünnweber, G. Graw, R. Kopp, C. Lauterbach, H. Puchta, and U. Lynen. *Phys. Rev. Lett.*, **39**:1062, 1977.

[8] F. Pougheon, P. Roussel, M. Bernas, F. Diaf, B. Fabbro, F. Naulin, E. Plagnol, and G. Rotbard. *Nucl. Phys. A*, **325**:481, 1979.

[9] P. D. Bond. *Phys. Rev. Lett.*, **40**:501, 1978.

[10] K. H. Tanaka, Y. Nojiri, T. Minamisono, K. Asahi, and N. Takahashi. *Phys. Rev. C*, **34**:580, 1986.

[11] K. Asahi, M. Ishihara, N. Inabe, T. Kubo, M. Adachi, H. Takanashi, M. Kougucki, M. Fukuda, D. Mikolas, D. J. Morrissey, D. Beaumel, T. Shimoda, H. Miyatake, and N. Takahashi. *Phys. Lett. B*, **251**:488, 1990.

[12] A. Ohnishi, T. Maruyama, and H. Horiuchi. *Prog. Theor. Phys.*, **87**:417, 1992.

[13] H. Okuno, K. Asahi, H. Sato, H. Ueno, J. Kura, M. Adachi, T. Nakamura, T. Kubo, N. Inabe, A. Yoshida, T. Ichihara, Y. Kobayashi, Y. Ohkubo, M. Iwamoto, F. Ambe, T. Shimoda, H. Miyatake, N. Takahashi, N. Nakamura, D. Beaumel, D. J. Morrissey, W.-D. Schmidt-Ott, and M. Ishihara. *Phys. Lett. B*, **335**:29, 1994.

[14] J. Gosset, H. H. Gutbrod, W. G. Meyer, A. M. Paskanzer, A. Sandoval, R. Stock, and G. D. Westfall. *Phys. Rev. C*, **16**:629, 1977.

[15] P. F. Mantica, R. W. Ibbotson, D. W. Anthony, M. Fauerbach, D. J. Morrissey, C. F. Powell, J. Rikovska, M. Steiner, N. J. Stone, and W. B. Walters. *Phys. Rev. C*, **55**:2501–2505, 1997.

[16] A. S. Goldhaber. *Phys. Lett. B*, **53**:306, 1974.

[17] D. E. Greiner, P. J. Lindsrom, H. H. Heckman, B. Cork, and F. S. Bieser. *Phys. Rev. Lett.*, **35**:152, 1975.

[18] J.-J. Gaimard and K.-H. Schmidt. *Nucl. Phys. A*, **531**:709, 1991.

[19] K.-H. Schmidt, T. Brohm, H.-G. Clerc, M. Dornik, M. Fauerbach, H. Geissel, A. Grewe, E. Hanelt, A. Junghans ans A. Magel, W. Morawek, G. Münzenberg, F. Nickel, M. Pfützner, C. Scheidenberger, K. Sümmerer, D. Vieira, B. Voss, and C. Zeigler. *Phys. Lett. B*, **300**:313, 1993.

[20] W. Freidman, M. B. Tsang, D. Bazin, and W. G. Lynch. *Phys. Rev. C*, **62**:064609, 2000.

[21] F. Púhlhofer. *Nucl. Phys. A*, **280**:267, 1977.

[22] A. Gavron. *Phys. Rev. C*, **21**:230, 1980.

[23] G. A. Souliotis, D. J. Morrissey, N. A. Orr, B. M. Sherrill, and J. A. Winger. *Phys. Rev. C*, **46**:1383, 1992.

[24] M. Belleguic, M.-J. Lòpez-Jiménez, M. Stanoiu, F. Azaiez, O. Sorlin M.-G. Saint-Laurent, N. L. Achouri, J.-C. Angélique, C. Bourgeois, C. Borcea, J.-M. Dougas, C. Donzaud, F. De Oliveira-Santos, J. Duprat, S. Grévy, D. Guillemaud-Mueller, S. Leenhardt, M. Lewitowicz, Yu.-E. Penionzhkevich, and Yu. Sobolev. *Nucl. Phys. A*, **682**:136c, 2001.

[25] R. Grzywacz, R. Anne, G. Auger, D. Bazin, C. Borcea, V. Borrel, J. M. Corre, T. Dörfler, A. Formichov, M. Gaelens, D. Guillemaud-Mueller, R. Hue, M. Huyse, Z. Janas, H. Keller, M. Lewitowicz, S. Lukyanov, A. C. Mueller, Yu. Penionzhkevich, M. Pfützner, F. Pougheon, K. Rykaczewski, M. G. Saint-Laurent, K. Schmidt, W.-D. Schmidt-Ott, O. Sorlin, J. Szerypo, O. Tarasov, J. Wauters, and J. Żylicz. *Phys. Lett. B*, **355**:439, 1995.

[26] W. D. Hamilton (Ed.). *The Electromagnetic Interaction in Nuclear Spectroscopy.* North-Holland, Amsterdam, 1975.

[27] G. A. Leander. *Comp. Phys. Comm.*, **47**:311–340, 1987.

[28] T. Von Egidy, H. H. Schmidt, and A. N. Behkami. *Nucl. Phys. A*, **481**:189–206, 1988.

[29] A. E. Stuchbery, D. E. Groh, and P. F. Mantica. in preparation.

[30] K. Matsuta, A. Ozawa, Y. Nojiri, T. Minamisono, M. Fukuda, A. Kitagawa, S. Momota, T. Ohtsubo, Y. Matsuo, H. Takechi, S. Fukuda, I. Minami, K. Sugimoto, I. Tanihata, K. Omata, J. R. Alonso, G. F. Krebs, and T. J. M. Symons. *Phys. Lett. B*, **281**:214, 1992.

[31] K. Matsuta, S. Fukuda, T. Izumikawa, M. Tanigaki, M. Fukuda, M. Nakazato, M. Mihara, T. Onishi, T. Yamaguchi, T. Miyake, M. Sasaki, A. Harada, T. Ohtsubo, Y. Nojiri, T. Minamisono, K. Yoshids, A. Ozawa, T. Kobayashi, I. Tanihata, J. R. Alonso, G. F. Krebs, and T. J. M. Symons. *AIP Conf. Proc.*, **339**:623, 1995.

[32] K. S. Krane. *Low Temperature Nuclear Orientation, Edited by N.J. Stone and H. Postma.* North-Holland, Amsterdam, 1986.

[33] D. W. Anthony, P. F. Mantica, D. J. Morrissey, and G. Georgiev. *Hyperfine Int*, **127**:485, 2000.

[34] K Tompa, L. Grenacs, J. Lehmann, and R. Pirlot. *Hyperfine Int*, **60**:877, 1990.

[35] D. J. Morrissey, B. M. Sherrill, M. Steiner, A. Stolz, and I. Wiedenhoever. *Nucl. Instr. and Meth. B*, in press, 2002.

[36] D. J. Morrissey and NSCL Staff. *Nucl. Instr. and Meth. B*, **126**:316, 1997.

[37] W. F. Rogers, G. Georgiev, G. Neyens, D. Borremans, N. Colier, R. Coussement, A. D. Davies, J. L. Mitchell, S. Teughels, B. A. Brown, and P. F. Mantica. *Phys. Rev. C*, **62**:44312, 2000.

[38] T. Minamisono, J. W. Hugg, D. G. Mavis, T. K. Saylor, S. M. Lazarus, H. F. Glavish, and S. S. Hanna. *Hyperfine Int*, **2**:315, 1976.

[39] R. B. Firestone. *Table of Isotopes.* John Wiley & Sons, New York., 8th edition, 1996.

[40] D. Bazin, O. Tarasov, M. Lewitowicz, and O. Sorlin. *Nucl. Instr. and Meth. A*, 482:307, 2002.

[41] K. Asahi, M. Ishihara, H. Kamitsubo, N. Takahashi, Y. Norjiri, T. Minamisono, A. Mizobuchi, and K. Sugimoto. *Nucl. Instr. and Meth.*, **220**:389, 1984.

[42] A. J. Armini, J. W. Sunier, and J. R. Richardson. *Phys. Rev. C*, **165**:1194, 1968.

[43] R. B. Firestone and P. M. Endt. *Nucl. Phys. A*, **633**:1, 1998.

[44] J. M. Daugas, R. Grzywacz, M. Lewitowicz, M. J. Lopez-Jimenez nad F. de Oliveira-Santos, J. C. Angélique, L. Axelsson, C. Borcea, C. Longour, and G. Neyens. *Phys. Rev. C*, **63**:064609, 2001.

[45] L. D. Landau and E. M. Lifshitz. *Mechanics, by L.D. Landau and E.M. Lifshitz. Translated from the Russian by J.B. Sykes and J.S. Bell.* Oxford, New York, Pergamon Press, 3d ed edition, 1976.

[46] K. S. Krane. *Introductory Nuclear Physics.* John Wiley & Sons, Inc., 1988.

[47] F. M. Mann, H. S. Wilson, and R. W. Kavanagh. *Nucl. Phys. A*, **258**:341, 1976.

[48] M. Morita. *Beta Decay and Muon Capture.* W. A. Benjamin, Inc., Reading, Mass, 1973.

[49] W.-T. Chou, E. K. Warburton, and B. A. Brown. *Phys. Rev. C*, **47**:163, 1993.